Inertial Measurement Unit based Virtual Antenna Arrays - DoA Estimation and Positioning in Wireless Networks

Yaqoob, Muhammad Atif

2016

Document Version:
Publisher's PDF, also known as Version of record

Link to publication

Citation for published version (APA):
Yaqoob, M. A. (2016). *Inertial Measurement Unit based Virtual Antenna Arrays - DoA Estimation and Positioning in Wireless Networks*. [Licentiate Thesis, Department of Electrical and Information Technology]. Lund University.

Total number of authors:
1

General rights
Unless other specific re-use rights are stated the following general rights apply:
Copyright and moral rights for the publications made accessible in the public portal are retained by the authors and/or other copyright owners and it is a condition of accessing publications that users recognise and abide by the legal requirements associated with these rights.
- Users may download and print one copy of any publication from the public portal for the purpose of private study or research.
- You may not further distribute the material or use it for any profit-making activity or commercial gain
- You may freely distribute the URL identifying the publication in the public portal

Read more about Creative commons licenses: https://creativecommons.org/licenses/

Take down policy
If you believe that this document breaches copyright please contact us providing details, and we will remove access to the work immediately and investigate your claim.

LUND UNIVERSITY

PO Box 117
221 00 Lund
+46 46-222 00 00

Download date: 17. Dec. 2025

Inertial Measurement Unit based Virtual Antenna Arrays
–
DoA Estimation and Positioning in Wireless Networks

Muhammad Atif Yaqoob

Lund 2016

Department of Electrical and Information Technology
Lund University
Box 118, SE-221 00 LUND
SWEDEN

This thesis is set in Computer Modern 10pt
with the LaTeX Documentation System

Series of licentiate and doctoral theses
No. 85
ISSN 1654-790X
ISBN 978-91-7623-748-9 (print)
ISBN 978-91-7623-749-6 (pdf)

© Muhammad Atif Yaqoob 2016
Printed in Sweden by *Tryckeriet i E-huset*, Lund.
April 2016.

Dedicated to
My Parents
and
My Lovely Wife

Abstract

Today we have different location based services available in a mobile phone or mobile station (MS). These services include: direction finding to nearby ATMs, locating favorite food restaurants, or finding any target destination. Similarly, we see different applications of the positioning and navigation systems in fire-fighting or other rescue operations. The common factor in almost all of the location based services is the system's ability to determine the user's current position, with reference to a floor plan or a navigation map. Current technologies are using sensor data measurements from one or more sensors, available to the positioning device, for positioning and navigation. Typical examples are radio based positioning such as global positioning system, inertial sensors based inertial navigation system, or camera based positioning systems. Different accuracy and availability conditions of the positioning and navigation solution can be obtained depending on the positioning algorithms and the available sensor information.

Nowadays, the focus of research in positioning and navigation has been mostly on the use of existing hardware infrastructure and low-cost solutions, such that the proposed technique can be deployed with ease and without extra infrastructure requirements as well as without any expensive sensor equipment. In this work, we investigate a novel idea for positioning using existing wireless networks and low-cost inertial sensor measurements available at the MS. We propose to use received baseband radio signal along with inertial sensor data, such as accelerometer and rate gyroscope measurements, for direction of arrival (DoA) estimation and positioning. The DoA information from different base stations or access points can be used to estimate the MS position using *triangulation* technique. Furthermore, due to size and cost restrictions it is difficult to have real antenna arrays at the MS, the idea of DoA estimation and positioning is proposed to be used with single antenna devices by using the so-called *virtual* antenna arrays.

We have presented our research results in three different papers. We provide measurement based results to perform a quantitative evaluation of DoA estimation using arbitrary virtual antenna arrays in 3-D; where a state-of-the-art high-resolution algorithm has been used for radio signal parameter estimation. Furthermore, we provide an extended Kalman filter framework to investigate the performance of unaided inertial navigation systems with 3-axis accelerometer and 3-axis rate gyroscope measurements, from a six-degrees-of-freedom inertial measurement unit. Using the extended Kalman filter framework, we provide results for position estimation error standard deviation with respect to integration time for an unaided inertial navigation system; where the effect of different stochastic errors noise sources in the inertial sensors measurements such as white Gaussian noise and bias instability noise is investigated. Also, we derive a closed form expression for Cramér-Rao lower bound to investigate DoA estimation accuracy for a far-field source using random antenna arrays in 3-D. The Cramér-Rao lower bound is obtained using known antenna coordinates as well as using estimated antenna coordinates, where the antenna coordinates are estimated with an uncertainty whose standard deviation is known. Furthermore, using Monte-Carlo simulations for random antenna arrays, we provide Cramér-Rao lower bound based performance evaluation of random 3-D antenna arrays for DoA estimation.

Preface

During my time with the Communications Engineering group at the department of Electrical and Information Technology, I have published three papers. These papers cover the main topic of this thesis and are listed below.

[1] M. A. Yaqoob, F. Tufvesson, A. Mannesson, and B. Bernhardsson, “Direction of arrival estimation with arbitrary virtual antenna arrays using low cost inertial measurement units,” in *2013 IEEE Int. Conf. on Communications Workshops (ICC)*, Budapest, Hungary, 2013, pp. 79-83.

[2] M. A. Yaqoob, A. Mannesson, B. Bernhardsson, N. R. Butt, and F. Tufvesson, “On the performance of random antenna arrays for direction of arrival estimation,” in *2014 IEEE Int. Conf. on Communications Workshops (ICC)*, Sydney, Australia, 2014, pp. 193-199.

[3] M. A. Yaqoob, A. Mannesson, N. R. Butt, and F. Tufvesson, “Source localization using virtual antenna arrays,” in *2015 Int. Conf. on Localization and GNSS (ICL-GNSS)*, Göteborg, Sweden, 2015, pp. 1-6.

The work has been performed in collaboration with the department of Automatic Control. I have been part of some related work, which resulted into further publications, whose contents are not included in this thesis.

[4] A. Mannesson, M. A. Yaqoob, F. Tufvesson, and B. Bernhardsson, “Radio and IMU based indoor positioning and tracking,” in *2012 19th Int. Conf. on Systems, Signals and Image Processing (IWSSIP)*, Vienna, Austria, 2012, pp. 32-35.

[5] A. Mannesson, B. Bernhardsson, M. A. Yaqoob, and F. Tufvesson, “Optimal virtual array length under position imperfections,” in *2014 IEEE 8th Sensor Array and Multichannel Signal Processing Workshop (SAM)*, A Coruña, Spain, 2014, pp. 5-8.

[6] A. Mannesson, M. A. Yaqoob, B. Bernhardsson, and F. Tufvesson, “Tightly Coupled Positioning and Multipath Radio Channel Tracking,” in *IEEE Trans. Aerosp. Electron. Syst.*, to be published.

Acknowledgements

Firstly, I am really thankful to my supervisor Prof. Fredrik Tufvesson and my co-supervisor Prof. Bo Bernhardsson, for giving me the opportunity of having post graduate studies. I have met really nice people during the course of time. I feel really humble to be around such a wonderful group of people, both at the department of Electrical and Information Technology as well as the department of Automatic Control, Lund University. The journey of my post-graduate studies was never an easy ride. The challenges at work, as well as, other personal issues could have been quite overwhelming. But, the timely support and guidance from different people around me really helped me achieve my goals of scientific learning and also helped me to deal with the everyday issues in general.

This thesis would not have been possible without the support and encouragement from my supervisor, Fredrik, who was always there during the ups and downs and provided me great help to achieve this milestone. Also, I am truly grateful to the support and encouragement I received from my co-supervisor, Bo Bernhardsson, for all the work I had done. My collaboration with Anders Mannesson, PhD student working at the Automatic Control department, was very exciting and helpful in many ways especially in the beginning of my work. I would also like to thank Dr. Fredrik Rusek for being my mentor, for one year, at the start of my studies. Your suggestions truly helped me deal with different issues regarding PhD studies. I also feel thankful to Prof. Buon Kiong Lau, director of the PhD studies. Annual meetings with him are helpful to ensure that the PhD studies have the right pace of work. I am also thankful to Prof. Ove Edfors, head of our research group, for always being very kind and lively person. I am grateful to my current and former colleagues at the department namely Dr. Taimoor, Dr. Rohit, Dr. Ghassan, Dr. Carl, Dr. Meifang, Jose, Nafiseh, Dr. Xiang, Joao, Dimitrios, Abdulaziz, Waqas, and Zachary as well as people in the administration especially Bertil, Josef, and Pia; all of you have made this a truly wonderful place to work.

This work is supported by the Excellence Center at Linköping-Lund in In-

formation Technology (www.elliit.liu.se) and by the Lund Center for Control of Complex Engineering Systems (www.lccc.lth.se) as well as the Swedish Research Council. The support is gratefully acknowledged.

I am also thankful to my Pakistani friends living in Lund. Their warmth and friendly presence has always been a real blessing while working away from the family. To name a few, I am very grateful for the lively time I spent with Taimoor Abbas, Naveed Butt, Farrukh Javed, Adeel Yasin, Usman Mirza, Sardar Sulaman, Waqas Khan, Yasser Sherazi, and Waqas Ahmad. By naming a few should not undermine the importance of all those people I have met and their names could not have been added due to space restrictions only. Thank you all.

Last but not the least, I am greatly thankful to my family for their never ending support and kindness during all the times. Also, my lovely wife who have brought more charm and comfort in my life. Thank you for everything.

Muhammad Atif Yaqoob

List of Acronyms and Abbreviations

2-D	Two Dimension
3-D	Three Dimension
6DoF	Six Degrees of Freedom
AD	Allan Deviation
ARW	Angle Random Walk
AV	Allan Variance
BI	Bias Instability
BS	Base Station
CRLB	Cramér-Rao Lower Bound
DoA	Direction of Arrival
EKF	Extended Kalman Filter
FIM	Fisher Information Matrix
GNSS	Global Navigation Satellite System
GPS	Global Positioning System
IMU	Inertial Measurement Unit
INS	Inertial Navigation System
LOS	Line of Sight

LS	Least Squares
MAP	Maximum A Posteriori
MEMS	Micro Electro-Mechanical Systems
ML	Maximum Likelihood
MS	Mobile Station
MSE	Mean Square Error
MUSIC	MUltiple SIgnal Classification
NLOS	Non-Line of Sight
pdf	probability density function
RCB	Robust Capon Beamformer
Rx	Receiver
SAGE	Space Alternating Generalized Expectation Maximization
SCB	Standard Capon Beamformer
Tx	Transmitter
VRW	Velocity Random Walk
WLS	Weighted Least Squares

Contents

Abstract **v**

Preface **vii**

Acknowledgements **ix**

List of Acronyms and Abbreviations **xi**

Contents **xiii**

I Overview of the Research Field **1**

1 Introduction **3**

1.1 Radio Based Positioning 5
1.2 Inertial Navigation System 6
1.3 Inertial and Radio Based Positioning 7
1.4 Thesis Objectives 8
1.5 Contributions 9

2 Positioning Using Inertial Measurement Units **11**

2.1 Inertial Measurement Unit 11
2.2 Reference Frames 12
2.3 Coordinate Transformation 13
  2.3.1 Euler angles 14
  2.3.2 Quaternions 14
2.4 Position Estimation using Dead Reckoning 15
  2.4.1 Orthogonal Coordinate System 15
  2.4.2 Deterministic Errors 17

2.4.3 Outlier Rejection and Low-pass Filtering 19
2.4.4 Movement Detection 22
2.4.5 Position and Attitude Initialization and Tracking . . 23
2.5 Positioning and Tracking using Extended Kalman Filter . . 26
2.5.1 IMU Data Modeling 26
2.5.2 Stochastic Errors 27
2.5.3 IMU Data Generation 31
2.5.4 Extended Kalman Filter 34
2.5.5 State Dynamics 35
2.5.6 Measurement Equation 38

3 Direction Of Arrival Estimation 41
3.1 Cramér-Rao Lower Bound 42
3.1.1 Arbitrary 3-D Antenna Arrays 43
3.1.2 Optimal Array Length 46
3.1.3 Hybrid-CRLB 46
3.2 DoA Estimation Methods 50
3.3 Robust DoA Estimation 51
3.3.1 Maximum A Posteriori Estimation 51
3.3.2 Robust Capon Beamforming 52
3.3.3 Robust Iterative Estimators 54

4 Positioning Using Angular Power Spectrum 55
4.1 Position Estimation Using Least Squares 56
4.2 Position Estimation Without Heading Information 57
4.3 Positioning in Non-Line of Sight 60

5 Conclusions and Future Work 63
5.1 Conclusions 63
5.2 Future Work 64

References 65

A FIM for the hybrid-CRLB 71

II Included Papers 75

PAPER I – Direction of Arrival Estimation with Arbitrary Virtual Antenna Arrays using Low Cost Inertial Measurement Units **79**
1 Introduction 81
2 Virtual Antenna Array 82
3 Array Coordinates 83
3.1 Attitude Estimation 83
3.2 Position Estimation 85
4 DoA Estimation 85
5 Measurement Setup 86
6 Results 87
7 Conclusion 92
References 92

PAPER II – On the Performance of Random Antenna Arrays for Direction of Arrival Estimation **97**
1 Introduction 99
2 Inertial Measurement Units 100
3 Extended Kalman Filter 100
3.1 State Update 101
3.2 Measurement Update 102
3.3 Simulation Parameters and Position Estimation . . . 103
4 Cramér Rao Lower Bound for DoA Estimation 105
4.1 CRLB with Known Antenna Positions 106
4.2 CRLB with Estimated Antenna Positions 107
5 Results and Discussion 112
6 Conclusion 113
References 114

PAPER III – Source Localization Using Virtual Antenna Arrays **119**
1 Introduction 121
2 IMU Data Generation 122
2.1 Random 3-D Antenna Array Coordinates 123
3 IMU Sensor Noise and Inertial Navigation System Simulation 125
3.1 Accelerometer Noise 126
3.2 Gyroscope Noise 130

- 3.3 Both Accelerometer and Gyroscope Noises 134
4 DoA Estimation using Monte Carlo Simulations 135
5 Summary and Conclusion 137
References 138

Part I

Overview of the Research Field

Chapter 1

Introduction

The field of positioning and navigation has been an interesting area of research for a long time. Today there are a large number of location based services available that require the users' current location in order to connect them to nearby points of interest (such as retail businesses, public facilities, or travel destinations), to be able to advise them of current conditions (e.g. traffic and weather), or to be able to provide routing and tracking services [1].

Depending on the user requirements, a complete navigation solution is required in applications where the user would be interested to find an optimal or shortest route to the destination. While in some other scenarios it is enough to determine one's current position in a given map or in an environment to enable any location based services. Whereas, for some other situations the user's tracking data might be crucial for any civil or military uses. The use of different common terms in this thesis are mentioned in the following text with their intended meaning. These terms might have been used for slightly different meanings in the literature as well.

Positioning: It is the process of determining current position of a user or a target in a given map or some reference frame, e.g., to identify the current position of a person in a building.

Navigation: It is the process to locate a user in a map, also suggest an optimal route for the user to reach a target position on the map, e.g., to navigate a fire-fighter from a smoke-filled room in a building to an exit point of the building, in a rescue operation.

Tracking: It is the process to do repeated positioning for a moving user or target object. Tracking is most often used in conjunction with dead reckoning; where user's current position is calculated using previously estimated positions, as well as, current measurements of speed and direction.

There are two fundamental methods used in the literature for navigation solutions, namely, position fixing and dead reckoning [2]. In position fixing, the absolute position of the object is computed using sensor data from external sources with known locations, e.g., global navigation satellite system (GNSS) based positioning where external satellite signals from known locations are used to estimate the position of the satellite receiver. Whereas in dead reckoning, the relative position of the object is estimated based on the user's initial position, speed and heading information, e.g., an inertial navigation system (INS) where accelerometers and gyroscopes are used to calculate the user's translational motion and rotational motion respectively. A thorough description of the subject concerning GNSS, INS, as well as their integration strategies can be found in different text books, such as [2, 3, 4, 5].

In this thesis, we propose a novel idea of mobile station (MS) position estimation for single antenna devices using direction of arrival (DoA) information of different base station (BS) signals. We evaluate the performance of virtual antenna arrays in terms of DoA estimation accuracy where the virtual array is created by tracking measurements of the MS (which includes an inertial measurement unit (IMU) and a receiver (Rx) antenna) in 3-D [6]. The antenna position estimates are obtained by dead reckoning using inertial sensor measurements, therefore, we investigate the performance evaluation of an unaided inertial navigation system. Using an extended Kalman filter (EKF), we propose a simple framework for calculating the error variance of the antenna positions estimates [7]. Furthermore, by adjusting the noise parameters for the white Gaussian noise and bias drift, the effect of different stochastic noise sources present in the IMU measurements is investigated [8].

This thesis outline is as follows. An overview of different positioning techniques, using radio signal measurements, is provided in section 1.1. A brief overview of inertial navigation systems is provided in section 1.2. In section 1.3, different integrated navigation approaches are described using radio and inertial sensor measurements. In Chapter 2, a detailed description about the use of inertial sensors data from a low-cost Micro Electro-Mechanical Systems (MEMS) based IMUs is provided, where the use of EKF is formulated for the performance evaluation of an unaided inertial navigation system with six degrees of freedom (6DoF). Chapter 3 provides necessary derivations to calculate the Cramér-Rao lower bound (CRLB) for DoA estimation accuracy using random antenna arrays in 3-D with known antenna positions. Also, a hybrid-CRLB is derived for the random 3-D antenna arrays when the true antenna positions are not known, but, the antenna positions are known with some a priori probability of the antenna positions about their nominal positions. Chapter 4 describes that the DoA estimates available at the MS can be directly employed to calculate the MS position using *'triangulation'*, a similar technique *'trilat-*

eration' is used in the Global Positioning System (GPS). Finally, Chapter 5 concludes this thesis and also provides possible directions for future work.

1.1 Radio Based Positioning

Using radio signal parameters, along with GPS some other approaches have also been proposed in the literature for positioning. The most common techniques are based on Time of Arrival (ToA), Received Signal Strength (RSS), and Direction of Arrival (DoA) measurements. All of these methods have their own advantages, as well as limitations. These techniques are briefly described below, while a more detailed discussion about these techniques can be found in [5, 9].

GNSS Based

GPS is used for positioning and navigation by using direct line of sight (LOS) radio signals from at least four satellites orbiting in the Earth orbit. Using GPS, the position of the satellite receiver is determined in a global coordinate system. Outdoors, GPS has proven to be a reliable solution with good accuracy. However, indoors or in urban canyons, the performance of the GPS receiver degrades as the received signal to noise and interference ratio deteriorates at the GPS receiver due to multipath propagation and fading effects. Furthermore, if the direct LOS signal to the GPS satellites is not available, then GPS data might not be available for positioning and tracking. In those scenarios where GPS signals are not available, some complementary sensor information, such as an INS, is often used to improve the navigation system performance.

Time of Arrival (ToA) Based

In ToA based positioning methods, precise time synchronization at both the transmitter (Tx) and receiver (Rx) clocks is required which demands the use of very stable clocks at the MS and the BS. In practice, it is difficult to have a high precision clock circuitry at the MS, as the device cost would then increase significantly. Although, for Time Difference of Arrival (TDoA) based positioning where difference of the different ToA measurements is used instead of direct ToA measurements, constraints on the clock synchronization between the MS and the BS can be relaxed. However, for better accuracy in TDoA measurements, higher signal bandwidth is required. The requirement of large bandwidth cannot be fulfilled in the current cellular systems and special hardware infrastructure must therefore be installed for better accuracy using the TDoA technique.

Received Signal Strength (RSS) Based

In RSS based positioning methods, the distances between the Tx and Rx are estimated using RSS measurements. Using three or more distance estimates corresponding to the RSS measurements, *trilateration* can be applied which gives position estimate. However, due to multipath fading (fast fading due to multipath propagation) and shadow fading (due to obstacles between the propagation paths), it is very hard to get reliable distance estimates using the RSS measurements. Another approach using the RSS measurements is to do fingerprinting. However, the use of large databases in fingerprinting based approaches requires very high computational effort, as well as, a calibration effort to get reliable fingerprints.

Direction of Arrival (DoA) Based

In DoA based techniques, using *triangulation*, DoA information of the LOS signal from a MS to different BSs is used to determine the MS position. The DoA information can be obtained by using an antenna array or through the use of antenna gain pattern of the Rx antenna. Due to increased hardware requirements in terms of multiple antenna elements and radio frequency (RF) chains, work in this area assumes that the DoA information is available at the BS only [10, 11, 12]. Subsequently, a central processing node which involves mutual information exchange between different BSs is required for the MS position estimation. Our work presented in this thesis also falls under the category of DoA based positioning. However, the DoA estimates of different BSs are obtained at the MS instead, where we propose to use a virtual antenna array for DoA estimation. The idea of using virtual antenna arrays is used in the field of wireless communication, especially for channel modeling and channel characterization purposes. Where, the virtual array can be made using a single antenna element and a single RF chain. In virtual antenna arrays, a single antenna element is moved to different antenna locations whose coordinates are known and the transmitted signal is then received at those locations, assuming that the propagation environment remains static during the measurement time (i.e., the time it takes to measure the transmitted signal at all the receive antenna positions).

1.2 Inertial Navigation System

An inertial navigation system (INS) is a self contained system and comprises of an IMU and a processing unit to process the inertial sensor measurements [2]. A high level block diagram description of an INS is shown in Figure 1.1.

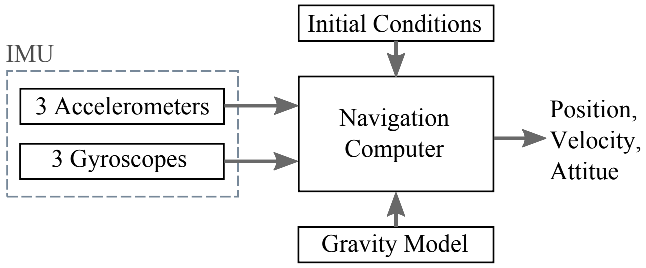

Figure 1.1: A high level block diagram description of an inertial navigation system.

The IMU usually has an accelerometer triad and a gyroscope triad, for 6DoF measurements of acceleration and angular velocity in an orthogonal coordinate system. In the navigation computer, dead reckoning is used to calculate the user's position and attitude estimates, where initial conditions of position and attitude are used along with the current acceleration and angular velocity measurements. To remove the gravity acceleration from the measured acceleration, a gravity model is also needed to estimate the device's net acceleration, i.e., the acceleration which is caused by the actual movement of the device. Single integration of acceleration and angular velocity measurements can provide velocity and attitude estimates. And further integration of velocity provides position estimate. However, due to error accumulation in the position and attitude estimates, it is important to note, that the use of INS alone is not a feasible solution for positioning and navigation over a long period of time, especially with low-cost MEMS based inertial sensors. A detailed description about the use of inertial sensor measurements for an INS is given in Chapter 2.

1.3 Inertial and Radio Based Positioning

The errors in the position estimates grow over time from a stand-alone INS; and the position estimates are reliable for a short period of time only. Whereas, the position estimates from a satellite based navigation system (e.g., GPS) relies on the direct path from the Earth orbiting satellites to obtain the position estimates. In areas where the direct path from the satellites gets blocked due to large buildings or other tall objects surrounding the GPS receiver, outage in the GPS system can be observed. Furthermore, relatively slower update rate is achieved with GPS as compared to INS, for the position estimates. Traditionally, one common solution, known as GPS/INS integration, has been a popular choice among researchers in the field of positioning and navigation due to the complementary features of these two techniques. Relatively slow updates of the position estimates from a satellite based navigation system (GPS) are combined with relatively fast updates of the position estimates from dead reckoning (INS); in a *loose*, *tight*, or *ultra-tight* integration [2]. The position estimates from the INS, which are relatively more accurate over short durations but drift to large errors over longer period of time, are periodically corrected/updated with more accurate absolute position estimates from the GPS.

We propose a novel approach to use the inertial and radio signal measurements. For a short random movement in 3-D, inertial sensor measurements are obtained along with the radio samples which are measured along the moved trajectory. We use measured radio signal to calculate the channel impulse response and the inertial sensor measurements provide estimated antenna array coordinates using dead reckoning. Finally, using radio signal parameter estimation algorithm, the DoA estimates are obtained at the MS side.

1.4 Thesis Objectives

Our thesis objective is to investigate positioning or localization solutions for single antenna devices, such as a modern day mobile phone or MS, which also includes a low-cost inertial measurement unit attached on to the device. In this thesis, we have studied positioning or localization problem under the context of using existing hardware infrastructure in the form of cellular network's base stations (BSs) or WLAN access points. Also, without using any external sensor information except the sensor measurements from already installed inertial sensors, which includes accelerometers and rate gyroscopes, and a radio receiver to measure the radio signals in a MS. The following research questions are addressed in the thesis to meet the above mentioned thesis objectives:

1. Using MEMS-based low-cost IMUs for the antenna array coordinates estimation and controlled scatterers for the different BSs, investigate measurement based performance analysis of virtual 3-D antenna arrays for DoA estimation.

2. Investigate the effect of stochastic errors noise sources, present in the IMU measurements, on to the position estimation error in an unaided INS for short integration times.

3. Study the effect of individual noise sources to determine the most significant stochastic error source in the IMU measurements for antenna position estimation using dead reckoning.

4. Using Monte-Carlo simulations for random 3-D antenna arrays, investigate the performance of random 3-D antenna arrays for DoA estimation using CRLB.

5. Investigate the DoA estimation performance degradation for random 3-D antenna arrays with antenna position errors where the errors are modeled as independent and Gaussian distributed at each antenna position.

1.5 Contributions

In [6, 7, 8], we have presented our results and discussed the research questions mentioned in section 1.4. Below is a brief summary of our contributions to the area of positioning and localization, for single antenna devices coupled with low-cost IMUs:

1. We perform a measurement based DoA estimation performance analysis, using low-cost IMUs for making random virtual antenna arrays, in an indoor environment [6]. The measurement results show that, using a high resolution SAGE algorithm, reasonably good DoA estimation accuracy can be achieved with random virtual antenna arrays [6].

2. We provide an EKF framework to estimate the position estimation error standard deviation for a 6DoF INS, where variance of the different stochastic errors noise sources such as angle/velocity random walk and bias instability noise, present in the IMU measurements, can be set to any specific values [7].

3. By using the EKF framework we show that if simple dead reckoning is used to estimate the antenna position coordinates, for averaging times of about 4-6 seconds, then angle random walk is the dominant error source in IMU measurements for a low-cost IMU [8].

4. To calculate the minimum achievable DoA estimation accuracy, we provide a closed form CRLB expression for a single far-field source [7]. Furthermore, by using the CRLB and Monte-Carlo simulations, we show that DoA estimation performance of a random 3-D antenna array improves significantly with increased array length and/or with increased signal to noise ratio [7].

5. We provide a closed form expression to calculate a hybrid-CRLB to calculate the DoA estimation accuracy where the antenna array coordinates are perturbed [7]. Furthermore, by using the hybrid-CRLB as well as

the standard CRLB, we show that after a specific integration time of about 3-4 seconds, the increase in the number of antenna elements does not provide significant improvement in the DoA estimation accuracy, because the growing position estimation error standard deviation affects more significantly on to the DoA estimation accuracy [7].

Chapter 2

Positioning Using Inertial Measurement Units

2.1 Inertial Measurement Unit

An inertial measurement unit most often comprises of an accelerometer triad and a gyroscope triad. The accelerometer triad provides acceleration measurements $\mathbf{a} \in \mathbb{R}^3$ along three Cartesian coordinate axes. Similarly, the gyroscope triad measures angular velocity $\boldsymbol{\omega} \in \mathbb{R}^3$ with respect to the three coordinate axes. Thus, the unit allows for a movement with 6DoF. Inertial measurement units (IMUs) are an integral part of inertial navigation systems (INSs) and are being used in different commercial and military applications, such as aircraft, unmanned aerial vehicles, satellites, and guided missiles. To measure the Earth's magnetic field and to assist computing the IMU heading or bearing angle, a magnetometer triad is also often installed on to the IMU platform along with the accelerometer triad and the rate gyroscope triad [13].

Furthermore, modern day technology has allowed the development of MEMS based IMUs which offer low weight and low-cost devices [13]. These MEMS based IMUs are now being considered for applications requiring the use of commercial or industry grade devices as well as where navigational grade or military grade performance is required. A typical arrangement of components of an IMU is shown in Figure 2.1.

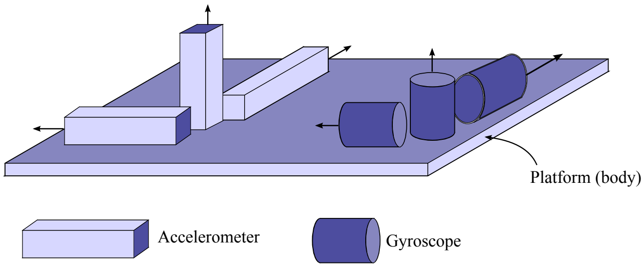

Figure 2.1: Arrangement of components of a strapdown inertial navigation system.

2.2 Reference Frames

Below is a brief summary of the reference frames used in this thesis. Each frame is an orthogonal, right handed coordinate frame. A more thorough description about reference frames can be found in [2, 4].

Inertial Frame

The Inertial Frame is a frame of reference in which classical laws of physics are in their simplest form, e.g., Newton's law of motion can be used in this frame assuming that all the fictitious forces (Coriolis force, centrifugal force, etc) are zero. More specifically, an inertial frame of reference is one in which the motion of a particle not subject to forces is in a straight line at constant speed. The accelerometers measure linear accelerations of the moving object in the inertial frame, while the gyroscopes measure angular velocity of the rotating object with respect to an arbitrary navigation frame.

Body Frame

Body Frame is a reference frame that is fixed with some rigid body or a platform. Figure 2.2 shows a body frame as (x_b, y_b, z_b) that is attached to a moving object or an IMU. The measurements from the IMU are then resolved in the body frame or body coordinates. When the IMU rotates the body frame also rotates with respect to a navigation frame (x_n, y_n, z_n) as shown in Figure 2.2.

Navigation Frame

Navigation Frame is a reference frame that can be defined on or close to the surface of earth such that its origin coincides with the origin of the inertial

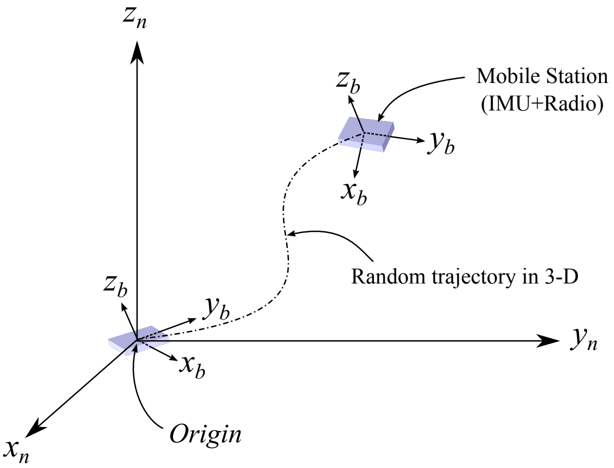

Figure 2.2: MS having an IMU and a radio receiver is moved along a random trajectory in 3-D with respect to a navigation coordinate system. The IMU accelerometer data measured in the body coordinates (x_b, y_b, z_b) can be transformed into the navigation coordinates (x_n, y_n, z_n) by using a rotation matrix $\mathbf{R}_b^n$; where the rotation matrix can be updated using IMU's angular velocity measurements.

sensors triad in the IMU. For a right handed navigation coordinate system, the z-axis points upward while the x-axis points towards east and the y-axis points towards true north.

2.3 Coordinate Transformation

The measured acceleration data $\mathbf{a}^b \in \mathbb{R}^3$ is in the body frame and need to transformed in to the navigation frame $\mathbf{a}^n \in \mathbb{R}^3$ for position, velocity and attitude estimation in the navigation coordinates. A rotation matrix $\mathbf{R}_b^n$ can be used to transform vector measurements from the body frame to the navigation frame as [4]

$$\mathbf{a}^n = \mathbf{R}_b^n \mathbf{a}^b, \tag{2.1}$$

where the rotation matrix $\mathbf{R}_b^n$ can be parametrized using the Euler angles or Quaternions as given below.

2.3.1 Euler angles

Euler angles provide three parameter representation to describe the orientation of a rigid body in a 3-D coordinate frame, and are typically denoted as (ψ, θ, ϕ), yaw, pitch, and roll angles. The Euler angles can also be used to describe the orientation of a reference frame with respect to another reference frame. Let's assume a reference frame that is considered to be fixed at some known or initial orientation (e.g., a navigation frame) while a second reference frame is assumed to be attached with a rigid body (e.g., a body frame). Also assuming that both the body frame and the navigation frame are aligned at some initial orientation, then any target orientation of the body frame, attached with a rigid body, can be achieved by a sequence of three elemental rotations. One possible rotation sequence, among twelve different rotation sequences, is z-y-x. This implies that the sequence of the three elemental rotations consists of: first rotation yaw (ψ) around the z-axis, second rotation pitch (θ) around the y-axis, and third rotation roll (ϕ) around the x-axis. The combination of these three rotation sequences will provide the moving body's reference frame orientation, represented as (ψ, θ, ϕ) yaw, pitch, and roll angles, with respect to the fixed or navigation frame.

Furthermore, to transform the body coordinates to the navigation coordinates, a rotation matrix which combines three rotation sequences described by the Euler angles can also be used. A rotation matrix $\mathbf{R}_b^n$ can e.g. be defined as a function of Euler angles (ψ, θ, ϕ), using a z-y-x rotation sequence, as [4]

$$\mathbf{R}_b^n = \begin{bmatrix} \cos\theta\cos\psi & -\cos\phi\sin\psi + \sin\phi\sin\theta\cos\psi & \sin\phi\sin\psi + \cos\phi\sin\theta\cos\psi \\ \cos\theta\sin\psi & \cos\phi\cos\psi + \sin\phi\sin\theta\sin\psi & -\sin\phi\cos\psi + \cos\phi\sin\theta\sin\psi \\ -\sin\theta & \sin\phi\cos\theta & \cos\phi\cos\theta \end{bmatrix}. \tag{2.2}$$

However, with Euler angles representation, we have singularities when the pitch (θ) approaches $\pm 90^\circ$ (north/south pole); the Euler angles can not be then uniquely determined with elemental rotations. To avoid these singularity problems, quaternions can be used for the attitude representation as given below.

2.3.2 Quaternions

A quaternion $\mathbf{q} = [q_0, q_1, q_2, q_3]^T$ is a four parameter representation to describe attitude of rigid body with reference to a 3-D coordinate system. A quaternion can be defined as

$$\mathbf{q} = \begin{bmatrix} q_0 \\ q_1 \\ q_2 \\ q_3 \end{bmatrix} = \begin{bmatrix} \cos(\vartheta/2) \\ u_x \sin(\vartheta/2) \\ u_y \sin(\vartheta/2) \\ u_z \sin(\vartheta/2) \end{bmatrix}, \tag{2.3}$$

where ϑ is a rotation angle (measured in radians) and $\mathbf{u} = [u_x, u_y, u_z]^T$ defines the axis of rotation. Quaternions are initialized with the rotation angle ϑ and rotation axis $\mathbf{u}$ as [14]

$$\vartheta = \cos^{-1}\left(\frac{\mathbf{a}^b \cdot \mathbf{g}^n}{\|\mathbf{a}^b\|\|\mathbf{g}^n\|}\right) \tag{2.4}$$

$$\mathbf{u} = \frac{\mathbf{a}^b \times \mathbf{g}^n}{\|\mathbf{a}^b\|\|\mathbf{g}^n\|\sin\vartheta}, \tag{2.5}$$

where $\mathbf{a}^b \in \mathbb{R}^3$ is the static acceleration in the body frame and $\mathbf{g}^n = [0, 0, 9.82]^T$ is the gravity acceleration in the navigation frame, measured in m/s^2. Also, $(\cdot)$ and $(\times)$ represent dot product and cross product in (2.4) and (2.5), respectively. Quaternions can also be used for rotation matrix parametrization to transform the body coordinates to navigation coordinates as

$$\mathbf{R_b^n}(\mathbf{q}) = \begin{bmatrix} q_0^2 + q_1^2 - q_2^2 - q_3^2 & 2q_1q_2 - 2q_0q_3 & 2q_1q_3 + 2q_0q_2 \\ 2q_1q_2 + 2q_0q_3 & q_0^2 - q_1^2 + q_2^2 - q_3^2 & 2q_2q_3 - 2q_0q_1 \\ 2q_1q_3 - 2q_0q_2 & 2q_2q_3 + 2q_0q_1 & q_0^2 - q_1^2 - q_2^2 + q_3^2 \end{bmatrix}. \tag{2.6}$$

More details about quaternions for attitude representation can be found in [4].

2.4 Position Estimation using Dead Reckoning

2.4.1 Orthogonal Coordinate System

To perform inertial navigation system calculations, the acceleration and angular velocity measurements must be represented with respect to an orthogonal coordinate system. Therefore, before using the IMU for any measurements, the IMU coordinate axes are labeled as shown in Figure 2.3, where body coordinate system (x_b, y_b, z_b) for a Phidget-1044 IMU is shown following a right-handed coordinate system.

With the Phidget-1044 IMU, a LabVIEW application has been used to observe the sign of the measured acceleration and angular velocity. For accelerometer measurements, orientation of the IMU was kept unchanged while moving the IMU along the different coordinate axes. For movements along the x-axis, positive acceleration is observed for the forward direction movements, and negative acceleration values were observed while moving the IMU towards the negative x-axis. For movements along the y-axis, negative acceleration values ware noted for the forward movements towards the positive y-axis, and vice versa. Similarly, For movements along the z-axis, positive acceleration values were noted for the forward movement towards the positive z-axis and vice

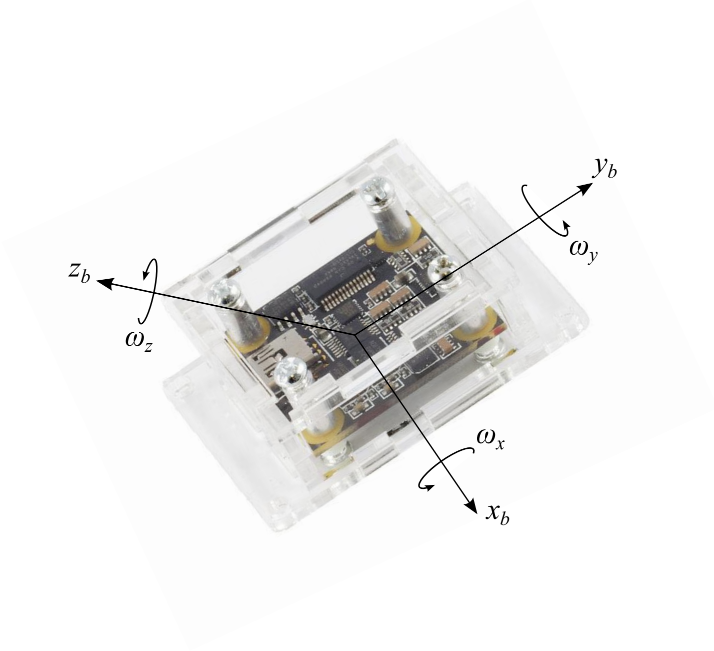

Figure 2.3: A MEMS based low-cost IMU used in our experiments, PhidgetSpatial_1044_0 [13]. It comprises of a 3-axis accelerometer triad, a 3-axis gyroscope triad, and a 3-axis magnetometer triad; installed onto a printed circuit board along with other components. The IMU is assembled into a plastic housing (chassis), which makes the IMU body coordinates referred as (x_b, y_b, z_b) which also corresponds to a right-handed coordinate system.

versa. In this work, all the calculations will be based on a right-handed coordinate system. Therefore, the acceleration data from the IMU measurements is translated using a translation matrix $\mathbf{A}_1$ as

$$\mathbf{A}_1 = \begin{bmatrix} 1 & 0 & 0 \\ 0 & -1 & 0 \\ 0 & 0 & 1 \end{bmatrix}. \tag{2.7}$$

Similarly, positive and negative rotation directions can be observed along each of the three sensitivity axes. A translation matrix $\mathbf{A}_2$ can also be defined to translate the measured data from the rate gyroscopes. From the Phidget-1044 gyroscope observations, the matrix $\mathbf{A}_2$ would translate the gyroscope data to a right-handed coordinate system.

$$\mathbf{A}_2 = \begin{bmatrix} -1 & 0 & 0 \\ 0 & 1 & 0 \\ 0 & 0 & -1 \end{bmatrix}. \tag{2.8}$$

Once the matrices $\mathbf{A}_1$ and $\mathbf{A}_2$ have been determined, the below equations can then be used to translate the measured acceleration $\mathbf{a}_{meas} \in \mathbb{R}^3$ and angular velocity $\boldsymbol{\omega}_{meas} \in \mathbb{R}^3$ data to an orthogonal right-handed Cartesian coordinate system, in the accelerometer cluster $\tilde{\mathbf{a}}^a = [\tilde{a}_x^a, \tilde{a}_y^a, \tilde{a}_z^a]^T$ and gyroscope cluster $\boldsymbol{\omega}^g = [\omega_x^g, \omega_y^g, \omega_z^g]^T$ coordinates.

$$\tilde{\mathbf{a}}^a = \mathbf{A}_1 \mathbf{a}_{meas}, \tag{2.9}$$

$$\boldsymbol{\omega}^g = \mathbf{A}_2 \boldsymbol{\omega}_{meas}. \tag{2.10}$$

2.4.2 Deterministic Errors

The acceleration measurements from a low-cost MEMS based IMU usually have some deterministic (fixed) errors as well. These errors include constant bias error, scale factor error, and cross axis-misalignment error. Figure 2.4 shows small angle errors between acceleration cluster coordinates (x_a, y_a, z_a) and the orthogonal body coordinates (x_b, y_b, z_b). For small misalignment errors along the accelerometer sensitivity axes, the measured acceleration signal from the acceleration cluster coordinates can be transformed into the orthogonal body coordinates following the relation $\mathbf{a}^b = \mathbf{T}_a^b \mathbf{a}^a$, where the transformation matrix $\mathbf{T}_a^b$ can be defined as [15, 16]

$$\mathbf{T}_a^b = \begin{bmatrix} 1 & -\alpha_{yz} & \alpha_{zy} \\ \alpha_{xz} & 1 & -\alpha_{zx} \\ -\alpha_{xy} & \alpha_{yx} & 1 \end{bmatrix}, \tag{2.11}$$

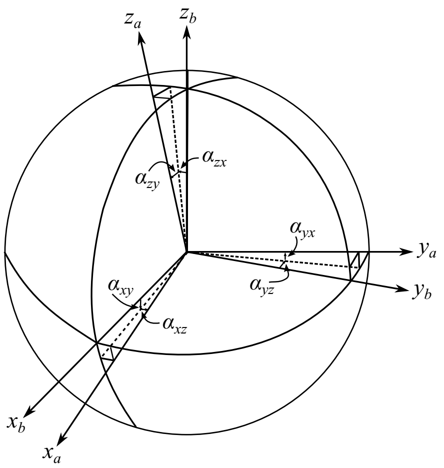

Figure 2.4: Acceleration coordinates (x_a, y_a, z_a) - body coordinates (x_b, y_b, z_b).

where α_{ij} is the rotation angle of the i^{th} accelerometer sensitivity axis around the j^{th} platform (body) axis. The observed signal from an accelerometer triad $\tilde{\mathbf{a}}^a \in \mathbb{R}^3$ can be modeled as [16, 3]

$$\tilde{\mathbf{a}}^a = \mathbf{K}_a(\mathbf{T}_a^b)^{-1}\mathbf{a}^b + \mathbf{b}_a + \mathbf{n}_a, \tag{2.12}$$

where $\mathbf{K}_a = diag(k_{x_a}, k_{y_a}, k_{z_a})$ is the unknown scaling of the accelerometer triad, $\mathbf{b}_a = [b_{x_a}, b_{y_a}, b_{z_a}]^T$ is constant bias error in the acceleration measurement, and $\mathbf{n}_a \in \mathbb{R}^3$ models a random noise vector. Similarly, the measurements from the rate gyroscope triad $\boldsymbol{\omega}^g \in \mathbb{R}^3$ are also affected by sensor errors, such as, constant bias, axis misalignment, and scale factor errors.

In [16], the authors have shown that the fixed errors in the accelerometer measurements can be estimated by taking static IMU measurements in 18 different orientations. A constant speed rate table can be used for the estimation of fixed errors in the rate gyroscope measurements and the calibration data is obtained by placing the IMU in different orientations on a three-axis rate table and the table is rotated at a constant speed.

In our work [6], we have used the same procedure as in [16] for accelerometer data calibration. For the gyroscope data, because of unavailability of the rate table at our premises, fixed errors in the rate gyroscope measurements are not estimated. We have estimated the parameters for two different sets of measurements. The calibration parameters are found to be negligible, for the IMU used in our experiments, as compared to the ones reported in [16]. For the sake of completeness, one of the estimated set of parameters are mentioned in Table 2.1. It can be noted from calibration parameters in Table 2.1, that the scale factor values are close to the ideal value of 1. Also, the constant bias errors and misalignment errors are found to be very small as well; where the ideal case would be to have these values close to zero.

Table 2.1: Estimated calibration parameters for the deterministic errors of Phidget-1044 IMU's accelerometer triad.

scale factor

k_x	k_y	k_z
1.0025	1.0022	0.9993

cross-coupling coefficient

α_{yz}	α_{zy}	α_{zx}
-0.0014	0.0001	0.0001

constant bias

b_x	b_y	b_z
0.0080	-0.0135	0.0053

A detailed study to investigate the effect of these fixed errors, if they are left uncalibrated, on to the position estimates has not been considered for this thesis and is left for future work. Finally, using the estimates of constant bias offset, axis misalignment errors, and the accelerometer triad scaling, the accelerometer data in the body coordinates of the IMU can be computed as

$$\mathbf{a}^b = \mathbf{T}_a^b \mathbf{K}^{-1}(\tilde{\mathbf{a}}^a - \mathbf{b}_a). \tag{2.13}$$

Figure 2.5 shows the accelerometer sensitivity axes and gyroscope sensitivity axes in a right-handed coordinate system. By using the calibrated scale-factor, bias, and cross-axis misalignment values, using (2.13), the accelerometer measurements in the body coordinates $\mathbf{a}^b$ can be obtained. In this work, since no calibration data is available for the rate gyroscope measurements, data $\boldsymbol{\omega}^g$ in orthogonal gyroscope cluster coordinates will be used directly.

2.4.3 Outlier Rejection and Low-pass Filtering

To decrease effects of high frequency noise in the IMU measurements, the measurements are filtered using a low-pass filter. It has been observed in the measurements, that when an IMU is picked up from a static position from a

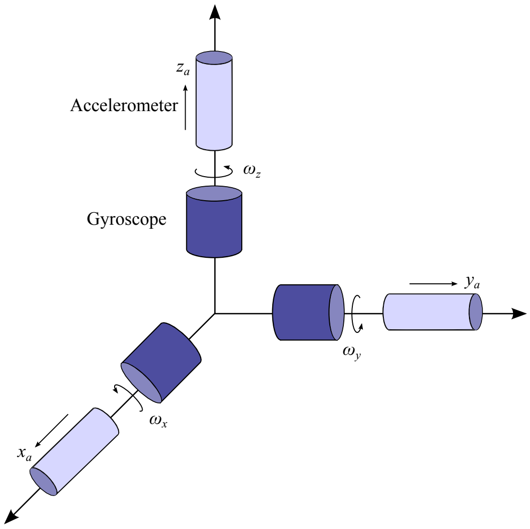

Figure 2.5: IMU sensor measurements in orthogonal coordinate system.

table or when it is put back on the table, very sharp peaks in the accelerometer data are present. Such a change in position of the device can be considered as an abrupt change and results in some sort of peakiness response in the measured accelerometer data, as experienced by the IMU's sensitivity axes. Using in-built functions in MATLAB, a direct-form finite impulse response filter is implemented to remove those unwanted spikes in the measured data. The sampling frequency, corresponding to the IMU data rate, is set as 250 Hz. Other parameters of the filter are set as given in Table 2.2. The same filter parameters are used for all the three coordinate axes measurements.

Table 2.2: Filter parameters for the accelerometer measurements.

Fs (sampling frequency of the data)	250 Hz
Fp (frequency at the end of pass band)	0.5 Hz
Fst (frequency at the start of stop band)	15 Hz
Ap (amount of ripple allowed in pass band)	0.0001 dB
As (attenuation in stop band)	40 dB

Similarly, measured data from the rate gyroscope is filtered using a low pass filter as well. The filter parameters for rate gyroscope measurements are given in Table 2.3. The same filter parameters are used for all the three coordinate

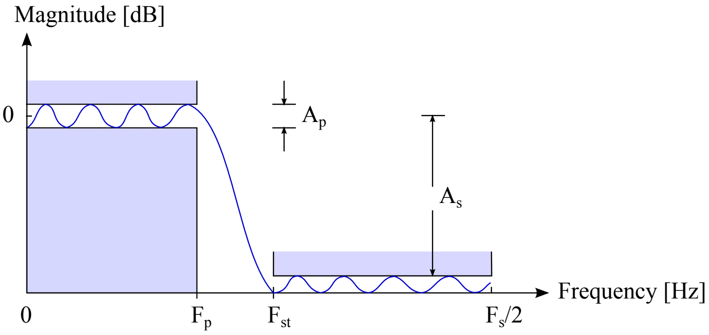
Magnitude [dB]
0
A_p
A_s
Frequency [Hz]
0
F_p
F_{st}
$F_s/2$

Figure 2.6: Design parameters of a lowpass filter in MATLAB.

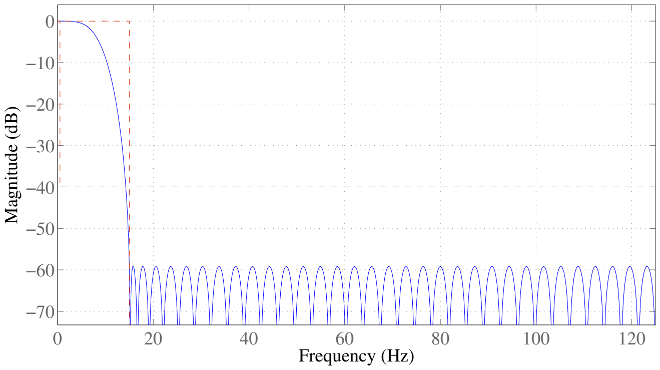

Figure 2.7: Magnitude response of the low-pass filter using filter parameters from Table 2.2.

axes measurements as well.

Table 2.3: Filter parameters for the gyroscope measurements.

Fs (sampling frequency of the data)	250 Hz
Fp (frequency at the end of pass band)	0.5 Hz
Fst (frequency at the start of stop band)	10 Hz
Ap (amount of ripple allowed in pass band)	0.01 dB
As (attenuation in stop band)	40 dB

2.4.4 Movement Detection

The estimated position error variance grows over integration time in an unaided inertial navigation system. In dead reckoning, to minimize the accumulated error in the position estimates, it is important to start position estimation when the actual movement starts. While the IMU is static, the gravity acceleration $\mathbf{g}^n = [0, 0, 9.82]^T$ m/s^2 is measured by the accelerometer triad where the gravity acceleration is projected onto the different coordinate axes. Ideally, the magnitude of the measured acceleration $\mathbf{a}^b = [a_x^b, a_y^b, a_z^b]^T$ in the body frame, while the IMU is held static, is given as

$$\|a\| = \sqrt{a_x^2 + a_y^2 + a_z^2} = 9.82\,\mathrm{m/s}^2. \tag{2.14}$$

It is important to mention that the acceleration in (2.14) is in the body coordinates, however, the superscript ^{b} has been omitted for simplicity. When the IMU is moved along some path, the measured acceleration is the sum of the the gravity acceleration and acceleration due to the applied force. By measuring the device's acceleration, the movement of the IMU can then be identified. A threshold detector can be used to detect if the magnitude of the measured acceleration is greater than the gravity acceleration. However, for robust estimate of the movement, a mean value of the acceleration magnitude is used instead, where mean of the acceleration magnitude is computed using N consecutive samples of the measurements as given below

$$\bar{a}_m = \frac{1}{N} \sum_{k=m}^{N+m-1} \|a_k\|, \tag{2.15}$$

where m defines the starting index of the samples in a given window of N samples, and k is the time index of the measurements. A sliding average $\bar{a}_m$ can be computed using the measured accelerations, for $m = 1, 2, \cdots$. A sliding window can provide better estimate of movement detection. The proposed scheme ensures that outlier in the acceleration data would not lead to false detection of the movement. After each iteration, the value of $\bar{a}_m$ is compared with a threshold to check if the IMU has moved or is static. In our measurements, it has been observed that by setting the window length as $N = 50$ and a threshold value of $g + 0.2$, movement detection can be made with good accuracy. The movement detection can be performed, after each iteration, as given below

$$\bar{a}_m \geq g + 0.2, \tag{2.16}$$

For some value of m, when the above mentioned threshold is detected, the movement start index k_s is determined for the position estimation with dead reckoning. The dead reckoning can be started from at-least $k_s = m$, assuming that $a_m \geq g + 0.2$. However, to ensure that no data samples are discarded which are related to the IMU movement, the movement start index is set as $k_s = m - N$ where N is length of the sliding window.

2.4.5 Position and Attitude Initialization and Tracking

In device tracking using inertial sensor data, firstly initial position and attitude values are defined and then any subsequent estimates of speed and heading are used to estimate the device's next position after the current time step.

Position Initialization

The position of a moving object can be tracked in a navigation coordinate system using inertial sensor measurements. If the user's initial position is known, it can be used as the user's initial position for tracking initialization. However, in this work, we assume that no initial position is given and the initial position of the IMU is assumed to be $O(0, 0, 0)$, the origin of a navigation coordinate system.

Attitude Initialization

Initial attitude of the IMU can be obtained using static accelerometer measurements and magnetometer measurements. The accelerometer measurements provide initial roll and pitch angles estimates and the magnetometer measures the Earth's magnetic field which can provide heading or yaw angle estimate.

In this work, initial attitude of the IMU is determined by using static accelerometer data only, and no magnetometer measurements are used. Therefore, no initial heading information of the IMU is known. Quaternions are initialized with the rotation angle ϑ and rotation axis $\mathbf{u}$ as given in (2.4)-(2.5), respectively. Furthermore, assuming that IMU remains static before the start of the movement, an average of the static acceleration in (2.4)-(2.5) provide a more accurate estimate of the initial attitude. The acceleration data samples can be averaged, starting from time index $k = 1$ to $k_s = N$, as shown below

$$\mathbf{a}^b_{avg} = \frac{1}{N} \sum_{k=1}^{N} \mathbf{a}^b_k, \tag{2.17}$$

where N is total number of acceleration data samples before the movement starts, $\mathbf{a}^b_k \in \mathbb{R}^3$ represents measured acceleration in the body coordinate system at time index k, and $\mathbf{a}^b_{avg} \in \mathbb{R}^3$ is the average value of the measured acceleration in the body coordinate system.

Position Update

Acceleration is defined as the rate of change of velocity and velocity is defined as the rate of change of position. Mathematically, they are defined as

$$v = \frac{\mathrm{d}p}{\mathrm{d}t}; \quad a = \frac{\mathrm{d}v}{\mathrm{d}t} = \frac{\mathrm{d}^2 p}{\mathrm{d}t^2} \tag{2.18}$$

Conversely, by integrating the measured acceleration, velocity can be computed; and by integrating the velocity, position displacement can be computed. This can also be expressed as

$$v = \int a \, \mathrm{d}t; \quad p = \int v \, \mathrm{d}t = \iint a \, \mathrm{d}t^2. \tag{2.19}$$

Assuming an object is moving with a constant acceleration a along a straight line. Also, assuming the initial velocity v_0 of the object is known, then final velocity v_t at any time t can be found as

$$v_t = \int_{t=0}^{t} a \, \mathrm{d}t = at + v_0. \tag{2.20}$$

Similarly, assuming the initial position p_0 is known, then position displacement at any time t can be computed as

$$p_t = \int_{t=0}^{t} v_t \, \mathrm{d}t = \int_{t=0}^{t} (at + v_0) \, \mathrm{d}t = \frac{1}{2} a t^2 + v_0 t + p_0. \tag{2.21}$$

The IMU position is calculated using initial conditions of position and velocity; and current measurement of acceleration data represented in the navigation coordinate system. Assuming the device is at rest in the beginning, then the initial position $\mathbf{p}_0 \in \mathbb{R}^3$ and the initial velocity $\mathbf{v}_0 \in \mathbb{R}^3$ can be initialized as zero vectors. Also, assuming the acceleration samples $\mathbf{a}_k^n \in \mathbb{R}^3$ are piecewise constant during sample time T_s, discrete time velocity $\mathbf{v}_{k+1}^n \in \mathbb{R}^3$ and position $\mathbf{p}_{k+1}^n \in \mathbb{R}^3$ samples can then be computed as

$$\begin{aligned} \mathbf{v}_{k+1}^n &= \mathbf{a}_k^n T_s + \mathbf{v}_k^n, && (2.22) \\ \mathbf{p}_{k+1}^n &= \frac{1}{2}\mathbf{a}_k^n T_s^2 + \mathbf{v}_k^n T_s + \mathbf{p}_k^n. && (2.23) \end{aligned}$$

Also, before the time-integration, the acceleration data need to be defined in the navigation coordinates. Using the rotation matrix $\mathbf{R}_b^n(\mathbf{q}_k)$, the measured acceleration $\mathbf{a}_k^b$ in the body coordinates can be transformed to the navigation coordinates. Further, the net acceleration due to the movement is obtained by subtracting the gravity acceleration $\mathbf{g}_k^n$ from the transformed acceleration as

$$\mathbf{a}_k^n = \mathbf{R}_b^n(\mathbf{q}_k)\,\mathbf{a}_k^b - \mathbf{g}_k^n. \tag{2.24}$$

Attitude Update

The rotation matrix $\mathbf{R}_b^n(\mathbf{q}_k)$ is obtained after every time step k, with the updated quaternion parameters $\mathbf{q}_k$. Let $\mathbf{q} = [1, 0, 0, 0]^T$ represents orientation of the device, with respect to navigation coordinate system, at time t. The time derivative of quaternion parameters can be approximated as [2, 17]

$$\frac{\mathrm{d}\mathbf{q}}{\mathrm{d}t} = \frac{1}{2}\mathbf{q} \otimes \begin{bmatrix} 0 \\ \boldsymbol{\omega} \end{bmatrix}, \tag{2.25}$$

where $\otimes$ represents quaternion multiplication. In the matrix multiplication form, the time derivative in (2.25) can be evaluated as

$$\frac{\mathrm{d}\mathbf{q}}{\mathrm{d}t} = \frac{1}{2}\bar{\boldsymbol{\Omega}}(\boldsymbol{\omega})\mathbf{q} = \frac{1}{2}\bar{\mathbf{Q}}(\mathbf{q})\boldsymbol{\omega}, \tag{2.26}$$

where

$$\bar{\boldsymbol{\Omega}}(\boldsymbol{\omega}) = \begin{bmatrix} 0 & -\omega_x & -\omega_y & -\omega_z \\ \omega_x & 0 & \omega_z & -\omega_y \\ \omega_y & -w_z & 0 & \omega_x \\ \omega_z & \omega_y & -\omega_x & 0 \end{bmatrix} \tag{2.27}$$

and

$$\bar{\mathbf{Q}}(\mathbf{q}) = \begin{bmatrix} -q_1 & -q_2 & -q_3 \\ q_0 & -q_3 & q_2 \\ q_3 & q_0 & -q_1 \\ -q_2 & q_1 & q_0 \end{bmatrix}. \tag{2.28}$$

Assuming the angular velocity is piecewise constant during the sample time T_s and by using Taylor series expansion, a closed-form expression for the quaternion update calculation can be found as [2, 17]

$$\mathbf{q}_{k+1} = e^{\frac{T_s}{2}\bar{\mathbf{\Omega}}(\boldsymbol{\omega}_k^g)}\mathbf{q}_k. \tag{2.29}$$

Furthermore, first-order approximation to the quaternion update equation can be found as [2]

$$\mathbf{q}_{k+1} = \mathbf{q}_k + \frac{T_s}{2}\bar{\mathbf{\Omega}}(\boldsymbol{\omega}_k^g)\mathbf{q}_k, \tag{2.30}$$

which also requires normalization of the quaternions as

$$\mathbf{q} := \frac{\mathbf{q}}{\|\mathbf{q}\|}. \tag{2.31}$$

The normalized quaternions are then used for updating the rotation matrix, and after each time step the updated rotation matrix is used to transform the measured acceleration from body coordinates to navigation coordinates. More details about the attitude tracking can be found in [18].

2.5 Positioning and Tracking using Extended Kalman Filter

2.5.1 IMU Data Modeling

The use of an accurate motion model to describe the target movement is very important in target tracking applications. Different motion models have been used in the literature to describe the movement of a target or an object. An overview of motion models, that can be applied for target tracking, can be found in [19]. To model motion dynamics, a model can be used which simply models the acceleration of the moving object as a zero-mean white Gaussian noise sequence; or another motion model can describe the acceleration process as a random walk process.

In our proposed application, the IMU coupled radio antenna device is assumed to be moving by free hand following any random trajectory. To model the said movement, we have considered the Singer acceleration model or simply the Singer model. The Singer model is defined as a target maneuvering model and it describes acceleration as a time correlated process [19, 20]. In the Singer model, the acceleration process can be generated as a first-order Gauss-Markov process, where, different values of the correlation time-constant and driving noise process variance can be used for the different movements. Using the Singer model, acceleration data samples can be generated independently, for each of the three coordinate axes, in a navigation coordinate system. For the Singer motion model, discrete time representation of the acceleration data samples can be defined as

$$\mathbf{a}_{k+1}^{n} = e^{-\alpha_a T_s}\mathbf{a}_k^n + \frac{1-e^{-\alpha_a T_s}}{\alpha_a}\boldsymbol{\nu}_{\mathbf{a}_k}, \tag{2.32}$$

where $\mathbf{a}_k^n \in \mathbb{R}^3$ is the acceleration data at time index k, T_s is the sample time, and $\alpha_a = 1/\tau_a$ where τ_a is time-constant value for the acceleration data. Also, the driving noise process $\boldsymbol{\nu}_{\mathbf{a}_k} \in \mathbb{R}^3$ is obtained, such that $\boldsymbol{\nu}_a \sim \mathcal{N}(0, \sigma^2_{\boldsymbol{\nu}_a}\mathbf{I}_3)$.

Similarly, angular velocity data is generated independently for the three coordinate axes by using the Singer model. The discrete time representation of the angular velocity data samples can be defined as

$$\boldsymbol{\omega}_{k+1} = e^{-\alpha_\omega T_s}\boldsymbol{\omega}_k + \frac{1-e^{\alpha_\omega T_s}}{\alpha_\omega}\boldsymbol{\nu}_{\omega_k}, \tag{2.33}$$

where $\boldsymbol{\omega}_k \in \mathbb{R}^3$ is the angular velocity at time index k, T_s is the sample time, and $\alpha_\omega = 1/\tau_\omega$ where τ_ω is time-constant value for the angular velocity data. Also, the driving noise process $\boldsymbol{\nu}_{\omega_k} \in \mathbb{R}^3$ is obtained, such that $\boldsymbol{\nu}_\omega \sim \mathcal{N}(0, \sigma^2_{\boldsymbol{\nu}_\omega}\mathbf{I}_3)$.

Furthermore, a single time-integration of the angular velocity data can provide device orientation tracking in 3-D with respect to the navigation coordinate system. Also, double time-integration of the simulated acceleration data samples can provide random 3-D trajectories in the navigation coordinate system. Also, in [7, 8], details about the use of different model parameters, such as τ_a and $\sigma^2_{\boldsymbol{\nu}_a}$, can be found to generate different random trajectories in 3-D.

2.5.2 Stochastic Errors

Allan Variance

Stochastic (random) errors also corrupt the inertial sensor measurements. Several authors have reported their work describing the error characterization and analysis of IMU data, see, e.g., [21, 22, 23, 24]. In the literature two techniques, namely Allan variance which is a time-domain analysis, and power spectrum decomposition which is a frequency-domain analysis, are commonly used to identify the stochastic noise sources in the IMU data. A brief overview of the different techniques used for stochastic error analysis can also be found in [21, 25].

We use the Allan variance to characterize the noise sources in the IMU data. Allan variance analysis was initially proposed to characterize the behavior of

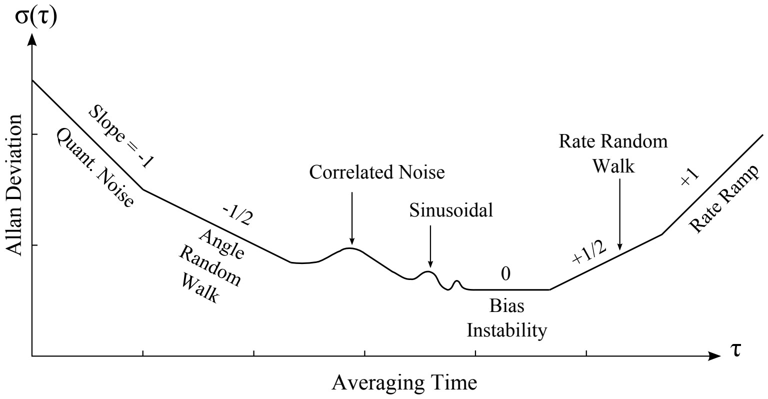

Figure 2.8: Sample plot for the Allan variance analysis [27].

different frequency oscillators [26]. But lately, it has been successfully applied to inertial sensor data [21, 27]. For the sake of completeness, a brief summary of the Allan variance analysis is given here. For the Allan variance analysis, measured data of acceleration and angular velocity is divided into N data bins, where each bin has data samples recorded over a period of τ seconds. An average value of data in each bin is then computed and can be denoted as a_{τ_i} for $i = 1, 2, \cdots, N$. Subsequently, using the set of averages $[a_{\tau_1}, a_{\tau_2}, \cdots, a_{\tau_N}]$, Allan variance corresponding to the averaging time τ is computed as

$$\mathrm{AV}(\tau) = \frac{1}{2(N-1)} \sum_{i=1}^{N-1} (a_{\tau_{i+1}} - a_{\tau_i})^2. \tag{2.34}$$

By taking square-root of the Allan variance values $\mathrm{AV}(\tau)$, Allan deviation values $\mathrm{AD}(\tau) = \sqrt{\mathrm{AV}(\tau)}$ are obtained, and then plotted in a log-log plot. Figure 2.8 shows a sample Allan deviation plot, where the different noise sources can be identified directly from the Allan deviation plot [27]. A brief overview of the most common stochastic errors in IMU measurements is given below.

Angle (Velocity) Random Walk

From the Allan deviation plot, a slope of -0.5 corresponds to the white Gaussian noise or constant power spectral density noise in the measured data. For the accelerometer data, the value of the Allan deviation plot at averaging time $\tau = 1\,\mathrm{s}$ is termed as velocity random walk (VRW). Whereas, for the rate gyroscope data, the value of the Allan deviation plot at averaging time $\tau = 1\,\mathrm{s}$ is termed as angle random walk (ARW). Furthermore, the white Gaussian noise for the accelerometer data $\mathbf{e}_a \in \mathbb{R}^3$ and the rate gyroscope data $\mathbf{e}_\omega \in \mathbb{R}^3$ can be modeled as

$$\begin{aligned} \mathbf{e}_{a,k} &\sim \mathcal{N}(\mathbf{0}, \mathbf{\Sigma}_a / T_s) && (2.35) \\ \mathbf{e}_{\omega,k} &\sim \mathcal{N}(\mathbf{0}, \mathbf{\Sigma}_\omega / T_s), && (2.36) \end{aligned}$$

where T_s is the sample time, $\mathbf{\Sigma}_a = diag(\sigma^2_{a_x}, \sigma^2_{a_y}, \sigma^2_{a_z})$ represents a diagonal covariance matrix for the accelerometer additive white Gaussian noise, and $\mathbf{\Sigma}_\omega = diag(\sigma^2_{\omega_x}, \sigma^2_{\omega_y}, \sigma^2_{\omega_z})$ represents a diagonal covariance matrix for the rate gyroscope additive white Gaussian noise. Without any loss of generality, assuming independent and identically distributed white Gaussian noise in all the three coordinate axes, the noise covariance matrix for the accelerometer data and the rate gyroscope data is then given as

$$\begin{aligned} \mathbf{\Sigma}_a &= \sigma_a^2 \mathbf{I}_3 && (2.37) \\ \mathbf{\Sigma}_\omega &= \sigma_\omega^2 \mathbf{I}_3, && (2.38) \end{aligned}$$

where σ_a and σ_ω represent the the value of the Allan deviation plots at $\tau = 1\,\mathrm{s}$ for the accelerometer data and the rate gyroscope data, respectively.

Bias Instability

From the Allan deviation plot, a slope of zero suggests the presence of pink noise or $1/f$ noise in the measured data. The source of this noise is the electronics or flicker noise. This is also known as bias instability (BI), where the bias is drifting over time. The bias instability is, however, bounded by the correlation time-constant of a first-order Gauss-Markov process. In the Allan deviation plot, slope of the plot becomes zero at the correlation time-constant of the Gauss-Markov process.

Similarly, assuming independent and identically distributed driving noise processes for all the three coordinate axes, without any loss of generality, the acceleration bias $\mathbf{a}_{b,k+1} \in \mathbb{R}^3$ and angular velocity bias $\boldsymbol{\omega}_{b,k+1} \in \mathbb{R}^3$ at time index $k+1$ can be found as

$$\begin{aligned} \mathbf{a}_{b,k+1} &= e^{-\alpha_{a_b} T_s} \mathbf{a}_{b,k} + \frac{1 - e^{-\alpha_{a_b} T_s}}{\alpha_{a_b}} \boldsymbol{\nu}_{a_{b,k}} && (2.39) \\ \boldsymbol{\omega}_{b,k+1} &= e^{-\alpha_{\omega_b} T_s} \boldsymbol{\omega}_{b,k} + \frac{1 - e^{-\alpha_{\omega_b} T_s}}{\alpha_{\omega_b}} \boldsymbol{\nu}_{\omega_{b,k}}, && (2.40) \end{aligned}$$

where $\alpha_{a_b} = 1/\tau_{a_b}$ and $\alpha_{\omega_b} = 1/\tau_{\omega_b}$ is inverse of the correlation time-constant for the acceleration bias and angular velocity bias drift processes, respectively. Further, $\boldsymbol{\nu}_{a_{b,k}} \in \mathbb{R}^3$ and $\boldsymbol{\nu}_{\omega_{b,k}} \in \mathbb{R}^3$ represent the driving noise vectors for the acceleration bias drift and angular velocity bias drift, at time index k, respectively; and are given as

$$\boldsymbol{\nu}_{a_{b,k}} \sim \mathcal{N}(\mathbf{0}, \sigma^2_{\nu_{a_b}} \mathbf{I}_3) \tag{2.41}$$

$$\boldsymbol{\nu}_{\omega_{b,k}} \sim \mathcal{N}(\mathbf{0}, \sigma^2_{\nu_{\omega_b}} \mathbf{I}_3), \tag{2.42}$$

Also, by letting $a_{d1} = e^{-\alpha_{a_b} T_s}$, $a_{d2} = (1 - e^{-\alpha_{a_b} T_s})/\alpha_{a_b}$ from (2.39), and $\omega_{d1} = e^{-\alpha_{\omega_b} T_s}$, $\omega_{d2} = (1 - e^{-\alpha_{\omega_b} T_s})/\alpha_{\omega_b}$ from (2.40): the variances $\sigma^2_{\nu_{a_b}}$ and $\sigma^2_{\nu_{\omega_b}}$ can be found as

$$\sigma^2_{\nu_{a_b}} = \frac{1 - a^2_{d1}}{a^2_{d2}} \sigma^2_{a_{BI}} \tag{2.43}$$

$$\sigma^2_{\nu_{\omega_b}} = \frac{1 - \omega^2_{d1}}{\omega^2_{d2}} \sigma^2_{\omega_{BI}}, \tag{2.44}$$

The values of $\sigma_{a_{BI}}$ and $\sigma_{\omega_{BI}}$ can be obtained using the Allan deviation plots of accelerometer and rate gyroscope data, respectively, as

$$\sigma_{a_{BI}} = \left.\frac{\sigma(\tau)}{0.664}\right|_{(\tau = \tau_{a_b})} \tag{2.45}$$

$$\sigma_{\omega_{BI}} = \left.\frac{\sigma(\tau)}{0.664}\right|_{(\tau = \tau_{\omega_b})}. \tag{2.46}$$

Rate Random Walk

In the Allan deviation plot, a slope of +0.5 is present for relatively longer averaging times which represents brown noise or noise with $1/f^2$ power spectrum. This noise process can be modeled as a random walk process. For the stochastic errors in the accelerometer and rate gyroscope data, a random walk process can be defined as

$$\mathbf{a}_{r,k+1} = \mathbf{a}_{r,k} + \boldsymbol{\nu}_{a_{r,k}} \tag{2.47}$$

$$\boldsymbol{\omega}_{r,k+1} = \boldsymbol{\omega}_{r,k} + \boldsymbol{\nu}_{\omega_{r,k}}, \tag{2.48}$$

where the variance of the driving noise processes $\boldsymbol{\nu}_{a_{r,k}}$ and $\boldsymbol{\nu}_{\omega_{r,k}}$ can be determined by using Allan deviation plots. Since the random walk process is not bounded in time, so the presence of this noise source becomes very critical in unaided inertial navigation systems performance. The effect of this type of noise source is more significant for relatively long averaging times, and its effect can be neglected for short averaging times.

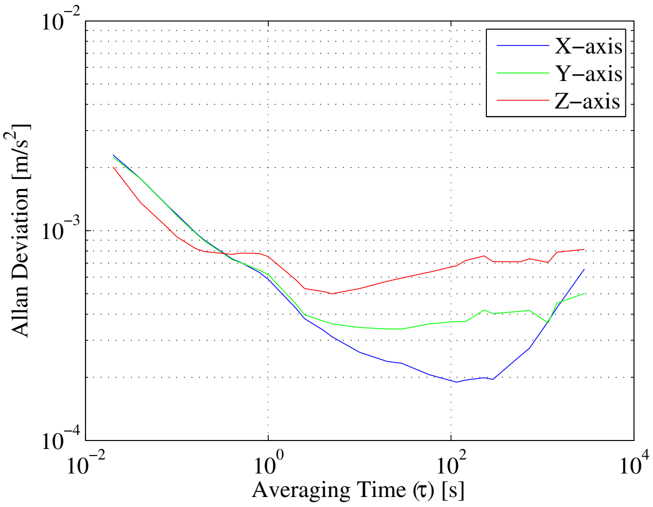

Figure 2.9: Allan deviation plot using measured accelerometer data with Phidget-1044 IMU.

Measured Allan Deviation Plots

In this work, Allan variance analysis is used to identify the stochastic errors present in the IMU measurements [7]. Static IMU data is recorded over a period of 8 hours to compute the Allan variance values. An example of Allan deviation plots using the static accelerometer data are shown in Figure 2.9. Similarly, for the rate gyroscope data, examples of Allan deviation plots are shown in Figure 2.10. Using the Allan deviation plot for the x-axis accelerometer data, we can identify that for short averaging times the slope of the curve is close to -0.5 and the slope becomes 0 at around $\tau = 115\,\mathrm{s}$, as shown in Figure 2.11. Similarly, for the x-axis rate gyroscope data, we can observe similar results as shown in Figure 2.11. Furthermore, the noise parameters for the stochastic error sources obtained from the Allan deviation plots are given in Table 2.4.

2.5.3 IMU Data Generation

Using the simulated angular velocity data (2.33), and the stochastic errors such as angle random walk (2.36) and bias instability (2.40), the angular velocity data in the gyroscope cluster coordinates is generated as

$$\boldsymbol{\omega}_k^g = \boldsymbol{\omega}_k + \boldsymbol{\omega}_{b,k} + \mathbf{e}_{\omega,k}, \tag{2.49}$$

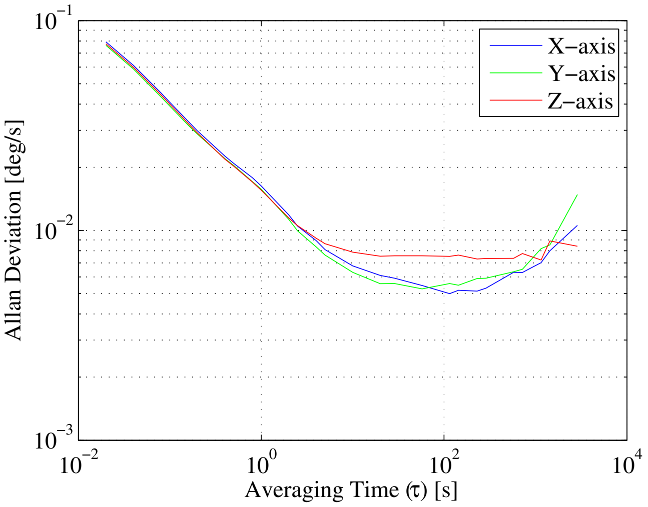

Figure 2.10: Allan deviation plot using measured rate gyroscope data with Phidget-1044 IMU.

Table 2.4: Noise Parameters for the stochastic noise sources present in the inertial sensor data. Noise parameters are obtained from static IMU data measurements as shown in Figure 2.11.

Accelerometer	
Velocity Random Walk	5.86×10^{-4} m/s/$\sqrt{s}$
Bias Instability	2.85×10^{-4} m/s^2 (at 115 s)
Gyroscope	
Angle Random Walk	1.63×10^{-2} deg /$\sqrt{s}$
Bias Instability	7.5×10^{-3} deg /s (at 115 s)

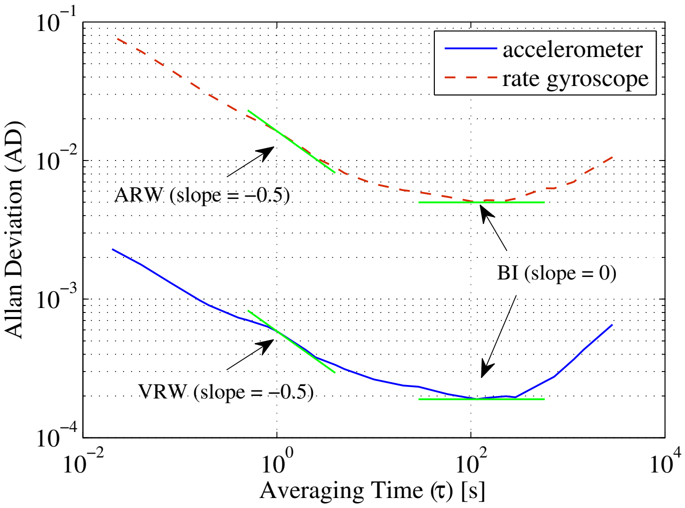

Figure 2.11: Allan deviation plots of the x-axis accelerometer and x-axis rate gyroscope data. A green line is plotted with a slope = -0.5 on top of the Allan deviation plots, where the line's y-intercept is located at $\tau = 1\,\mathrm{s}$. Also, at the minimum value of the Allan deviation plots, another green line is plotted with a slope = 0. From the plots it can be observed that the Allan deviation plots have a slope of approximately -0.5 for short averaging times and the slope then becomes close to 0; and finally the slope becomes positive for relatively long averaging times.

By using the angular velocity data $\boldsymbol{\omega}_k^g$, the quaternion parameters $\mathbf{q}_k$ can be computed using (2.29) as well as the rotation matrix $\mathbf{R}_b^n(\mathbf{q})$ as shown in (2.6). Finally, using the simulated accelerometer data in (2.32), and the stochastic errors such as velocity random walk in (2.35) and bias instability in (2.39), the accelerometer data in the body coordinates is generated as

$$\mathbf{a}_k^b = [\mathbf{R}_b^n(\mathbf{q}_k)]^T(\mathbf{a}_k^n + \mathbf{g}^n) + \mathbf{a}_{b,k} + \mathbf{e}_{a,k}, \tag{2.50}$$

where $[\mathbf{R}_b^n(\mathbf{q}_k)]^T$ is transpose of the rotation matrix, and $\mathbf{g}^n = [0, 0, 9.82]^T$ is the gravity acceleration in the navigation coordinate system and is measured in m/s^2. The generated IMU data in (2.49)-(2.50) is used in the EKF framework to determine the position estimation performance of an unaided inertial navigation system.

2.5.4 Extended Kalman Filter

A Kalman filter can be used to estimate state parameters by minimizing the mean squared error recursively, where a weighted average is used to update the parameter's estimates with new observations. The Kalman filter was proposed in 1960 [28] and since then it has been a very popular choice for researchers in state space based parameter estimation. The standard form of the Kalman filter can be used to estimate the system parameters of a linear system where the process noise and measurement noise are assumed to be Gaussian. Whereas, for a nonlinear system where the system dynamics or measurement equation is nonlinear, the state parameters can be estimated using an extended Kalman filter (EKF) [29, 30]. A nonlinear discrete-time system can be described as

$$\mathbf{x}_{k+1} = \mathbf{f}(\mathbf{x}_k, \mathbf{u}_k, \boldsymbol{\nu}_k) \tag{2.51}$$

$$\mathbf{y}_k = \mathbf{h}(\mathbf{x}_k, \mathbf{e}_k), \tag{2.52}$$

where $\mathbf{x}_k$ and $\mathbf{y}_k$ represent the state vector and measurement vector respectively at time index k. $\mathbf{f}(\mathbf{x}_k, \mathbf{u}_k, \boldsymbol{\nu}_k)$ models the state dynamics and $\mathbf{h}(\mathbf{x}_k, \mathbf{e}_k)$ relates the state parameters with the observations. $\boldsymbol{\nu}_k$ is the process noise, $\mathbf{e}_k$ is the measurement noise, and $\mathbf{u}_k$ is the control input defined at the time index k.

The filter operations can be performed iteratively after each time step. The different filter operations can be categorized into two main steps, the measurement update and the time update. A brief summary of the filter operations in these two steps can be described as [30]

Measurement Update:

$$\mathbf{K}_k = \mathbf{P}_{k|k-1}\mathbf{H}_k^T(\mathbf{H}_k\mathbf{P}_{k|k-1}\mathbf{H}_k^T + \mathbf{R}_k)^{-1} \tag{2.53}$$

$$\hat{\mathbf{x}}_{k|k} = \hat{\mathbf{x}}_{k|k-1} + \mathbf{K}_k(\mathbf{y}_k - \mathbf{h}(\hat{\mathbf{x}}_{k|k-1}, 0)) \tag{2.54}$$

$$\mathbf{P}_{k|k} = (\mathbf{I} - \mathbf{K}_k\mathbf{H}_k)\mathbf{P}_{k|k-1} \tag{2.55}$$

Time Update:

$$\hat{\mathbf{x}}_{k+1|k} = \mathbf{f}(\hat{\mathbf{x}}_{k|k}, \mathbf{u}_k, 0) \tag{2.56}$$

$$\mathbf{P}_{k+1|k} = \mathbf{F}_k \mathbf{P}_{k|k} \mathbf{F}_k^T + \mathbf{G}_k \mathbf{Q}_k \mathbf{G}_k^T, \tag{2.57}$$

where $\mathbf{K}_k$ is the filter gain, $\mathbf{R}_k$ is the measurement noise covariance, and $\mathbf{Q}_k$ is the process noise covariance, at time index k. The initial states of the filter can be configured as $\hat{\mathbf{x}}_{1|0} = \mathbb{E}(\mathbf{x}_0)$ and $\mathbf{P}_{1|0} = \text{Cov}(\mathbf{x}_0)$; where $\mathbb{E}(\mathbf{x}_0)$ is expected value of the state vector, and is used to initialize the state vector estimate at time index $k = 1$, when no measurements are available. Also, $\text{Cov}(\mathbf{x}_0)$ is covariance matrix of the state vector, and is used to initialize uncertainty in the state vector estimate at time index $k = 1$. The other parameters $\mathbf{F}_k$, $\mathbf{G}_k$, and $\mathbf{H}_k$ are Jacobians and can be computed as follows

$$\mathbf{F}_k = \left.\frac{\partial \mathbf{f}(\mathbf{x}_k, \mathbf{u}_k, \boldsymbol{\nu}_k)}{\partial \mathbf{x}_k}\right|_{(\hat{\mathbf{x}}_{k|k}, \mathbf{u}_k, 0)} \tag{2.58}$$

$$\mathbf{G}_k = \left.\frac{\partial \mathbf{f}(\mathbf{x}_k, \mathbf{u}_k, \boldsymbol{\nu}_k)}{\partial \boldsymbol{\nu}_k}\right|_{(\hat{\mathbf{x}}_{k|k}, \mathbf{u}_k, 0)} \tag{2.59}$$

$$\mathbf{H}_k = \left.\frac{\partial \mathbf{h}(\mathbf{x}_k, \mathbf{e}_k)}{\partial \mathbf{x}_k}\right|_{(\hat{\mathbf{x}}_{k|k-1}, 0)}. \tag{2.60}$$

2.5.5 State Dynamics

Using inertial sensor measurements to estimate the position, velocity, and attitude of the moving IMU, a state vector $\mathbf{x} = [\mathbf{p}, \mathbf{v}, \mathbf{a}, \mathbf{a}_b, \mathbf{q}, \boldsymbol{\omega}_b]^T$ is defined. The state vector comprises of position, velocity, acceleration, acceleration bias, quaternion, and angular velocity bias states respectively, defined in the navigation frame. Firstly, state dynamics for the different state parameters are determined to compute the time update operation in the EKF.

Position, Velocity, and Acceleration States

In this work, as shown in (2.32), the Singer model is used to model the acceleration process where an uncontrolled input $\boldsymbol{\nu}_{a_k}$ drives the acceleration process $\mathbf{a}_k$. Further, by using the acceleration process data in (2.22)-(2.23), estimated position and velocity data at time index $k+1$ along with the acceleration data are obtained as shown below.

$$\begin{aligned}
\mathbf{a}_{k+1} &= e^{-\alpha_a T_s}\mathbf{a}_k + \frac{1-e^{-\alpha_a T_s}}{\alpha_a}\boldsymbol{\nu}_{a_k} && (2.61)\\
\mathbf{v}_{k+1} &= \mathbf{v}_k + \frac{1-e^{-\alpha_a T_s}}{\alpha_a}\mathbf{a}_k + \frac{\alpha T_s - 1 + e^{-\alpha T_s}}{\alpha^2}\boldsymbol{\nu}_{a_k} && (2.62)\\
\mathbf{p}_{k+1} &= \mathbf{p}_k + \mathbf{v}_k T_s + \frac{\alpha_a T_s - 1 + e^{-\alpha_a T_s}}{\alpha_a^2}\mathbf{a}_k + \\
&\quad \frac{1-\alpha_a T_s + (\alpha_a T_s)^2/2 - e^{-\alpha_a T_s}}{\alpha_a^3}\boldsymbol{\nu}_{a_k}. && (2.63)
\end{aligned}$$

Quaternion States

Similarly, quaternion parameters can also be estimated at time index $k+1$ as shown in (2.64). However, the angular velocity data $\boldsymbol{\omega}^g$ might be corrupted by stochastic errors as shown in in (2.49). Assuming angle random walk and bias instability errors in the rate gyroscope data, the quaternion update can be computed as [7]

$$\mathbf{q}_{k+1} = e^{\frac{T_s}{2}\bar{\boldsymbol{\Omega}}(\boldsymbol{\omega}_k^g)}\mathbf{q}_k - \frac{T_s}{2}\bar{\mathbf{Q}}(\mathbf{q}_k)\boldsymbol{\omega}_{b,k} - \frac{T_s}{2}\bar{\mathbf{Q}}(\mathbf{q}_k)\boldsymbol{\nu}_{\omega,k}. \qquad (2.64)$$

Also note that, in the EKF framework, by using the measured angular velocity $\boldsymbol{\omega}^g$ as a controlled input in the system model, the white Gaussian noise $\mathbf{e}_{\omega,k}$ in the angular velocity measurements is then used as an uncontrolled process noise input $\boldsymbol{\nu}_{\omega,k}$, that is, $\boldsymbol{\nu}_{\omega,k} = \mathbf{e}_{\omega,k}$.

Acceleration and Angular Velocity Bias States

The state dynamics for the acceleration and angular velocity bias states are used as given in (2.39)-(2.40).

State Update

Finally, using the state dynamics as defined in (2.61)-(2.64) and (2.39)-(2.40), the time update of unaided inertial navigation system is computed. The time update for the EKF can be described as

$$\begin{pmatrix} \hat{\mathbf{p}}_{k+1|k} \\ \hat{\mathbf{v}}_{k+1|k} \\ \hat{\mathbf{a}}_{k+1|k} \\ \hat{\mathbf{a}}_{b,k+1|k} \\ \hat{\mathbf{q}}_{k+1|k} \\ \hat{\boldsymbol{\omega}}_{b,k+1|k} \end{pmatrix} =$$

$$\begin{pmatrix} \mathbf{I}_3 & T_s\mathbf{I}_3 & \frac{\alpha T_s - 1 + e^{-\alpha T_s}}{\alpha_a^2}\mathbf{I}_3 & \mathbf{0} & \mathbf{0} & \mathbf{0} \\ \mathbf{0} & \mathbf{I}_3 & \frac{1-e^{-\alpha_a T_s}}{\alpha_a}\mathbf{I}_3 & \mathbf{0} & \mathbf{0} & \mathbf{0} \\ \mathbf{0} & \mathbf{0} & e^{-\alpha_a T_s}\mathbf{I}_3 & \mathbf{0} & \mathbf{0} & \mathbf{0} \\ \mathbf{0} & \mathbf{0} & \mathbf{0} & e^{-\alpha_{a_b} T_s}\mathbf{I}_3 & \mathbf{0} & \mathbf{0} \\ \mathbf{0} & \mathbf{0} & \mathbf{0} & \mathbf{0} & e^{\frac{T_s}{2}\bar{\mathbf{\Omega}}(\boldsymbol{\omega}_k^g)} & -\frac{T_s}{2}\bar{\mathbf{Q}}(\hat{\mathbf{q}}_{k|k}) \\ \mathbf{0} & \mathbf{0} & \mathbf{0} & \mathbf{0} & \mathbf{0} & e^{-\alpha_{\omega_b} T_s}\mathbf{I}_3 \end{pmatrix} \begin{pmatrix} \hat{\mathbf{p}}_{k|k} \\ \hat{\mathbf{v}}_{k|k} \\ \hat{\mathbf{a}}_{k|k} \\ \hat{\mathbf{a}}_{b,k|k} \\ \hat{\mathbf{q}}_{k|k} \\ \hat{\boldsymbol{\omega}}_{b,k|k} \end{pmatrix}. \tag{2.65}$$

In the time update step, estimation error covariance matrix $\mathbf{P}$ is updated as well along with the state parameters. To calculate the matrix $\mathbf{P}_{k+1|k}$, process noise covariance matrix $\mathbf{Q}_k$ is calculated as shown below

$$\mathbf{Q}_k = \begin{bmatrix} \sigma_{\nu_a}^2\mathbf{I}_3 & \mathbf{0} & \mathbf{0} & \mathbf{0} \\ \mathbf{0} & \sigma_{\nu_{a_b}}^2\mathbf{I}_3 & \mathbf{0} & \mathbf{0} \\ \mathbf{0} & \mathbf{0} & \sigma_{\nu_\omega}^2\mathbf{I}_3 & \mathbf{0} \\ \mathbf{0} & \mathbf{0} & \mathbf{0} & \sigma_{\nu_{\omega_b}}^2\mathbf{I}_3 \end{bmatrix}, \tag{2.66}$$

where $\sigma_{\nu_a}^2, \sigma_{\nu_{a_b}}^2, \sigma_{\nu_\omega}^2$, and $\sigma_{\nu_{\omega_b}}^2$ represent variance of the noise process that drives the acceleration data, variance of the noise process that drives the acceleration bias drift, variance of the white Gaussian noise in the angular velocity measurements, and variance of the noise process that drives the angular velocity bias drift, respectively. Further, using the state dynamics in (2.61)-(2.64) and (2.39)-(2.40), the scaling matrix $\mathbf{G}_k$ that translates effect of the process noise on to the parameter estimates is given as

$$\mathbf{G}_k = \begin{pmatrix} \frac{1-\alpha_a T_s + (\alpha_a T_s)^2/2 - e^{-\alpha_a T_s}}{\alpha_a^3}\mathbf{I}_3 & \mathbf{0} & \mathbf{0} & \mathbf{0} \\ \frac{\alpha_a T_s - 1 + e^{-\alpha_a T_s}}{\alpha_a^2}\mathbf{I}_3 & \mathbf{0} & \mathbf{0} & \mathbf{0} \\ \frac{1-e^{-\alpha_a T_s}}{\alpha_a}\mathbf{I}_3 & \mathbf{0} & \mathbf{0} & \mathbf{0} \\ \mathbf{0} & \frac{1-e^{-\alpha_{a_b} T_s}}{\alpha_{a_b}}\mathbf{I}_3 & \mathbf{0} & \mathbf{0} \\ \mathbf{0} & \mathbf{0} & -\frac{T_s}{2}\bar{\mathbf{Q}}(\hat{\mathbf{q}}_{k|k}) & \mathbf{0} \\ \mathbf{0} & \mathbf{0} & \mathbf{0} & \frac{1-e^{-\alpha_{\omega_b} T_s}}{\alpha_{\omega_b}}\mathbf{I}_3 \end{pmatrix}. \tag{2.67}$$

Also, the state transition matrix $\mathbf{F}_k$ is found as

$$\mathbf{F}_k = \begin{pmatrix} \mathbf{I}_3 & T_s\mathbf{I}_3 & \frac{\alpha_a T_s - 1 + e^{-\alpha_a T_s}}{\alpha_a^2}\mathbf{I}_3 & \mathbf{0} & \mathbf{0} & \mathbf{0} \\ \mathbf{0} & \mathbf{I}_3 & \frac{1-e^{-\alpha_a T_s}}{\alpha_a}\mathbf{I}_3 & \mathbf{0} & \mathbf{0} & \mathbf{0} \\ \mathbf{0} & \mathbf{0} & e^{-\alpha_a T_s}\mathbf{I}_3 & \mathbf{0} & \mathbf{0} & \mathbf{0} \\ \mathbf{0} & \mathbf{0} & \mathbf{0} & e^{-\alpha_{a_b} T_s}\mathbf{I}_3 & \mathbf{0} & \mathbf{0} \\ \mathbf{0} & \mathbf{0} & \mathbf{0} & \mathbf{0} & e^{\frac{T_s}{2}\bar{\mathbf{\Omega}}(\boldsymbol{\omega}_k^g)} & -\frac{T_s}{2}\bar{\mathbf{Q}}(\hat{\mathbf{q}}_{k|k}) \\ \mathbf{0} & \mathbf{0} & \mathbf{0} & \mathbf{0} & \mathbf{0} & e^{-\alpha_{\omega_b} T_s}\mathbf{I}_3 \end{pmatrix}. \tag{2.68}$$

2.5.6 Measurement Equation

The measurement data vector $\mathbf{y}_k \in \mathbb{R}^3$ contains accelerometer measurements, in the body frame, at time index k. The measurement function $\mathbf{h}(\mathbf{x}_k, \mathbf{e}_k)$ relates the state vector parameters with the measurement data vector as shown below

$$\mathbf{y}_k = \left(\mathbf{R}_b^n(\mathbf{q}_k)\right)^T (\mathbf{a}_k + \mathbf{g}^n) + \mathbf{a}_{b,k} + \mathbf{e}_{a,k}, \tag{2.69}$$

where $\mathbf{a}_k \in \mathbb{R}^3$ is the movement based acceleration in the navigation frame, $\mathbf{g}^n \in \mathbb{R}^3$ is gravity acceleration in the navigation frame, $\mathbf{a}_{b,k} \in \mathbb{R}^3$ represents the bias drift in the accelerometer measurements in the body frame, and $\mathbf{e}_{a,k} \in \mathbb{R}^3$ is the additive noise in the accelerometer measurements in the body frame, at time index k. The rotation matrix $\left(\mathbf{R}_b^n(\mathbf{q}_k)\right)^T$, parametrized with the quaternions $\mathbf{q}_k$, transforms acceleration from the navigation frame to the body frame, at time index k.

The measurement noise is modeled such that $\mathbf{e}_a \sim \mathcal{N}(\mathbf{0}, diag(\sigma_{a_x}^2, \sigma_{a_y}^2, \sigma_{a_z}^2))$, where, $\sigma_{a_x}^2, \sigma_{a_y}^2$, and $\sigma_{a_z}^2$ represent additive white Gaussian noise variance in the accelerometer measurements for the xyz-coordinate axes. Also note that, as described in Section 2.5.2, variance of the white Gaussian noise in the accelerometer measurements can be estimated from the Allan deviation plot. Furthermore, without any loss of generality, assuming similar additive white Gaussian noise variance σ_a^2 for each of the three coordinate axes, the measurement noise covariance matrix can be set as $\mathbf{R}_k = \sigma_a^2\mathbf{I}_3$.

The measurement residual $\mathbf{y}_k - \mathbf{h}(\hat{\mathbf{x}}_{k|k-1}, 0)$ is computed by calculating the difference between the measured data $\mathbf{y}_k$ and the predicted measurement $\mathbf{h}(\hat{\mathbf{x}}_{k|k-1}, 0)$, where the latter can be obtained using (2.69) as

$$
\begin{aligned}
\mathbf{h}(\hat{\mathbf{x}}_{k|k-1},0) &= (\mathbf{R}_b^n(\hat{\mathbf{q}}_{k|k-1}))^T\mathbf{g}^n + \\
&\quad \begin{pmatrix}\mathbf{0}_3 & \mathbf{0}_3 & (\mathbf{R}_b^n(\hat{\mathbf{q}}_{k|k-1}))^T & \mathbf{I}_3 & \mathbf{0}_{3\times 4} & \mathbf{0}_3\end{pmatrix}\begin{pmatrix}\hat{\mathbf{p}}_{k|k-1}\\ \hat{\mathbf{v}}_{k|k-1}\\ \hat{\mathbf{a}}_{k|k-1}\\ \hat{\mathbf{a}}_{b,k|k-1}\\ \hat{\mathbf{q}}_{k|k-1}\\ \hat{\boldsymbol{\omega}}_{b,k|k-1}\end{pmatrix}.
\end{aligned}
\tag{2.70}
$$

Similarly, using the measurement function described in (2.69), the matrix $\mathbf{H}_k$ can be computed as

$$
\mathbf{H}_k = \begin{pmatrix}\mathbf{0}_3 & \mathbf{0}_3 & (\mathbf{R}_b^n(\hat{\mathbf{q}}_{k|k-1}))^T & \mathbf{I}_3 & \mathbf{R}'(\hat{\mathbf{a}}_{k|k-1},\hat{\mathbf{q}}_{k|k-1},\mathbf{g}^n) & \mathbf{0}_3\end{pmatrix}, \tag{2.71}
$$

where

$$
\mathbf{R}'(\hat{\mathbf{a}}_{k|k-1},\hat{\mathbf{q}}_{k|k-1},\mathbf{g}^n) \triangleq \left.\frac{\partial \mathbf{h}(\mathbf{x}_k,0)}{\partial \mathbf{q}}\right|_{(\hat{\mathbf{x}}_{k|k-1},0)}. \tag{2.72}
$$

The matrix $\mathbf{R}'(\hat{\mathbf{a}}_{k|k-1},\hat{\mathbf{q}}_{k|k-1},\mathbf{g}^n)$ is computed as

$$
\mathbf{R}'(\hat{\mathbf{a}}_{k|k-1},\hat{\mathbf{q}}_{k|k-1},\mathbf{g}^n) = 2\begin{pmatrix} r_{11} & r_{12} & r_{13} & r_{14}\\ r_{21} & r_{22} & r_{23} & r_{24}\\ r_{31} & r_{32} & r_{33} & r_{34}\end{pmatrix}, \tag{2.73}
$$

where the different matrix elements are found as

$$
\begin{aligned}
r_{11} &= \hat{q}_0(\hat{a}_x+g_x^n)+\hat{q}_3(\hat{a}_y+g_y^n)-\hat{q}_2(\hat{a}_z+g_z^n) && (2.74)\\
r_{12} &= \hat{q}_1(\hat{a}_x+g_x^n)+\hat{q}_2(\hat{a}_y+g_y^n)+\hat{q}_3(\hat{a}_z+g_z^n) && (2.75)\\
r_{13} &= -\hat{q}_2(\hat{a}_x+g_x^n)+\hat{q}_1(\hat{a}_y+g_y^n)-\hat{q}_0(\hat{a}_z+g_z^n) && (2.76)\\
r_{14} &= -\hat{q}_3(\hat{a}_x+g_x^n)+\hat{q}_0(\hat{a}_y+g_y^n)+\hat{q}_1(\hat{a}_z+g_z^n) && (2.77)\\
r_{21} &= -\hat{q}_3(\hat{a}_x+g_x^n)+\hat{q}_0(\hat{a}_y+g_y^n)+\hat{q}_1(\hat{a}_z+g_z^n) && (2.78)\\
r_{22} &= \hat{q}_2(\hat{a}_x+g_x^n)-\hat{q}_1(\hat{a}_y+g_y^n)+\hat{q}_0(\hat{a}_z+g_z^n) && (2.79)\\
r_{23} &= \hat{q}_1(\hat{a}_x+g_x^n)+\hat{q}_2(\hat{a}_y+g_y^n)+\hat{q}_3(\hat{a}_z+g_z^n) && (2.80)\\
r_{24} &= -\hat{q}_0(\hat{a}_x+g_x^n)-\hat{q}_3(\hat{a}_y+g_y^n)+\hat{q}_2(\hat{a}_z+g_z^n) && (2.81)\\
r_{31} &= \hat{q}_2(\hat{a}_x+g_x^n)-\hat{q}_1(\hat{a}_y+g_y^n)+\hat{q}_0(\hat{a}_z+g_z^n) && (2.82)\\
r_{32} &= \hat{q}_3(\hat{a}_x+g_x^n)-\hat{q}_0(\hat{a}_y+g_y^n)-\hat{q}_1(\hat{a}_z+g_z^n) && (2.83)\\
r_{33} &= \hat{q}_0(\hat{a}_x+g_x^n)+\hat{q}_3(\hat{a}_y+g_y^n)-\hat{q}_2(\hat{a}_z+g_z^n) && (2.84)\\
r_{34} &= \hat{q}_1(\hat{a}_x+g_x^n)+\hat{q}_2(\hat{a}_y+g_y^n)+\hat{q}_3(\hat{a}_z+g_z^n). && (2.85)
\end{aligned}
$$

The subscript $(\hat{\cdot})_{k|k-1}$ with acceleration and quaternion parameters estimates have been omitted for simplicity, i.e., $\hat{\mathbf{a}}_{k|k-1} = [\hat{a}_x, \hat{a}_y, \hat{a}_z]^T$ and $\hat{\mathbf{q}}_{k|k-1} = [\hat{q}_0, \hat{q}_1, \hat{q}_2, \hat{q}_3]^T$.

Chapter 3

Direction Of Arrival Estimation

Sensor array signal processing has been an active area of research for many years [31]. Estimation of signal parameters by using an array of sensors has enabled many applications in the field of mobile communications, radar, sonar, astronomy, seismology, and medical imaging. Antenna arrays at Rx can be employed for received radio signal parameter estimation, e.g., DoA, time delay, Doppler shift, and complex signal amplitude [32]. Using the estimated values of the DoA and other signal parameters, the LOS path and other reflected paths for the received radio signal can be identified for radio channel modeling and characterization purposes. Accurate channel models are used to improve the network capacity, to increase the mobile user data rates, and to increase the overall Quality-of-Service for the mobile users in a wireless communication network [33]. Furthermore, DoA estimates can also be used for MS position estimation in a wireless communication network, see [12] for a review of the different techniques for MS positioning. For a straightforward solution, DoA information from at least two LOS base stations is required to estimate the MS position in 2-D, and three base stations can provide the position in 3-D [10, 11, 34].

In order to have the DoA measurements at the Rx side, the need for extra hardware in terms of antenna elements and RF chains demands a complex as well as a costly solution for positioning. Our focus in this work is to estimate the DoA at the MS side by employing a virtual antenna array. A virtual antenna array can be made by moving the antenna element to different positions along with measuring the received radio signal at those locations, assuming that the propagation environment remains static during the whole measurement time [33]. The antenna locations are usually controlled with the help of a controller to have precise movements, because, the antenna position coordinates will be used to compute the array response vector or the array steering vector. We propose that the Rx antenna could be coupled with an IMU, such a setup is commonly available in modern day's cell phones. A virtual antenna array could then be realized, where the antenna positions will be tracked using inertial sensors of the IMU. Consequently, an appropriate array processing at the Rx can provide the DoA estimates of the incoming radio signals. We have provided measurement results in an indoor environment, where three Tx antennas and one Rx antenna attached with an IMU are used, to investigate the DoA estimation errors with virtual 3-D antenna arrays [6]. Furthermore, in [7, 8], a CRLB is used to investigate the DOA estimation performance of random 3-D antenna arrays.

3.1 Cramér-Rao Lower Bound

The CRLB provides a lower bound on the achievable estimation error accuracy of an unbiased estimator, provided that such an estimator exists [35]. The CRLB can be used to evaluate the performance of any unbiased estimator in terms of its mean square error (MSE) performance. The closer the MSE for any unbiased estimator is to the CRLB, the better the estimator is and vice versa. Furthermore, a classical or standard CRLB can be derived for deterministic unknown parameters and a stochastic or Bayesian-CRLB can be derived for random unknown parameters [36]. Similarly, if the unknown parameters are both deterministic and random, then a hybrid-CRLB can be derived for the joint processing of the unknown parameters [36, 37].

In the literature [38, 39], a CRLB is derived and different DoA estimators are proposed for the problem of source signal parameter estimation, where the superimposed signal of multiple narrowband far-field sources is received at an antenna array. In this work, in Section 3.1.1, we provide a closed form expression to compute the CRLB for a random 3-D antenna array to estimate the 2-D DoA(ϕ, θ) of an incoming radio signal, where ϕ is the azimuth and θ is the elevation as shown in Figure 3.1. A narrowband radio signal from a far-field source is received at an antenna array of N isotropic antenna elements. The derived expression for the CRLB can be used for any fixed source location to determine the 2-D DoA(ϕ, θ) estimation performance. Using Monte-Carlo simulations, where each simulation creates a random array in 3-D, we investigate the performance statistics of random 3-D antenna arrays for 2-D DoA(ϕ, θ) estimation.

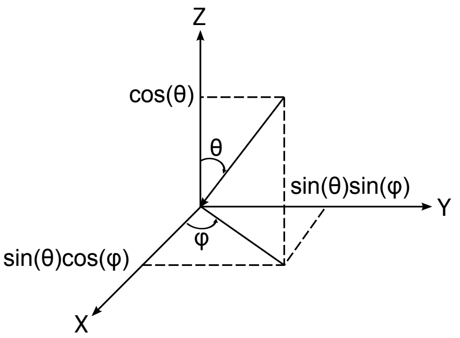

Figure 3.1: Received radio signal direction vector projected on X-, Y-, and Z-axis.

3.1.1 Arbitrary 3-D Antenna Arrays

We are using virtual antenna arrays where the IMU data is used to estimate the antenna position coordinates in 3-D. The IMU and the receive antenna can be moved freely to have a random trajectory, therefore, it is of interest to study the performance of arbitrary or random 3-D antenna arrays for DoA estimation. For the analysis, we use a simplified scenario where only a single plane wave source is considered.

Signal Model

The signal model used in the derivation of the CRLB for DoA estimation is given as

$$\mathbf{y}_r = \alpha_r \mathbf{s}(\phi, \theta) + \mathbf{e}_r, \tag{3.1}$$

where $\mathbf{y_r} \in \mathbb{C}^{N\times 1}$ is the received signal vector, α_r=ae^{jb} is the complex amplitude of the received radio signal (where a is the amplitude and b is the phase), $\mathbf{e}_r \in \mathbb{C}^{N\times 1}$ is the additive complex Gaussian noise having covariance matrix $\mathbf{R_r}$=$\sigma_r^2 \mathbf{I}_N$, and $\mathbf{s}(\phi, \theta) \in \mathbb{C}^{N\times 1}$ is the array response vector and is given by

$$\mathbf{s}(\phi, \theta) = e^{jk_0(\mathbf{x}\cos(\phi)\sin(\theta)+\mathbf{y}\sin(\phi)\sin(\theta)+\mathbf{z}\cos(\theta))}, \tag{3.2}$$

where $k_0 = \frac{2\pi}{\lambda}$ and λ is the wavelength of the radio signal. The above expressions (3.1)-(3.2) show that the received signal amplitude is assumed constant while its phase varies with the change in antenna position coordinates represented as (x, y, z). We have considered that all of the signal parameters are unknown, i.e., the signal amplitude a, its phase b, DoA in azimuth ϕ, and DoA in elevation θ. Having N i.i.d samples of the complex radio signal measured, the probability density function (pdf) of the received signal can be described as [40]

$$p(\mathbf{y}_r;\Theta) = \frac{1}{\pi^N \det(\mathbf{R_r})} e^{-[\mathbf{y}_r-\alpha_r\mathbf{s}(\phi,\theta)]^H \mathbf{R}_r^{-1}[\mathbf{y}_r-\alpha_r\mathbf{s}(\phi,\theta)]}, \tag{3.3}$$

where Θ is a vector of unknown signal parameters and is defined as

$$\Theta = [\Theta_1, \Theta_2, \Theta_3, \Theta_4]^T = [a, b, \phi, \theta]^T. \tag{3.4}$$

The variance of an unbiased estimator for each element in Θ is bounded by [35]

$$\operatorname{var}(\Theta_i) \geq [\mathbf{I}^{-1}(\Theta)]_{ii}, \tag{3.5}$$

where $i = 1, 2, 3, 4$ and $\mathbf{I}(\Theta)$ is the Fisher information matrix and is given by

$$\mathbf{I}(\Theta) =$$

$$\begin{pmatrix} -\mathbb{E}\left[\frac{\partial^2 \ln p(\mathbf{y}_r;\Theta)}{\partial a^2}\right] & -\mathbb{E}\left[\frac{\partial^2 \ln p(\mathbf{y}_r;\Theta)}{\partial a \partial b}\right] & -\mathbb{E}\left[\frac{\partial^2 \ln p(\mathbf{y}_r;\Theta)}{\partial a \partial \phi}\right] & -\mathbb{E}\left[\frac{\partial^2 \ln p(\mathbf{y}_r;\Theta)}{\partial a \partial \theta}\right] \\ -\mathbb{E}\left[\frac{\partial^2 \ln p(\mathbf{y}_r;\Theta)}{\partial b \partial a}\right] & -\mathbb{E}\left[\frac{\partial^2 \ln p(\mathbf{y}_r;\Theta)}{\partial b^2}\right] & -\mathbb{E}\left[\frac{\partial^2 \ln p(\mathbf{y}_r;\Theta)}{\partial b \partial \phi}\right] & -\mathbb{E}\left[\frac{\partial^2 \ln p(\mathbf{y}_r;\Theta)}{\partial b \partial \theta}\right] \\ -\mathbb{E}\left[\frac{\partial^2 \ln p(\mathbf{y}_r;\Theta)}{\partial \phi \partial a}\right] & -\mathbb{E}\left[\frac{\partial^2 \ln p(\mathbf{y}_r;\Theta)}{\partial \phi \partial b}\right] & -\mathbb{E}\left[\frac{\partial^2 \ln p(\mathbf{y}_r;\Theta)}{\partial \phi^2}\right] & -\mathbb{E}\left[\frac{\partial^2 \ln p(\mathbf{y}_r;\Theta)}{\partial \phi \partial \theta}\right] \\ -\mathbb{E}\left[\frac{\partial^2 \ln p(\mathbf{y}_r;\Theta)}{\partial \theta \partial a}\right] & -\mathbb{E}\left[\frac{\partial^2 \ln p(\mathbf{y}_r;\Theta)}{\partial \theta \partial b}\right] & -\mathbb{E}\left[\frac{\partial^2 \ln p(\mathbf{y}_r;\Theta)}{\partial \theta \partial \phi}\right] & -\mathbb{E}\left[\frac{\partial^2 \ln p(\mathbf{y}_r;\Theta)}{\partial \theta^2}\right] \end{pmatrix}. \tag{3.6}$$

The Fisher information matrix elements can be determined using natural logarithm of the likelihood function of the observations as

$$\ln p(\mathbf{y}_r;\Theta) = -N \ln \pi - \ln \det(\mathbf{R}_r) - \frac{1}{\sigma_r^2}[\mathbf{y}_r - \alpha_r \mathbf{s}(\phi,\theta)]^H [\mathbf{y}_r - \alpha_r \mathbf{s}(\phi,\theta)]. \tag{3.7}$$

By computing the derivatives with respect to the unknown parameters

$$\frac{\partial \ln p(\mathbf{y}_r;\Theta)}{\partial a} = \frac{1}{\sigma_r^2}[e^{jb}\mathbf{y}_r^H \mathbf{s}(\phi,\theta) + e^{-jb}\mathbf{s}^H(\phi,\theta)\mathbf{y}_r - 2a\mathbf{s}^H(\phi,\theta)\mathbf{s}(\phi,\theta)] \tag{3.8}$$

$$\frac{\partial^2 \ln p(\mathbf{y}_r;\Theta)}{\partial a^2} = \frac{2}{\sigma_r^2}\mathbf{s}^H(\phi,\theta)\mathbf{s}(\phi,\theta) \tag{3.9}$$

$$\frac{\partial^2 \ln p(\mathbf{y}_r;\Theta)}{\partial a \partial b} = \frac{1}{\sigma_r^2}[je^{jb}\mathbf{y}_r^H \mathbf{s}(\phi,\theta) - je^{-jb}\mathbf{s}^H(\phi,\theta)\mathbf{y}_r] \tag{3.10}$$

$$\begin{aligned} \frac{\partial^2 \ln p(\mathbf{y}_r;\Theta)}{\partial a \partial \phi} = {} & \frac{1}{\sigma_r^2}[e^{jb}\mathbf{y}_r^H \mathbf{s}'_\phi(\phi,\theta) + e^{-jb}[\mathbf{s}'_\phi(\phi,\theta)]^H \mathbf{y}_r \\ & -2a[\mathbf{s}'_\phi(\phi,\theta)]^H \mathbf{s}(\phi,\theta) - 2a\mathbf{s}^H(\phi,\theta)\mathbf{s}'_\phi(\phi,\theta)] \end{aligned} \tag{3.11}$$

$$\begin{aligned} \frac{\partial^2 \ln p(\mathbf{y}_r;\Theta)}{\partial a \partial \theta} = {} & \frac{1}{\sigma_r^2}[e^{jb}\mathbf{y}_r^H \mathbf{s}'_\theta(\phi,\theta) + e^{-jb}[\mathbf{s}'_\theta(\phi,\theta)]^H \mathbf{y}_r \\ & -2a[\mathbf{s}'_\theta(\phi,\theta)]^H \mathbf{s}(\phi,\theta) - 2a\mathbf{s}^H(\phi,\theta)\mathbf{s}'_\theta(\phi,\theta)], \end{aligned} \tag{3.12}$$

where

$$\mathbf{s}'_{\phi}(\phi,\theta) \triangleq \frac{\partial \mathbf{s}(\phi,\theta)}{\partial \phi} \tag{3.13}$$

$$\mathbf{s}'_{\theta}(\phi,\theta) \triangleq \frac{\partial \mathbf{s}(\phi,\theta)}{\partial \theta}. \tag{3.14}$$

By taking negative expectation with respect to the observations, the elements of the Fisher information matrix can be found as

$$-\mathbb{E}\left[\frac{\partial^2 \ln p(\mathbf{y}_r;\Theta)}{\partial a^2}\right] = \frac{2N}{\sigma_r^2} \tag{3.15}$$

$$-\mathbb{E}\left[\frac{\partial^2 \ln p(\mathbf{y}_r;\Theta)}{\partial a \partial b}\right] = 0 \tag{3.16}$$

$$-\mathbb{E}\left[\frac{\partial^2 \ln p(\mathbf{y}_r;\Theta)}{\partial a \partial \phi}\right] = 0 \tag{3.17}$$

$$-\mathbb{E}\left[\frac{\partial^2 \ln p(\mathbf{y}_r;\Theta)}{\partial a \partial \theta}\right] = 0. \tag{3.18}$$

Similarly other elements of the Fisher information matrix can be found and (3.6) can be written as

$$\mathbf{I}(\Theta) = \begin{pmatrix} \frac{2N}{\sigma_r^2} & 0 & 0 & 0 \\ 0 & \frac{2Na^2}{\sigma_r^2} & -\frac{2a^2k_0}{\sigma_r^2}\sum_{n=1}^{N} A_n & \frac{2a^2k_0}{\sigma_r^2}\sum_{n=1}^{N} B_n \\ 0 & -\frac{2a^2k_0}{\sigma_r^2}\sum_{n=1}^{N} A_n & \frac{2a^2k_0^2}{\sigma_r^2}\sum_{n=1}^{N} A_n^2 & -\frac{2a^2k_0^2}{\sigma_r^2}\sum_{n=1}^{N} A_nB_n \\ 0 & \frac{2a^2k_0}{\sigma_r^2}\sum_{n=1}^{N} B_n & -\frac{2a^2k_0^2}{\sigma_r^2}\sum_{n=1}^{N} A_nB_n & \frac{2a^2k_0^2}{\sigma_r^2}\sum_{n=1}^{N} B_n^2 \end{pmatrix}, \tag{3.19}$$

where

$$A_n = x_n \sin(\phi)\sin(\theta) - y_n \cos(\phi)\sin(\theta), \tag{3.20}$$

$$B_n = x_n \cos(\phi)\cos(\theta) + y_n \sin(\phi)\cos(\theta) - z_n \sin(\theta). \tag{3.21}$$

The matrix $\mathbf{I}(\Theta)$ is evaluated at the true values of Θ, and the diagonal values of the inverse of the Fisher information matrix provides the lower bound on the estimation error variance for each element in Θ as defined in (3.5).

To investigate the effect of random array shapes on the DoA estimation accuracy, performance statistics of arbitrary 3-D antenna arrays can be obtained using the CRLB, where Monte-Carlo simulations can be used to generate random 3-D antenna arrays and the CRLB values are obtained for different source locations in 2-D DoA (ϕ,θ).

3.1.2 Optimal Array Length

One of the fundamental limitation with the approach of making virtual antenna arrays using IMU measurements is the growing position estimation error. In unaided inertial navigation systems, having no other sensor information, the position coordinates will have growing estimation errors; the standard deviation of the estimation error values can be obtained utilizing a Kalman filter framework as discussed in Section 2.5. The estimation error covariance matrix in the EKF is useful to analyze the effect of different IMU sensor noise parameters on the growing standard deviation of the position estimation error. Also, a suitable time to make virtual antenna arrays can be determined utilizing the position estimation error standard deviation values. Furthermore, as described in Section 3.1.1, the matrix $\mathbf{I}(\Theta)$ in (3.19) can be used to calculate the CRLB for deterministic unknown radio signal parameters, where the true antenna position coordinates are given. However, if the antenna position coordinates are estimated with an estimation error associated with each antenna position, e.g., assume the true antenna position coordinates are (x_n, y_n, z_n) for the n^{th} antenna location, but the estimated antenna position coordinates are $(x_n + \Delta x_n, y_n + \Delta y_n, z_n + \Delta z_n)$. In this case, because some parameters in the signal model are known with a priori probability, a CRLB would be required by using the pdf of the antenna position errors.

3.1.3 Hybrid-CRLB

A classical or standard CRLB is used to calculate the minimum variance achievable with an unbiased estimator for deterministic unknown parameters. For random unknown parameters, the lower bound on the estimation error variance can be found using a Bayesian approach and is often referred to as the Bayesian-CRLB. The Bayesian-CRLB illustrates the minimum variance of the estimation error that can be achieved on the average using a minimum mean square error estimator. If the parameter set includes both random and deterministic unknown parameters, then the lower bound on the estimation error variance is defined as a hybrid-CRLB. More detailed descriptions can be found in [36, 37] about the use of different CRLBs. In our work, we also have both deterministic and random unknown parameters, the set of unknown parameters Θ is given as

$$\Theta = [\underbrace{a, b, \phi, \theta,}_{\Theta_{det}} \underbrace{\Delta x_1, \Delta y_1, \Delta z_1, \cdots, \Delta x_N, \Delta y_N, \Delta z_N}_{\Theta_{random}}]^T. \tag{3.22}$$

The deterministic part of the parameter set Θ_{det} consists of unknown radio signal parameters. While Θ_{random} consists of unknown parameters modeling random position errors in the estimated antenna positions. Therefore, a lower bound on the estimation error variance can be found as a hybrid-CRLB, where prior information about the random unknown parameters is known. The Fisher information matrix for the hybrid-CRLB is given as [36]

$$\mathbf{I}(\Theta)_{ij} = \mathbf{I}_1(\Theta)_{ij} + \mathbf{I}_2(\Theta)_{ij}, \tag{3.23}$$

where

$$\begin{aligned} \mathbf{I}_1(\Theta)_{ij} &= -\mathbb{E}_{\mathbf{y_r},\Theta}\left[\frac{\partial^2 \ln p(\mathbf{y_r};\Theta)}{\partial\Theta_i\partial\Theta_j}\right] && (3.24)\\ \mathbf{I}_2(\Theta)_{ij} &= -\mathbb{E}_{\Theta}\left[\frac{\partial^2 \ln p(\Theta)}{\partial\Theta_i\partial\Theta_j}\right]. && (3.25) \end{aligned}$$

The diagonal elements of matrix $\mathbf{I}_1(\Theta)$ can be determined as

$$\begin{aligned} -\mathbb{E}_{\mathbf{y_r},\Theta}\left[\frac{\partial^2 \ln p(\mathbf{y_r};\Theta)}{\partial a^2}\right] &= \mathbb{E}_{\Theta}\left[\frac{2N}{\sigma_r^2}\right] && (3.26)\\ -\mathbb{E}_{\mathbf{y_r},\Theta}\left[\frac{\partial^2 \ln p(\mathbf{y_r};\Theta)}{\partial b^2}\right] &= \mathbb{E}_{\Theta}\left[\frac{2Na^2}{\sigma_r^2}\right] && (3.27)\\ -\mathbb{E}_{\mathbf{y_r},\Theta}\left[\frac{\partial^2 \ln p(\mathbf{y_r};\Theta)}{\partial \phi^2}\right] &= \mathbb{E}_{\Theta}\left[\frac{2a^2k_0^2}{\sigma_r^2}\sum_{n=1}^{N} A_n^2\right] && (3.28)\\ -\mathbb{E}_{\mathbf{y_r},\Theta}\left[\frac{\partial^2 \ln p(\mathbf{y_r};\Theta)}{\partial \theta^2}\right] &= \mathbb{E}_{\Theta}\left[\frac{2a^2k_0^2}{\sigma_r^2}\sum_{n=1}^{N} B_n^2\right], && (3.29) \end{aligned}$$

where

$$\begin{aligned} A_n &= (x_n+\Delta x_n)\sin(\phi)\sin(\theta) - (y_n+\Delta y_n)\cos(\phi)\sin(\theta) && (3.30)\\ B_n &= (x_n+\Delta x_n)\cos(\phi)\cos(\theta) + (y_n+\Delta y_n)\sin(\phi)\cos(\theta)\\ &\quad -(z_n+\Delta z_n)\sin(\theta). && (3.31) \end{aligned}$$

The expectation with respect to the prior pdf $p(\Theta)$ of the unknown parameters can be computed as

$$\begin{aligned} \mathbb{E}_{\Theta}\left[\frac{2N}{\sigma_r^2}\right] &= \frac{2N}{\sigma_r^2} && (3.32)\\ \mathbb{E}_{\Theta}\left[\frac{2Na^2}{\sigma_r^2}\right] &= \frac{2Na^2}{\sigma_r^2} && (3.33) \end{aligned}$$

$$
\begin{aligned}
\mathbb{E}_{\Theta}\left[\frac{2a^2k_0^2}{\sigma_r^2}\sum_{n=1}^{N}A_n^2\right] &= \frac{2a^2k_0^2}{\sigma_r^2}\sum_{n=1}^{N}\mathbb{E}_{\Theta}\left[A_n^2\right] && (3.34)\\
\mathbb{E}_{\Theta}\left[\frac{2a^2k_0^2}{\sigma_r^2}\sum_{n=1}^{N}B_n^2\right] &= \frac{2a^2k_0^2}{\sigma_r^2}\sum_{n=1}^{N}\mathbb{E}_{\Theta}\left[B_n^2\right], && (3.35)
\end{aligned}
$$

where

$$\mathbb{E}_{\Theta}\left[A_n^2\right] = \int A_n^2\, p(\Theta)\mathrm{d}\Theta \tag{3.36}$$

$$\mathbb{E}_{\Theta}\left[B_n^2\right] = \int B_n^2\, p(\Theta)\mathrm{d}\Theta. \tag{3.37}$$

The prior pdf of the unknown parameters can be defined as

$$p(\Theta) = p(\Delta x_1, \Delta y_1, \Delta z_1, \cdots, \Delta x_N, \Delta y_N, \Delta z_N). \tag{3.38}$$

Assuming that the antenna position errors are independent and zero-mean Gaussian distributed, then the joint pdf $p(\Theta)$ and antenna position error covariance matrix $\mathbf{\Sigma}$ can be defined as

$$p(\Theta) = p(\Delta x_1)\, p(\Delta y_1)\, p(\Delta z_1) \cdots p(\Delta x_N)\, p(\Delta y_N)\, p(\Delta z_N), \tag{3.39}$$

$$\mathbf{\Sigma} = \begin{bmatrix}
\sigma_{x_1}^2 & 0 & 0 & & \cdots & & 0\\
0 & \sigma_{y_1}^2 & 0 & & \cdots & & 0\\
0 & 0 & \sigma_{z_1}^2 & & & & \vdots\\
\vdots & \vdots & & \ddots & & & \\
 & & & & \sigma_{x_N}^2 & 0 & 0\\
 & & & & 0 & \sigma_{y_N}^2 & 0\\
0 & 0 & \cdots & & 0 & 0 & \sigma_{z_N}^2
\end{bmatrix}. \tag{3.40}$$

Also, for $m = x, y, z$ and $i = 1, 2, \cdots, N$ representing different coordinate axes and different antenna positions, respectively, the following integrals can also be found.

$$
\begin{aligned}
\int_{\Delta m_i} \Delta m_i\, p(\Delta m_i)\, \mathrm{d}\Delta m_i &= 0 && (3.41)\\
\int_{\Delta m_i} \Delta m_i^2\, p(\Delta m_i)\, \mathrm{d}\Delta m_i &= \sigma_{m_i}^2 && (3.42)\\
\int_{\Delta m_i} p(\Delta m_i)\, \mathrm{d}\Delta m_i &= 1. && (3.43)
\end{aligned}
$$

Using the integrals in (3.41)-(3.43), the following results can be obtained

$$\begin{aligned}\mathbb{E}_\Theta\left[\frac{2a^2k_0^2}{\sigma_r^2}\sum_{n=1}^{N}A_n^2\right] &= \frac{2a^2k_0^2}{\sigma_r^2}\sum_{n=1}^{N}((x_n^2+\sigma_{x_n}^2)\sin^2\phi+(y_n^2+\sigma_{y_n}^2)\cos^2\phi\\ &\quad -2x_ny_n\sin\phi\cos\phi)\sin^2\theta \qquad (3.44)\\ \mathbb{E}_\Theta\left[\frac{2a^2k_0^2}{\sigma_r^2}\sum_{n=1}^{N}B_n^2\right] &= \frac{2a^2k_0^2}{\sigma_r^2}\sum_{n=1}^{N}((x_n^2+\sigma_{x_n}^2)\cos^2\phi+(y_n^2+\sigma_{y_n}^2)\sin^2\phi)\cos^2\theta\\ &\quad +(z_n^2+\sigma_{z_n}^2)\sin^2\theta+2x_ny_n\cos\phi\sin\phi\cos^2\theta\\ &\quad -2(y_nz_n\sin\phi\cos\theta+x_nz_n\cos\phi\cos\theta)\sin\theta \qquad (3.45)\end{aligned}$$

Using similar derivations as above, other elements of the matrix $\mathbf{I}_1(\Theta)$ can be obtained. A complete summary of results for the matrix $\mathbf{I}_1(\Theta)$ is also given in Appendix A. The following derivation provides matrix elements for $\mathbf{I}_2(\Theta)$. Firstly, taking natural logarithm of the pdf of unknown parameters

$$\begin{aligned}\ln p(\Theta) &= \ln p(\Delta x_1)+\ln p(\Delta y_1)+\ln p(\Delta z_1)+\cdots\\ &\quad +\ln p(\Delta x_N)+\ln p(\Delta y_N)+\ln p(\Delta z_N), \qquad (3.46)\end{aligned}$$

By taking the derivative of (3.46) with respect to Δx_1, the following results can be obtained

$$\frac{\partial \ln p(\Theta)}{\partial \Delta x_1}=\frac{\partial \ln p(\Delta x_1)}{\partial \Delta x_1}=-\frac{1}{\sigma_{x_1}^2}\Delta x_1, \qquad (3.47)$$

where $\ln p(\Delta x_1)$ is given as

$$\ln p(\Delta x_1)=-\frac{1}{2}\ln 2\pi\sigma_{x_1}^2-\frac{1}{2\sigma_{x_1}^2}\Delta x_1^2. \qquad (3.48)$$

Negative expectation of the second derivative results the following expression

$$-\mathbb{E}_\Theta\left[\frac{\partial^2 \ln p(\Delta x_1)}{\partial \Delta x_1^2}\right] = \frac{1}{\sigma_{x_1}^2}. \qquad (3.49)$$

For $l,m=1,2,\cdots,N$, elements of the matrix $\mathbf{I}_2(\Theta)$ can be summarized as

$$-\mathbb{E}_\Theta\left[\frac{\partial^2 \ln p(\Theta)}{\partial \Delta x_l\partial \Delta x_m}\right]=\begin{cases}\dfrac{1}{\sigma_{x_l}^2} & \text{if } l=m,\\ 0 & \text{if } l\neq m.\end{cases} \qquad (3.50)$$

$$-\mathbb{E}_\Theta\left[\frac{\partial^2 \ln p(\Theta)}{\partial \Delta y_l\partial \Delta y_m}\right]=\begin{cases}\dfrac{1}{\sigma_{y_l}^2} & \text{if } l=m,\\ 0 & \text{if } l\neq m.\end{cases} \qquad (3.51)$$

$$-\mathbb{E}_{\Theta}\left[\frac{\partial^2 \ln p(\Theta)}{\partial \Delta z_l \partial \Delta z_m}\right] = \begin{cases} \frac{1}{\sigma_{z_l}^2} & \text{if } l = m, \\ 0 & \text{if } l \neq m. \end{cases} \tag{3.52}$$

Using the results in (3.50)-(3.52), the matrix $\mathbf{I}_2(\Theta)$ can also be described as

$$\mathbf{I}_2(\Theta) = \begin{bmatrix} \mathbf{0}_{4\times 4} & \mathbf{0}_{4\times 3N} \\ \mathbf{0}_{3N\times 4} & \mathbf{\Sigma}_{3N\times 3N}^{-1} \end{bmatrix}. \tag{3.53}$$

3.2 DoA Estimation Methods

This section provides a brief overview of DoA estimation methods used in the array processing literature. DoA estimators can be categorized into three main categories.

Spectrum Based

To locate the direction of the incoming radio signal, classical DoA estimation methods make use of the angular power spectrum, by identifying the peaks in the spectrum. The most common examples of spectrum based methods is the Bartlett beamforming method [31]. Furthermore, Bartlett beamforming is an optimal method for DoA estimation for single multipath signal in white Gaussian noise. However, for two or more multipath components, high resolution or sub-space based methods perform better as compared to the classical methods for the DoA estimation.

Sub-Space Based

Several sub-space methods are available in the literature for DoA estimation. The most known technique is the MUltiple SIgnal Classification (MUSIC) method [41]. The sub-space based methods offer better resolution in DoA estimation at the expense of added complexity. One of the limiting factor in the use of sub-space methods is their sensitivity to the signal model errors [42, 43].

Maximum Likelihood Based

High-resolution methods based on the maximum likelihood (ML) principle outperform other sub-space based methods especially in low SNR conditions and for highly correlated or coherent signals; but they are also the most computationally expensive ones [31]. SAGE [32] is an ML based algorithm and it has been used by many researchers in the field of radio signal parameter estimation and radio channel modeling. The ML estimator can asymptotically achieve the CRLB using large data samples and is an asymptotically efficient estimator. Furthermore, instead of using the CRLB the ML-based estimator performance can be used to compare with other estimators in terms of accuracy and complexity; where Monte-Carlo simulations can provide MSE results for comparison purposes.

3.3 Robust DoA Estimation

Signal model errors such as incorrect antenna gain, phase, or antenna positions in the assumed signal model lead to imprecise antenna array response, which further results in degraded DoA estimation performance. Different robust DoA estimation algorithms are proposed in the literature that address the issue of signal model errors or antenna array perturbations. The following text briefly describes some robust beamforming methods available in the literature.

3.3.1 Maximum A Posteriori Estimation

In the array processing literature, the effect of signal model errors on the DoA estimation accuracy has been studied by several authors, for different estimation algorithms [42, 44, 43, 45]. The performance of high resolution DoA estimation algorithms degrades significantly if the true array response in the desired look direction is not known. One approach, that has often been employed for robust parameter estimation, uses the joint estimation of source signal parameters and signal model errors or antenna array perturbations [46, 47, 48], where, the former can be treated as deterministic unknown parameters and the latter as random unknown parameters with a priori information. This scheme can also be termed as antenna array self-calibration or auto-calibration.

In [46], the authors have introduced the use of a hybrid-CRLB which sets a lower bound on the variance of unbiased estimates of the deterministic parameters and on the mean squared errors of the random parameters. Numerical results in the paper illustrate that a conventional delay-and-sum beamformer is optimal for single source bearing and range estimates for small and independent antenna position errors, because these errors offer no structure for the estimator to exploit and the maximum a posteriori (MAP) estimation can not be applied [46, 49]. Furthermore, when more than one source is present, an approximate hybrid-CRLB was provided by assuming that the array perturbations are small [47]; and the authors also discussed the identifiability conditions for the joint estimation of antenna array parameters and source signal parameters. The results in the paper suggest that if the location of one sensor and direction to another is known and three sources disjoint in time or frequency are present, then with high SNR or large observation times array calibration can be performed to arbitrary accuracy. Similar to our work described in Section 3.1.3, in a recent article [37], the authors have provided an exact form of the hybrid-CRLB by relaxing the assumption on small (or moderately large) errors. Furthermore, the authors have claimed that if the hybrid-CRLB is tight, then the array self-calibration can be done and the least number of sources required for array self-calibration is two.

Using a Bayesian framework, following the work of [47] for small perturbations $\boldsymbol{\rho}$ around the known nominal value $\boldsymbol{\rho}_0$ having known covariance matrix $\boldsymbol{\Sigma}^{-1}$, an optimal estimator using MAP estimation can be formulated as [48, 50]

$$\mathbf{V}_{MAP}(\boldsymbol{\theta}, \boldsymbol{\rho}) = \mathbf{V}_{ML}(\boldsymbol{\theta}, \boldsymbol{\rho}) + \frac{1}{2}(\boldsymbol{\rho} - \boldsymbol{\rho}_0)^T \boldsymbol{\Sigma}^{-1}(\boldsymbol{\rho} - \boldsymbol{\rho}_0) \tag{3.54}$$

where the above cost function is minimized with respect to the signal parameters $\boldsymbol{\theta}$ and nuisance parameters $\boldsymbol{\rho}$ for optimal parameter estimation. $\mathbf{V}_{ML}(\boldsymbol{\theta}, \boldsymbol{\rho})$ is the negative log-likelihood function and $\mathbf{V}_{MAP}(\boldsymbol{\theta}, \boldsymbol{\rho})$ can be considered as a local regularization of the ML cost function. Furthermore, in [50, 51], the authors have proposed different subspace-based algorithms which are numerically simpler to implement and have equivalent asymptotic performance as can be obtained with the optimal estimator in (3.54). Simulation results in these references show that hybrid-CRLB can be asymptotically achieved for small perturbations in the array response due to antenna gain, phase, or antenna position errors.

3.3.2 Robust Capon Beamforming

The performance of the standard Capon beamformer (SCB) is very sensitive to signal model errors. However, the advantages of the SCB as compared to standard beamformers (data-independent beamformers), in terms of better resolution and interference suppression capabilities, has motivated the researchers in the field of array processing to introduce robustness in the SCB. In [52], the problem to estimate the beamforming weights and desired signal power is reformulated, such that the desired signal power is maximized by calibrating the estimated or nominal steering vector within an uncertainty ellipsoid. The proposed formulation is different from the other robust Capon beamforming approaches, because it provides a direct estimate of the desired signal power estimate as well as the beamforming filter weights.

The proposed robust Capon beamformer (RCB) is defined as [52]

$$\max_{\sigma^2,\mathbf{a}} \sigma^2 \qquad \text{subject to} \quad \mathbf{R} - \sigma^2 \mathbf{a}\mathbf{a}^H \geq 0$$
$$\text{for any } \mathbf{a} \text{ satisfying } (\mathbf{a} - \bar{\mathbf{a}})^H \mathbf{C}^{-1} (\mathbf{a} - \bar{\mathbf{a}}) \leq 1, \tag{3.55}$$

where $\mathbf{a}$ represents the steering vector, σ^2 is variance of the desired signal, and $\mathbf{R}$ is the observed signal covariance matrix. Furthermore, $\bar{\mathbf{a}}$ is the nominal or estimated steering vector, $\mathbf{C}$ is a positive definite error covariance matrix for steering vector errors. In [53], the authors have suggested that the solution to the above mentioned problem can be determined as

$$\min_{\mathbf{a}} \mathbf{a}^H \mathbf{R}^{-1} \mathbf{a} \qquad \text{subject to } (\mathbf{a} - \bar{\mathbf{a}})^H \mathbf{C}^{-1} (\mathbf{a} - \bar{\mathbf{a}}) \leq 1. \tag{3.56}$$

The derivation in [52] leads to an algorithm for calculating a diagonal loading parameter which is further used along with the the received signal covariance matrix, to compute the steering vector estimate $\hat{\mathbf{a}}$. Finally, instead of using the steering vector $\hat{\mathbf{a}}$, the estimated steering vector $\hat{\mathbf{a}}$ is used to calculate the beamforming weights $\hat{\mathbf{w}}$ by using the SCB algorithm as

$$\hat{\mathbf{w}} = \frac{\mathbf{R}^{-1}\hat{\mathbf{a}}}{\hat{\mathbf{a}}^H \mathbf{R}^{-1} \hat{\mathbf{a}}}. \tag{3.57}$$

In [52], the authors have also mentioned that the proposed methodology can be considered as another diagonal loading approach for SCB. However, depending on the steering vector uncertainty set, this approach of diagonal loading precisely calculates the loading parameter.

Signal power and DoA estimation: In one of the numerical examples shown in [52], the authors have shown that the proposed RCB and SCB have similar performance in terms of DoA estimation. However, the power of the impinging signal at the antenna array can be accurately estimated using RCB, whereas, SCB fails to estimate the signal power if the true steering vector is not known. Also, the results show that the delay-and-sum beamformer cannot be used for DoA estimation due to poor resolution capability. Also, false peaks can be observed in the angular spectrum of delay-and-sum beamformer due to higher side lobes.

Steering vector errors and uncertainty set: The proposed RCB assumes that the steering vector errors can be handled such that the nominal steering vector lies within an uncertainty set, where an uncertainty ellipsoid can be used to constrain the uncertainty set using the steering vector error covariance matrix. However, no direct method is provided to calculate the steering vector error covariance matrix based on the knowledge of antenna position estimation errors. Furthermore, in terms of DoA estimation performance, the RCB offers similar performance as compared to the SCB.

3.3.3 Robust Iterative Estimators

Assuming that the identifiability conditions as mentioned in [47] are fulfilled, iterative schemes have also been proposed in the literature to jointly estimate DoA and antenna array perturbations [54, 55, 56].

In [54], an iterative ML technique has been utilized, where the proposed algorithm consists of two steps. In the first step, using nominal values of the antenna positions, DoA estimation is performed. In the second step, using the DoA estimates from the first step, antenna positions are estimated. The algorithm iterates between the two steps until convergence is achieved. The proposed algorithm assumes that the sensor position errors are small and are close to the nominal values. In [55], the authors have suggested the use of the SAGE algorithm to jointly estimate the DoA and antenna position errors. Simulation results in the paper are given for small and large sensor position errors. The results in the paper suggest that both the ML and the SAGE algorithm have comparable performance for small antenna position errors. However, for large antenna position errors and closely spaced sources, the SAGE algorithm outperforms the ML algorithm. In [56], several existing techniques are combined together for more robust array self-calibration and improved DoA estimation as compared to the subspace-based MAP algorithms proposed in [51] and the ML algorithm proposed in [54].

The different robust DoA estimation algorithms available in the literature are mentioned to provide a brief summary of these methods and also to provide some references for the interested reader. In our work, we have not used any of these methods and this is left for the future work.

Chapter 4

Positioning Using Angular Power Spectrum

Triangulation is an approach that can be used to find the location of a mobile target when two or more angle measurements from the target to the base station are available. In [10, 11, 12], the authors have analyzed estimation of the mobile target using angle of arrival (AoA) measurements, which might be corrupted by noise, at the different base stations or receiving units. Also, different estimation methods have been utilized, such as the iterative approach for maximum likelihood estimation and closed form solutions such as least squares (LS) and weighted least squares (WLS).

In [10], the authors have suggested to use the ML estimator assuming Gaussian noise in the AoA measurements. The estimator convergence is not guaranteed and a nonlinear relationship between the measured angles and the target position is utilized. In [11], the authors have used another approach where the AoA measurements are linearly mapped to the target position in the Cartesian coordinates and noise statistics are not required in this estimation framework. This approach suggests that, using an overdetermined system where AoA measurements are available at two or more base stations, LS estimation framework can be utilized. Furthermore, in [12], the authors have extended the work of LS estimation to further improved performance using WLS; where, the weighing matrix is computed using noise variance values in the AoA measurements. However, assuming identical noise in the different AoA measurements, both the LS and the WLS estimators would be the same as the weighting matrix in the WLS would become an identity matrix.

4.1 Position Estimation Using Least Squares

Similar to the work in [11], the MS position can be estimated in a local coordinate system using DoA information available at the MS from two or more BSs. In this work, it has been assumed that the DoA estimates are obtained such that the heading information is available at the IMU and is used to align the x-axis of the IMU with the x-axis of the local coordinate system; while the tilt in the IMU with respect to the local coordinate system can be estimated using static accelerometer data measurements from the IMU. Furthermore, if no heading information is available at the MS, Section 4.2 provides a method to estimate the MS position using DoA measurements.

Assuming the Cartesian coordinates (x_i, y_i, z_i) of the different BSs in a local coordinate system are given along with the corresponding DoA(ϕ_i, θ_i) estimates available at the MS, then the following relationship is valid for the different DoA measurements

$$\frac{\sqrt{(x_i - x)^2 + (y_i - y)^2}}{(z_i - z)} = \tan\theta_i, \tag{4.1}$$

where (x_i, y_i, z_i) corresponds to the i^{th} BS position coordinates and (x, y, z) represents the MS position coordinates in the 3-D Cartesian coordinate system. Also,

$$\tan\theta_i = \frac{\sin\theta_i}{\cos\theta_i}, \tag{4.2}$$

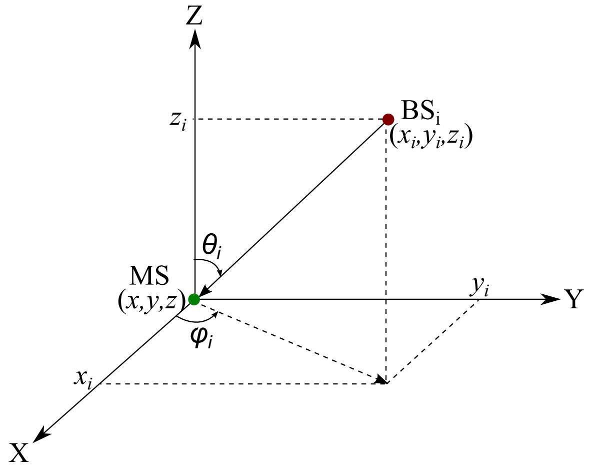

Figure 4.1: BS and MS position in the local coordinate system.

$$\sqrt{(x_i - x)^2 + (y_i - y)^2} = (x_i - x)\cos\phi_i + (y_i - y)\sin\phi_i. \tag{4.3}$$

Therefore, (4.1) can be written as

$$\frac{(x_i - x)\cos\phi_i + (y_i - y)\sin\phi_i}{(z_i - z)} = \frac{\sin\theta_i}{\cos\theta_i}, \tag{4.4}$$

or

$$\begin{aligned} & x_i \cos\phi_i \cos\theta_i + y_i \sin\phi_i \cos\theta_i - z_i \sin\theta_i = \\ & x \cos\phi_i \cos\theta_i + y \sin\phi_i \cos\theta_i - z \sin\theta_i. \end{aligned} \tag{4.5}$$

Assuming N LOS measurements from different BSs are available, then for $i = 1, 2, \cdots, N$, the above expression can be written in matrix form as

$$\underbrace{\begin{bmatrix} x_1 \cos\phi_1 \cos\theta_1 + y_1 \sin\phi_1 \cos\theta_1 - z_1 \sin\theta_1 \\ x_2 \cos\phi_2 \cos\theta_1 + y_2 \sin\phi_2 \cos\theta_2 - z_2 \sin\theta_2 \\ \vdots \\ x_N \cos\phi_n \cos\theta_N + y_N \sin\phi_N \cos\theta_N - z_N \sin\theta_N \end{bmatrix}}_{\mathbf{b}} =$$

$$\underbrace{\begin{bmatrix} \cos\phi_1 \cos\theta_1 & \sin\phi_1 \cos\theta_1 & -\sin\theta_1 \\ \cos\phi_2 \cos\theta_2 & \sin\phi_2 \cos\theta_2 & -\sin\theta_2 \\ \vdots & \vdots & \vdots \\ \cos\phi_N \cos\theta_N & \sin\phi_N \cos\theta_N & -\sin\theta_N \end{bmatrix}}_{\mathbf{A}} \underbrace{\begin{bmatrix} x \\ y \\ z \end{bmatrix}}_{\mathbf{x}}. \tag{4.6}$$

Equivalently,

$$\mathbf{b} = \mathbf{A}\mathbf{x}, \tag{4.7}$$

and the LS estimate $\hat{\mathbf{x}} = [\hat{x}, \hat{y}, \hat{z}]^T$ of the MS position can be determined as

$$\hat{\mathbf{x}} = (\mathbf{A}^T\mathbf{A})^{-1}\mathbf{A}^T\mathbf{b}. \tag{4.8}$$

4.2 Position Estimation Without Heading Information

DoA of an incoming radio signal at the MS can be estimated using a virtual antenna array [6], where the virtual antenna array is made by moving the single antenna coupled with an IMU, arbitrarily in 3D. Assume that the starting position of the moving antenna is at position (x, y, z) in a local coordinate system $(\mathrm{X}, \mathrm{Y}, \mathrm{Z})$, as shown in Figure 4.2. Also, assume that the DoA estimates are given in the MS coordinate system $(\mathrm{X_m}, \mathrm{Y_m}, \mathrm{Z_m})$. The MS is located at position (x, y, z) in the local coordinate system and at $(0, 0, 0)$ in the MS coordinate system. It is assumed that no heading information is available at the MS to align the coordinate axes of the MS coordinate system with the local coordinate system. This implies that the azimuth angle estimates at the MS can have an arbitrary offset that is added into each of the estimated azimuth angles as compared to the case where the coordinate axes of the two coordinate systems are aligned. From Figure 4.2, we can have the following relationships

$$\begin{aligned} a_{13}^2 &= b_1^2 + b_3^2 - 2b_1 b_3 \cos\psi_{13} && (4.9)\\ a_{12}^2 &= b_1^2 + b_2^2 - 2b_1 b_2 \cos\psi_{12} && (4.10)\\ a_{23}^2 &= b_2^2 + b_3^2 - 2b_2 b_3 \cos\psi_{23}. && (4.11) \end{aligned}$$

Using the known BS position coordinates (x_i, y_i, z_i) in the local coordinate system and the DoA(ϕ_i, θ_i) from the i^{th} BS to the MS in the MS coordinate system, the following results as shown in (4.12)-(4.18) can be computed and utilized in (4.9)-(4.11) to estimate the MS position $(\hat{x}, \hat{y}, \hat{z})$ in the local coordinate

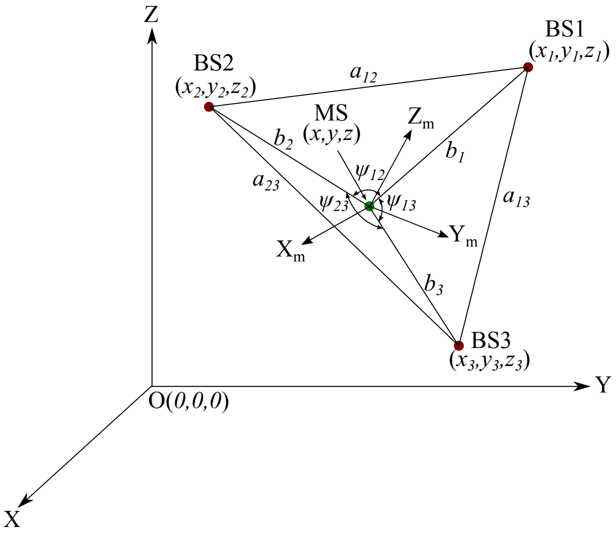

Figure 4.2: MS position estimation with three base stations whose directions from the MS and their positions in a local coordinate system are known.

system.

$$
\begin{aligned}
a_{13}^2 &= (x_1 - x_3)^2 + (y_1 - y_3)^2 + (z_1 - z_3)^2 && (4.12)\\
a_{12}^2 &= (x_1 - x_2)^2 + (y_1 - y_2)^2 + (z_1 - z_2)^2 && (4.13)\\
a_{23}^2 &= (x_2 - x_3)^2 + (y_2 - y_3)^2 + (z_2 - z_3)^2 && (4.14)\\
b_1^2 &= (x_1 - x)^2 + (y_1 - y)^2 + (z_1 - z)^2 && (4.15)\\
b_2^2 &= (x_2 - x)^2 + (y_2 - y)^2 + (z_2 - z)^2 && (4.16)\\
b_3^2 &= (x_3 - x)^2 + (y_3 - y)^2 + (z_3 - z)^2 && (4.17)\\
\psi_{13} &= \cos^{-1}(\cos\phi_1 \sin\theta_1 \cos\phi_3 \sin\theta_3 \\
&\quad + \sin\phi_1 \sin\theta_1 \sin\phi_3 \sin\theta_3 + \cos\theta_1 \cos\theta_3) && (4.18)\\
\psi_{12} &= \cos^{-1}(\cos\phi_1 \sin\theta_1 \cos\phi_2 \sin\theta_2 \\
&\quad + \sin\phi_1 \sin\theta_1 \sin\phi_2 \sin\theta_2 + \cos\theta_1 \cos\theta_2) && (4.19)\\
\psi_{23} &= \cos^{-1}(\cos\phi_2 \sin\theta_2 \cos\phi_3 \sin\theta_3 \\
&\quad + \sin\phi_2 \sin\theta_2 \sin\phi_3 \sin\theta_3 + \cos\theta_2 \cos\theta_3). && (4.20)
\end{aligned}
$$

It can also be observed from (4.9)-(4.11) that we have a set of non-linear equations. In the literature, there are multiple methods available to solve non-linear system of equations. This thesis will not describe about these methods in much detail. In our work, we have opted to use the MATLAB function 'fsolve' which utilizes non-linear least squares approach to solve multivariate non-linear equations.

Furthermore, if there are more than three BSs present whose LOS signal is being received at the MS, then the number of equations will be increased. E.g., by increasing the number of BSs by one from three to four BSs, we will have three more equations in our system of non-linear equations. To find the MS position coordinates, along-with the previously mentioned equations (4.9)-(4.11), further three equations can be described as

$$
\begin{aligned}
a_{14}^2 &= b_1^2 + b_4^2 - 2b_1 b_4 \cos\psi_{14} && (4.21)\\
a_{24}^2 &= b_2^2 + b_4^2 - 2b_2 b_4 \cos\psi_{24} && (4.22)\\
a_{34}^2 &= b_3^2 + b_4^2 - 2b_3 b_4 \cos\psi_{34}, && (4.23)
\end{aligned}
$$

where a_{14}, a_{24}, and a_{34} represent distance between BS4 and BS1, BS2, and BS3 respectively. Also, b_4 represents distance between the BS4 and the MS. Similarly, ψ_{14}, ψ_{24}, and ψ_{34} represent angle between b_1 and b_4, b_2 and b_4, and b_3 and b_4 respectively.

4.3 Positioning in Non-Line of Sight

The techniques described in the preceding sections assume that there is a direct link available between the MS and at least three base stations, such that the DoA information available at the MS can be directly used for MS position estimation. However, in practice, the direct path might be blocked between the BS and the MS due to shadowing by some large objects. In addition, multiple copies of the transmitted signal might also arrive at the MS after reflection and scattering through different objects in the environment. The problem of MS positioning in the mixed LOS/NLOS propagation has been studied extensively by different authors. It has been identified that the major source of error in the MS position estimation is caused by NLOS propagation. Different techniques have been proposed to identify and mitigate the NLOS errors in the MS position estimation. Below, we have summarized some of the related work in this area.

In [57, 58], it has been reported that the variance of the range measurements is higher in NLOS propagation as compared to the LOS scenarios; and a simple hypothesis test can be used to identify the NLOS propagation. In [59], the authors have provided algorithms to identify LOS/NLOS propagation using time history of the range measurements corrupted by noise. The paper presents the application of a binary hypothesis test on the range measurements to identify the LOS or NLOS. Noise in the measurements is assumed to follow distinct probability distribution corresponding to LOS and NLOS errors. An NLOS error mitigation technique is proposed for range measurements corrupted by NLOS errors where no a priori information is available about the statistics of the LOS and NLOS errors in the range measurements. Several authors have used the idea of calculating residual errors with estimated MS position and the known BSs positions [60, 61].

In [60] the authors have shown that if the NLOS BSs are present along with the LOS BSs, different sets of the BSs can be made to estimate the MS position. At least three BSs are, e.g., required to estimate the MS in 2D using range measurements. A residual weighting technique for MS position estimates has been used. The residues are computed as the sum of the squares of the difference between the measured ranges and the estimated ranges where the estimate ranges can be obtained using the MS position and the known BS positions. The residue would be large if the BS set has any NLOS BS as compared to the set which has only LOS BSs. The total number of BSs in the set can also be used to normalize the residues. Finally, the estimate with a lesser residue will be weighted more than the estimate with a higher residue. The proposed technique performs well in the situations where NLOS BSs are unidentifiable. The results in the paper show that best performance is achieved when only LOS BSs are used, and worst performance is observed when all the BSs are used without any residual weighting.

In [61], the authors have presented a method to identify the NLOS base stations in mixed LOS/NLOS ToA measurements. The algorithm is similar to the one that is presented in [60], however, no residual weighing has been used for MS position estimation. Instead, the authors have proposed a method to identify the NLOS BSs in the measurements and a residual test has been suggested. The NLOS base stations can be identified by measuring the statistics of the residuals. The residuals are computed for the different BS sets, where each set will have at-least three or more BSs, to estimate the MS position. A non-central chi-square distribution can be observed if any of the BS set has one or more NLOS BSs whereas a central chi-square distributions can be observed if all the sets of the BSs have LOS BSs. Simulation results are provided in the paper that show the efficacy of the proposed algorithm. An example scenario with five or more LOS base stations in a total of seven base stations shows that the algorithm attains a performance that is close to the CRLB. However, for three or four LOS base stations, the performance degrades and does not attain the CRLB. According to the authors, the overall performance of the proposed algorithm outperforms the existing state of the art methods found in the literature.

To mitigate the NLOS errors in DoA based positioning, a technique has been suggested in [62] to selectively identify and remove the NLOS base stations. By using known BS positions and the estimated MS position, the authors have proposed a technique to estimate angular errors in the DoA measurements. Simulation results in the paper show that the proposed technique performs well if the LOS errors are relatively small and there are more than enough (for position estimation in 2D, a minimum of two LOS BSs are required.) LOS BSs measurements are available. The algorithm performance with more than one NLOS base stations has not been demonstrated in the paper.

Chapter 5

Conclusions and Future Work

5.1 Conclusions

The work performed in this thesis demonstrates the use of a novel approach for DoA estimation in single antenna devices using virtual antenna arrays. Using inertial sensor data from IMU measurements, antenna location coordinates are tracked using dead reckoning. We have shown that, using a high resolution algorithm for DoA estimation, reasonably good accuracy of DoA estimation results can be achieved with low-cost IMUs for making virtual antenna arrays in single antenna devices coupled with IMUs.

We have further demonstrated that, for an unaided inertial navigation system the standard deviation of the position estimation error grows over time. Using an extended Kalman filter, we compute the estimation error covariance matrix for the different parameters in the state vector. It has been observed that, for an unaided inertial navigation system white Gaussian noise in the rate gyroscope measurements is the main source of error in the estimated position using low-cost MEMS based IMUs.

We have also derived a hybrid-CRLB to calculate the DoA estimation error variance for a single plane wave source located in the far field of the array where the antenna positions are perturbed with random antenna position errors. A closed form expression is derived to calculate the numerical value for the minimum variance that can be achieved with a minimum mean square error estimator. The results of CRLBs using known antenna locations as well as the estimated antenna locations are compared for different array lengths of the virtual antenna array. The results suggest that, after integration times of about 3-4 seconds, the two CRLBs diverge from each other and the array performance degrades significantly with the estimated antenna positions. It can also be noted that the use of hybrid-CRLB proves to be a vital tool to investigate the DoA estimation performance of antenna arrays with perturbed antenna positions.

Furthermore, theoretical results of DoA estimation performance with random 3-D antenna arrays are analyzed. Using Monte-Carlo simulations, we have shown that the performance of random 3-D antenna arrays improves significantly with increase in signal to noise ratio as well as with increased array size or number of antenna elements. The simulation results also suggest that for random antenna arrays, the array resolution for DoA estimation accuracy may vary for different source location directions and an antenna array with optimum DoA estimation accuracy for all source directions could be devised.

5.2 Future Work

In the future work, by placing transmitter antennas at known locations in an indoor environment in a similar measurement setup as described in [6], the receiver antenna location will be estimated. Both, experimental as well as theoretical evaluation of the positioning accuracy, will be investigated using the proposed setup.

Furthermore, by having channel impulse response at the receiver side for the different cellular networks, such as, GSM, WCDMA, or an LTE network, DoA estimates of the incoming signals can be obtained using the virtual antenna array. In the future work, a software radio can be utilized to obtain baseband radio signals from one or more of the commercial cellular networks, and consequently the MS position will be estimated using the virtual antenna array, where the array coordinates are tracked using a low-cost IMU.

Also, WiFi access points can be considered for MS position estimation. The positioning estimates can be obtained in the global coordinate system if the cellular network base station coordinates are known in the global coordinate system. Similarly, for the WiFi access points, the MS position can be estimated in the coordinate system where the WiFi access points are located.

References

[1] S. Godha and M. E. Cannon, "Integration of DGPS with a low cost MEMS-based inertial measurement unit (IMU) for land vehicle navigation application," in *Proc. of the 18th Int. Tech. Meeting of the Satellite Division of the Institute of Navigation (ION GNSS05)*, Long Beach, CA, 2005, pp. 333–345.

[2] N. Aboelmagd, T. B. Karmat, and J. Georgy, *Fundamentals of inertial navigation, satellite-based positioning and their Integration.* Heidelberg, Germany: Springer, 2013.

[3] M. S. Grewal, L. R. Weill, and A. P. Andrews, *Global positioning systems, inertial navigation, and integration*, 1st ed. New York: John Wiley & Sons, Inc., 2001.

[4] D. Titterton and J. L. Weston, *Strapdown inertial navigation technology*, 2nd ed. Stevenage, United Kingdom: IET, 2004.

[5] R. Zekavat and R. M. Buehrer, Eds., *Handbook of position location: Theory, practice and advances.* NJ: John Wiley & Sons, Inc., 2012.

[6] M. A. Yaqoob, F. Tufvesson, A. Mannesson, and B. Bernhardsson, "Direction of arrival estimation with arbitrary virtual antenna arrays using low cost inertial measurement units," in *2013 IEEE Int. Conf. on Communications Workshops (ICC)*, Budapest, Hungary, 2013, pp. 79–83.

[7] M. A. Yaqoob, A. Mannesson, B. Bernhardsson, N. R. Butt, and F. Tufvesson, "On the performance of random antenna arrays for direction of arrival estimation," in *2014 IEEE Int. Conf. on Communications Workshops (ICC)*, Sydney, Australia, 2014, pp. 193–199.

[8] M. A. Yaqoob, A. Mannesson, N. R. Butt, and F. Tufvesson, "Source localization using virtual antenna arrays," in *2015 Int. Conf. on Localization and GNSS (ICL-GNSS)*, Göteborg, Sweden, 2015, pp. 1–6.

[9] R. Mautz, "Indoor positioning technologies," Habilitationsschrift ETH Zürich, 2012.

[10] D. J. Torrieri, "Statistical theory of passive location systems," *IEEE Trans. Aerosp. Electron. Syst.*, vol. AES-20, no. 2, pp. 183–198, Mar. 1984.

[11] A. Pages-Zamora, J. Vidal, and D. H. Brooks, "Closed-form solution for positioning based on angle of arrival measurements," in *13th IEEE Int. Symp. on Personal, Indoor and Mobile Radio Communications*, vol. 4, Lisboa, Portugal, 2002, pp. 1522–1526.

[12] K. W. Cheung, H.-C. So, W.-K. Ma, and Y.-T. Chan, "A constrained least squares approach to mobile positioning: algorithms and optimality," *EURASIP journal on applied signal processing*, vol. 2006, pp. 1–23, Jan. 2006.

[13] "Phidgets inc. - 1044_0 - phidgetspatial precision 3/3/3 high resolution," Retrieved March 16, 2015. [Online]. Available: http://www.phidgets.com/products.php?product_id=1044

[14] J. Stewart, *Calculus: early transcendentals*, 8th ed. Boston: Cengage Learning, 2015.

[15] K. R. Britting, *Inertial Navigation Systems Analysis.* John Wiley & Sons, Inc., 1971.

[16] I. Skog and P. Händel, "Calibration of a MEMS inertial measurement unit," in *XVII IMEKO World Congress*, Rio de Janeiro, Brazil, 2006, pp. 1–6.

[17] J. Sola, "Quaternion kinematics for the error-state KF," Laboratoire d'Analyse et d'Architecture des Systemes-Centre national de la recherche scientifique (LAAS-CNRS), Toulouse, France, Tech. Rep., 2012.

[18] W. F. Phillips, C. E. Hailey, and G. A. Gebert, "Review of attitude representations used for aircraft kinematics," *Journal of Aircraft*, vol. 38, no. 4, pp. 718–737, Jul.-Aug. 2001.

[19] X. R. Li and V. P. Jilkov, "Survey of maneuvering target tracking. Part I: Dynamic models," *IEEE Trans. Aerosp. Electron. Syst.*, vol. 39, no. 4, pp. 1333–1364, Oct. 2003.

[20] R. A. Singer, "Estimating optimal tracking filter performance for manned maneuvering targets," *IEEE Trans. Aerosp. Electron. Syst.*, vol. AES-6, no. 4, pp. 473–483, Jul. 1970.

[21] N. El-Sheimy, H. Hou, and X. Niu, "Analysis and modeling of inertial sensors using Allan variance," *IEEE Trans. Instrum. Meas.*, vol. 57, no. 1, pp. 140–149, Jan. 2008.

[22] P. Petkov and T. Slavov, "Stochastic modeling of MEMS inertial sensors," *Cybernetics and information technologies*, vol. 10, no. 2, pp. 31–40, 2010.

[23] J. H. Wall and D. M. Bevly, "Characterization of inertial sensor measurements for navigation performance analysis," in *ION GNSS*, Fort Worth, TX, 2006, pp. 2678–2685.

[24] M. M. Tehrani, "Ring laser gyro data analysis with cluster sampling technique," *Proc. SPIE*, vol. 412, pp. 207–220, Sept. 1983.

[25] A. G. Quinchia, G. Falco, E. Falletti, F. Dovis, and C. Ferrer, "A comparison between different error modeling of MEMS applied to GPS/INS integrated systems," *Sensors*, vol. 13, no. 8, pp. 9549–9588, Jul. 2013.

[26] D. W. Allan, "Statistics of atomic frequency standards," *Proc. IEEE*, vol. 54, no. 2, pp. 221–230, Feb. 1966.

[27] "IEEE standard specification format guide and test procedure for single-axis interferometric fiber optic gyros," *IEEE Std 952-1997*, Dec. 2008.

[28] R. E. Kalman, "A new approach to linear filtering and prediction problems," *Transactions of the ASME - Journal of Basic Engineering*, no. 82, pp. 35–45, Mar. 1960.

[29] F. Gustafsson, *Statistical sensor fusion.* Lund, Sweden: Studentlitteratur, 2010.

[30] W. Greg and G. Bishop, "An introduction to the Kalman filter," Department of Computer Science, University of North Carolina at Chapel Hill, Chapel Hill, NC, Tech. Rep. TR 95-041, 2006.

[31] H. Krim and M. Viberg, "Two decades of array signal processing research: the parametric approach," *IEEE Signal Processing Mag.*, vol. 13, no. 4, pp. 67–94, Jul. 1996.

[32] B. H. Fleury, M. Tschudin, R. Heddergott, D. Dahlhaus, and K. Ingeman Pedersen, "Channel parameter estimation in mobile radio environments using the SAGE algorithm," *IEEE J. Sel. Areas Commun.*, vol. 17, no. 3, pp. 434–450, Mar. 1999.

[33] A. F. Molisch, *Wireless communications.* John Wiley & Sons, Inc., 2007.

[34] L. Badriasl, H. Kennedy, and A. Finn, “Effects of coordinate system rotation on two novel closed-from localization estimators using azimuth/elevation,” in *16th Int. Conf. on Information Fusion (FUSION)*, Istanbul, Turkey, 2013, pp. 1797–1804.

[35] S. M. Kay, *Fundamentals of statistical signal processing: estimation theory.* New Jersey: Prentice-Hall, Inc., 1993.

[36] H. L. Van Trees, *Optimum Array Processing, Detection Estimation, and Modulation Theory-Part IV.* New York: John Wiley & Sons, Inc., 2002.

[37] H. Messer, “The hybrid Cramer-Rao lower bound - from practice to theory,” in *4th IEEE Workshop on Sensor Array and Multichannel Processing (SAM)*, Waltham, MA, 2006, pp. 304–307.

[38] P. Stoica and A. Nehorai, “MUSIC, maximum likelihood, and Cramer-Rao bound,” *IEEE Trans. Acoust., Speech, Signal Process.*, vol. 37, no. 5, pp. 720–741, May 1989.

[39] ——, “Performance study of conditional and unconditional direction-of-arrival estimation,” *IEEE Trans. Acoust., Speech, Signal Process.*, vol. 38, no. 10, pp. 1783–1795, Oct. 1990.

[40] X. Yang, T. Long, and T. K. Sarkar, “Effect of geometry of planar antenna arrays on Cramer-Rao Bounds for DOA estimation,” in *2010 IEEE 10th Int. Conf. on Signal Processing (ICSP)*, Beijing, China, 2010, pp. 389–392.

[41] R. O. Schmidt, “Multiple emitter location and signal parameter estimation,” *IEEE Trans. Antennas Propag.*, vol. 34, no. 3, pp. 276–280, Mar. 1986.

[42] B. Friedlander, “A sensitivity analysis of the MUSIC algorithm,” *IEEE Trans. Acoust., Speech, Signal Process.*, vol. 38, no. 10, pp. 1740–1751, Oct. 1990.

[43] A. L. Swindlehurst and T. Kailath, “A performance analysis of subspace-based methods in the presence of model errors. I. The MUSIC algorithm,” *IEEE Trans. Signal Process.*, vol. 40, no. 7, pp. 1758–1774, Jul. 1992.

[44] B. Friedlander, “Sensitivity analysis of the maximum likelihood direction-finding algorithm,” *IEEE Trans. Aerosp. Electron. Syst.*, vol. 26, no. 6, pp. 953–968, Nov. 1990.

[45] A. L. Swindlehurst and T. Kailath, “A performance analysis of subspace-based methods in the presence of model error. II. Multidimensional algorithms,” *IEEE Trans. Signal Process.*, vol. 41, no. 9, pp. 2882–2890, Sept. 1993.

[46] P. M. Schultheiss and J. P. Ianniello, “Optimum range and bearing estimation with randomly perturbed arrays,” *Acoustical Society of America Journal*, vol. 68, pp. 167–173, Jul. 1980.

[47] Y. Rockah and P. M. Schultheiss, “Array shape calibration using sources in unknown locations–part I: Far-field sources,” *IEEE Trans. Acoust., Speech, Signal Process.*, vol. 35, no. 3, pp. 286–299, Mar. 1987.

[48] B. Wahlberg, B. Ottersten, and M. Viberg, “Robust signal parameter estimation in the presence of array perturbations,” in *IEEE Int. Conf. on Acoustics, Speech, and Signal Processing, ICASSP*, vol. 5, Toronto, Canada, 1991, pp. 3277–3280.

[49] Y. Rockah and P. M. Schultheiss, “Source localization with two dimensional array subject to uncertainty in sensor location,” in *IEEE Int. Conf. on Acoustics, Speech, and Signal Processing, ICASSP*, vol. 11, Tokyo, Japan, 1986, pp. 1885–1888.

[50] M. Viberg and A. L. Swindlehurst, “A Bayesian approach to auto-calibration for parametric array signal processing,” *IEEE Trans. Signal Process.*, vol. 42, no. 12, pp. 3495–3507, Dec. 1994.

[51] M. Jansson, A. L. Swindlehurst, and B. Ottersten, “Weighted subspace fitting for general array error models,” *IEEE Trans. Signal Process.*, vol. 46, no. 9, pp. 2484–2498, Sept. 1998.

[52] J. Li, P. Stoica, and Z. Wang, “On robust Capon beamforming and diagonal loading,” *IEEE Trans. Signal Process.*, vol. 51, no. 7, pp. 1702–1715, Jul. 2003.

[53] P. Stoica, Z. Wang, and J. Li, “Robust Capon beamforming,” *IEEE Signal Process. Lett.*, vol. 10, no. 6, pp. 172–175, Jun. 2003.

[54] A. J. Weiss and B. Friedlander, “Array shape calibration using sources in unknown locations-a maximum likelihood approach,” *IEEE Trans. Acoust., Speech, Signal Process.*, vol. 37, no. 12, pp. 1958–1966, Dec. 1989.

[55] P.-J. Chung and S. Wan, “Array self-calibration using SAGE algorithm,” in *2008 IEEE 5th Sensor Array and Multichannel Signal Processing Workshop (SAM)*, Darmstadt, Germany, 2008, pp. 165–169.

[56] B. P. Flanagan and K. L. Bell, “Array self-calibration with large sensor position errors,” *Signal Processing*, vol. 81, no. 10, pp. 2201–2214, Oct. 2001.

[57] L. Cong and W. Zhuang, “Nonline-of-sight error mitigation in mobile location,” *IEEE Trans. Wireless Commun.*, vol. 4, no. 2, pp. 560–573, Mar. 2005.

[58] M. P. Wylie and J. Holtzman, “The non-line of sight problem in mobile location estimation,” in *5th IEEE Int. Conf. on Universal Personal Communications*, vol. 2, Cambridge, MA, 1996, pp. 827–831.

[59] J. Borras, P. Hatrack, and N. B. Mandayam, “Decision theoretic framework for NLOS identification,” in *48th IEEE Vehicular Technology Conf. (VTC)*, vol. 2, Ottawa, Canada, 1998, pp. 1583–1587.

[60] P.-C. Chen, “A non-line-of-sight error mitigation algorithm in location estimation,” in *IEEE Wireless Communications and Networking Conf. (WCNC)*, vol. 1, New Orleans, LA, 1999, pp. 316–320.

[61] Y.-T. Chan, W.-Y. Tsui, H.-C. So, and P.-C. Ching, “Time-of-arrival based localization under NLOS conditions,” *IEEE Trans. Veh. Technol.*, vol. 55, no. 1, pp. 17–24, Jan. 2006.

[62] L. Xiong, “A selective model to suppress NLOS signals in angle-of-arrival (AOA) location estimation,” in *9th IEEE Int. Symp. on Personal, Indoor and Mobile Radio Communications*, vol. 1, Boston, MA, 1998, pp. 461–465.

Appendix A

FIM for the hybrid-CRLB

By omitting the detailed derivations, the different elements of the FIM $\mathbf{I}_1(\Theta)$ are given as

$$
\begin{aligned}
-\mathbb{E}_{\mathbf{y_r},\Theta}\left[\frac{\partial^2 \ln p(\mathbf{y_r};\Theta)}{\partial a^2}\right] &= \frac{2N}{\sigma_r^2} && \text{(A.1)}\\
-\mathbb{E}_{\mathbf{y_r},\Theta}\left[\frac{\partial^2 \ln p(\mathbf{y_r};\Theta)}{\partial b^2}\right] &= \frac{2Na^2}{\sigma_r^2} && \text{(A.2)}\\
-\mathbb{E}_{\mathbf{y_r},\Theta}\left[\frac{\partial^2 \ln p(\mathbf{y_r};\Theta)}{\partial \phi^2}\right] &= \frac{2a^2k_0^2}{\sigma_r^2}\sum_{n=1}^{N}((x_n^2+\sigma_{x_n}^2)\sin^2\phi+(y_n^2+\sigma_{y_n}^2)\cos^2\phi &&\\
&\quad -2x_ny_n\sin\phi\cos\phi)\sin^2\theta && \text{(A.3)}\\
-\mathbb{E}_{\mathbf{y_r},\Theta}\left[\frac{\partial^2 \ln p(\mathbf{y_r};\Theta)}{\partial \theta^2}\right] &= \frac{2a^2k_0^2}{\sigma_r^2}\sum_{n=1}^{N}((x_n^2+\sigma_{x_n}^2)\cos^2\phi+(y_n^2+\sigma_{y_n}^2)\sin^2\phi)\cos^2\theta &&\\
&\quad +(z_n^2+\sigma_{z_n}^2)\sin^2\theta+2x_ny_n\cos\phi\sin\phi\cos^2\theta &&\\
&\quad -2(y_nz_n\sin\phi\cos\theta+x_nz_n\cos\phi\cos\theta)\sin\theta && \text{(A.4)}\\
-\mathbb{E}_{\mathbf{y_r},\Theta}\left[\frac{\partial^2 \ln p(\mathbf{y_r};\Theta)}{\partial b\partial \phi}\right] &= -\frac{2a^2k_0}{\sigma_r^2}\sum_{n=1}^{N}A_n && \text{(A.5)}\\
-\mathbb{E}_{\mathbf{y_r},\Theta}\left[\frac{\partial^2 \ln p(\mathbf{y_r};\Theta)}{\partial b\partial \theta}\right] &= \frac{2a^2k_0}{\sigma_r^2}\sum_{n=1}^{N}B_n && \text{(A.6)}
\end{aligned}
$$

$$\begin{aligned}-\mathbb{E}_{\mathbf{y_r},\Theta}\left[\frac{\partial^2 \ln p(\mathbf{y_r};\Theta)}{\partial\phi\partial\theta}\right] &= -\frac{2a^2}{\sigma_r^2}k_0^2\sum_{n=1}^{N}(x_n^2+\sigma_{x_n}^2)\sin\phi\cos\phi\sin\theta\cos\theta \\ &\quad -(y_n^2+\sigma_{y_n}^2)\sin\phi\cos\phi\sin\theta\cos\theta \\ &\quad +x_ny_n\sin^2\phi\sin\theta\cos\theta - x_ny_n\cos^2\phi\sin\theta\cos\theta \\ &\quad -x_nz_n\sin\phi\sin^2\theta + y_nz_n\cos\phi\sin^2\theta. \qquad (A.7)\end{aligned}$$

Further elements of the matrix $\mathbf{I}_1(\Theta)$ can be evaluated as shown below for $l = 1, 2, \cdots, N$ and $m = 1, 2, \cdots, N$. Also, $C_1 = \cos\phi\sin\theta$, $C_2 = \sin\phi\sin\theta$, and $C_3 = \cos\theta$ are evaluated at the true values of ϕ and θ to calculate the FIM $\mathbf{I}_1(\Theta)$.

$$-\mathbb{E}_{\mathbf{y}_r,\Theta}\left[\frac{\partial^2 \ln p(\mathbf{y}_r;\Theta)}{\partial\Delta x_l\partial\Delta x_m}\right] = \begin{cases}\frac{2a^2}{\sigma_r^2}k_0^2C_1^2 & \text{if } l = m, \\ 0 & \text{if } l \neq m.\end{cases} \qquad (A.8)$$

$$-\mathbb{E}_{\mathbf{y}_r,\Theta}\left[\frac{\partial^2 \ln p(\mathbf{y}_r;\Theta)}{\partial\Delta y_l\partial\Delta y_m}\right] = \begin{cases}\frac{2a^2}{\sigma_r^2}k_0^2C_2^2 & \text{if } l = m, \\ 0 & \text{if } l \neq m.\end{cases} \qquad (A.9)$$

$$-\mathbb{E}_{\mathbf{y}_r,\Theta}\left[\frac{\partial^2 \ln p(\mathbf{y}_r;\Theta)}{\partial\Delta z_l\partial\Delta z_m}\right] = \begin{cases}\frac{2a^2}{\sigma_r^2}k_0^2C_3^2 & \text{if } l = m, \\ 0 & \text{if } l \neq m.\end{cases} \qquad (A.10)$$

$$-\mathbb{E}_{\mathbf{y}_r,\Theta}\left[\frac{\partial^2 \ln p(\mathbf{y}_r;\Theta)}{\partial\Delta x_l\partial\Delta y_m}\right] = \begin{cases}\frac{2a^2}{\sigma_r^2}k_0^2C_1C_2 & \text{if } l = m, \\ 0 & \text{if } l \neq m.\end{cases} \qquad (A.11)$$

$$-\mathbb{E}_{\mathbf{y}_r,\Theta}\left[\frac{\partial^2 \ln p(\mathbf{y}_r;\Theta)}{\partial\Delta x_l\partial\Delta z_m}\right] = \begin{cases}\frac{2a^2}{\sigma_r^2}k_0^2C_1C_3 & \text{if } l = m, \\ 0 & \text{if } l \neq m.\end{cases} \qquad (A.12)$$

$$-\mathbb{E}_{\mathbf{y}_r,\Theta}\left[\frac{\partial^2 \ln p(\mathbf{y}_r;\Theta)}{\partial\Delta y_l\partial\Delta z_m}\right] = \begin{cases}\frac{2a^2}{\sigma_r^2}k_0^2C_2C_3 & \text{if } l = m, \\ 0 & \text{if } l \neq m.\end{cases} \qquad (A.13)$$

Below equations can be evaluated for $n = 1, 2, \cdots, N$.

$$-\mathbb{E}_{\mathbf{y}_r,\Theta}\left[\frac{\partial^2 \ln p(\mathbf{y}_r;\Theta)}{\partial b \partial \Delta x_n}\right] = \frac{2a^2}{\sigma_r^2} k_0 C_1 \tag{A.14}$$

$$-\mathbb{E}_{\mathbf{y}_r,\Theta}\left[\frac{\partial^2 \ln p(\mathbf{y}_r;\Theta)}{\partial b \partial \Delta y_n}\right] = \frac{2a^2}{\sigma_r^2} k_0 C_2 \tag{A.15}$$

$$-\mathbb{E}_{\mathbf{y}_r,\Theta}\left[\frac{\partial^2 \ln p(\mathbf{y}_r;\Theta)}{\partial b \partial \Delta z_n}\right] = \frac{2a^2}{\sigma_r^2} k_0 C_3 \tag{A.16}$$

$$-\mathbb{E}_{\mathbf{y}_r,\Theta}\left[\frac{\partial^2 \ln p(\mathbf{y}_r;\Theta)}{\partial \phi \partial \Delta x_n}\right] = -\frac{2a^2}{\sigma_r^2} k_0^2 A_n C_1 \tag{A.17}$$

$$-\mathbb{E}_{\mathbf{y}_r,\Theta}\left[\frac{\partial^2 \ln p(\mathbf{y}_r;\Theta)}{\partial \phi \partial \Delta y_n}\right] = -\frac{2a^2}{\sigma_r^2} k_0^2 A_n C_2 \tag{A.18}$$

$$-\mathbb{E}_{\mathbf{y}_r,\Theta}\left[\frac{\partial^2 \ln p(\mathbf{y}_r;\Theta)}{\partial \phi \partial \Delta z_n}\right] = -\frac{2a^2}{\sigma_r^2} k_0^2 A_n C_3 \tag{A.19}$$

$$-\mathbb{E}_{\mathbf{y}_r,\Theta}\left[\frac{\partial^2 \ln p(\mathbf{y}_r;\Theta)}{\partial \theta \partial \Delta x_n}\right] = \frac{2a^2}{\sigma_r^2} k_0^2 B_n C_1 \tag{A.20}$$

$$-\mathbb{E}_{\mathbf{y}_r,\Theta}\left[\frac{\partial^2 \ln p(\mathbf{y}_r;\Theta)}{\partial \theta \partial \Delta y_n}\right] = \frac{2a^2}{\sigma_r^2} k_0^2 B_n C_2 \tag{A.21}$$

$$-\mathbb{E}_{\mathbf{y}_r,\Theta}\left[\frac{\partial^2 \ln p(\mathbf{y}_r;\Theta)}{\partial \theta \partial \Delta z_n}\right] = \frac{2a^2}{\sigma_r^2} k_0^2 B_n C_3. \tag{A.22}$$

All the remaining elements in $\mathbf{I}_1(\Theta)$ are found to be zero.

Part II

Included Papers

Paper I

Direction of Arrival Estimation with Arbitrary Virtual Antenna Arrays using Low Cost Inertial Measurement Units

Abstract

In this paper, we have investigated the use of virtual antenna arrays at the receiver to do single antenna direction-of-arrival estimation. The array coordinates are obtained by doing simple dead reckoning using acceleration and angular speed measurements from a low cost micro-electro-mechanical system inertial measurement unit (IMU). The proposed solution requires no extra hardware in terms of receiver chains and antenna elements. Direction-of-arrival estimation results are obtained using a high resolution SAGE algorithm. Measurement results show that the direction-of-arrival can be estimated with a reasonable accuracy in an indoor environment.

©2013 IEEE. Reprinted, with permission, from

M. A. Yaqoob, F. Tufvesson, A. Mannesson, and B. Bernhardsson,
"Direction of arrival estimation with arbitrary virtual antenna arrays using low cost inertial measurement units,"
in *2013 IEEE Int. Conf. on Communications Workshops (ICC)*, Budapest, Hungary, 2013, pp. 79-83.

1 Introduction

In radio communications, direction-of-arrival (DoA) estimation of the radio wave has been an interesting area of research as it offers several interesting benefits in terms of improved Quality-of-Service, such as, better coverage, more reliable communication, and higher data rates [1]. Furthermore, by triangulation, the DoA information can also be used for positioning or localization in a wireless cellular network.

One of the biggest challenges to get the direction-of-arrival at a mobile handheld terminal is the extra hardware, e.g., the additional antenna elements and/or receive chains that are required to form real antenna arrays or switched arrays. Due to these practical issues, as it will increase the size and weight of the device, it has not been considered to be a feasible solution to form a larger antenna array at the mobile terminal side. To solve these issues, a virtual antenna array technique can be used by moving the receiver antenna to various locations and then measuring the radio signal at those locations, one by one, assuming that the radio channel remains constant during the measurement time. In the literature, an effort is made to employ virtual antenna arrays for DoA estimation using single antenna devices as presented in [2, 3].

In [2], a virtual array was formed using a rotating arm controlled by a motor. The rotating arm provide a uniform circular array which was used to perform high resolution DoA estimation of the radio channel. Similarly, in [3], with the help of a personal computer and a motor, the authors have used a controlled movement of the antenna where the antenna was also coupled with an inertial measurement unit (IMU). From the IMU measurements of rotational speed and lateral acceleration, the radius of the circle was estimated to form a virtual uniform circular array for further processing.

In this paper, we demonstrate DoA estimation using virtual antenna arrays where the array coordinates are estimated from raw IMU measurements for arbitrary free movements carried out in 3D. The contribution of this work is that we have demonstrated a method to perform DoA estimation with single antenna devices using virtual arrays and random movements. Indoor measurements are performed to measure the radio signal synchronously with the IMU data while moving the Rx antenna, attached with an IMU, in 3D. The results obtained from these measurements are very promising and allows for further research work in the DoA based localization in wireless cellular networks, where single antenna devices are used at the receiver.

The rest of the paper is organized as follows. A brief overview of virtual antenna arrays is provided in section 2, which is followed by the description of array coordinate estimation using IMU measurements in section 3. Then, the DoA estimation algorithm (SAGE) is introduced in section 4 where it is also used to compute DoA estimates. The measurement setup is explained in section 5, and measurement results are provided in section 6. Finally, the paper is concluded in section 7.

2 Virtual Antenna Array

The virtual antenna array is based on one Rx antenna to receive the incoming radio signal and one Rx chain for down conversion and signal processing. Array coordinates corresponding to the different antenna locations are used in the DoA estimation algorithm where the phase and amplitude differences among antenna elements are used to estimate the DoA of the incoming radio wave in the azimuth (ϕ) as well as in elevation (θ). Figure 1 shows a virtual array where the radio signal is received at N different locations. The radio signal received at antenna position p_m has the following signal model [1],

$$r_{p_m}(t) = s(t) * h_{p_m}(t, \tau, \phi, \theta) + n_{p_m}(t), \tag{1}$$

where $*$ denotes convolution, and $s(t)$ is the transmitted signal and is assumed to be known. Without loss of generality, we assume $s(t) = 1$, and $n_{p_m}(t)$ is assumed to be additive white Gaussian noise measured at the m^{th} antenna position. The channel impulse response $h_{p_m}(t, \tau, \phi, \theta)$, assuming that the received signal is a sum of finite number of plane waves, is given by

$$h_{p_m}(t, \tau, \phi, \theta) = \sum_i \alpha_i(t)\delta(t - \tau_i)\delta(\phi - \phi_i)\delta(\theta - \theta_i), \tag{2}$$

where α_i, τ_i, ϕ_i and θ_i are the complex signal amplitude, delay, DoA in azimuth, and DoA in elevation of the i^{th} multi-path component (MPC), respectively.

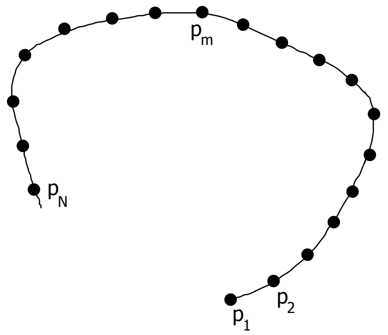

Figure 1: Virtual antenna array for N receive antenna positions.

Figure 2 shows how the incoming radio signal at different Rx antenna locations in a 3D space can be projected onto the different coordinate axes. The steering vector of the virtual array formed by the measurements at positions p_m can thus thus be expressed as

$$\mathbf{a}(\phi,\theta) = \exp(-jk(\mathbf{x}\sin(\theta)\cos(\phi) + \mathbf{y}\sin(\theta)\sin(\phi) + \mathbf{z}\cos(\theta))), \tag{3}$$

where $\mathbf{x}, \mathbf{y}$, and $\mathbf{z}$ are the position coordinate vectors of the antenna array for x-, y-, and z-axis respectively.

3 Array Coordinates

For conventional virtual antenna arrays, array coordinates are precisely controlled through controlled robotic movements and these coordinates are used for virtual array processing in DoA estimation. However, by attaching an IMU with the Rx antenna, the array coordinates for any arbitrary movement can be estimated from the IMU measurements. The IMU measurements provide raw acceleration and rotational speed in the three axes, i.e., the x-, y-, and z-axis. Local array coordinates are then obtained by computing an attitude estimate followed by a position estimate of the IMU.

3.1 Attitude Estimation

When the device is static, the only force acting upon the device is gravity. The acceleration due to gravity has to be subtracted to compute the net accelera-

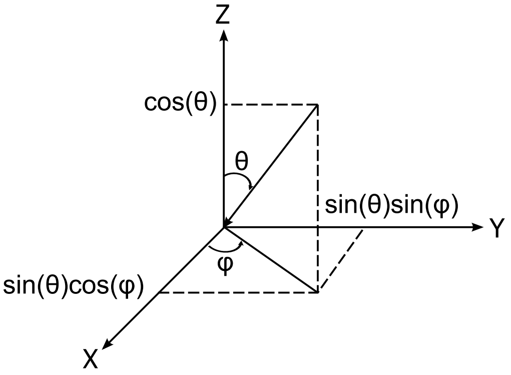

Figure 2: Received radio signal direction vector projected on X-, Y- ,and Z-axis.

tion that is experienced by the device for any movement. Also, the measured acceleration from the device is in body coordinate system (**b**), which is changing with the device movement. Position displacement of the device has to be determined in the earth coordinate system (**e**), which is fixed.

The device orientation determines the projection of gravity acceleration onto the different axes in a coordinate system. Firstly, when the device is static, the initial orientation of the device is determined. The device orientation is represented in the form of a unit quaternion [4] which is initialized as follows

$$\mathbf{q} = \begin{bmatrix} q_0 \\ q_1 \\ q_2 \\ q_3 \end{bmatrix} = \begin{bmatrix} \cos(\vartheta/2) \\ \mathbf{u} \cdot \sin(\vartheta/2) \end{bmatrix}, \tag{4}$$

where **q** is the unit quaternion, ϑ is the rotation angle between the earth coordinate system and the body coordinate system, and **u** is an orthonormal axis vector which is orthogonal to the two coordinate systems. The axis vector **u** is given by,

$$\mathbf{u} = \frac{\mathbf{b} \times \mathbf{e}}{|\mathbf{b}| \cdot |\mathbf{e}| \cdot \sin\vartheta}. \tag{5}$$

Figure 3 shows how the measurements in body coordinate system are converted to earth coordinate system through a rotation matrix defined as R^{eb} as given in (6).

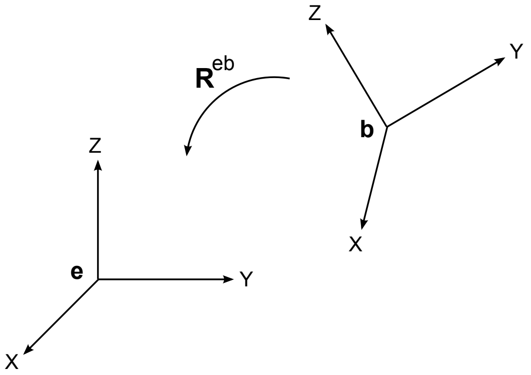

Figure 3: Body coordinate system to earth coordinate system.

$$R^{eb}(\mathbf{q}) = \begin{bmatrix} q_0^2+q_1^2-q_2^2-q_3^2 & 2q_1q_2+2q_0q_3 & 2q_1q_3-2q_0q_2 \\ 2q_1q_2-2q_0q_3 & q_0^2-q_1^2+q_2^2-q_3^2 & 2q_2q_3+2q_0q_1 \\ 2q_1q_3+2q_0q_2 & 2q_2q_3-2q_0q_1 & q_0^2-q_1^2+q_2^2+q_3^2 \end{bmatrix} \tag{6}$$

Furthermore, during any movement, the measured rotational speed from the gyroscope measurements provide the orientation update information for the IMU. The quaternions are updated using (7) which assumes that the rotation speed is constant during the sample time T_s

$$\mathbf{q}_n = \mathbf{q}_{n-1} + \frac{T_s}{2} S(\mathbf{q}_{n-1})\mathbf{w}_n, \tag{7}$$

where $\mathbf{w}$ is the 3-axis gyro measurement and $S(\mathbf{q})$ is defined as,

$$S(\mathbf{q}) = \begin{bmatrix} -q_1 & -q_2 & -q_3 \\ q_0 & -q_3 & q_2 \\ q_3 & q_0 & -q_1 \\ -q_2 & q_1 & q_0 \end{bmatrix}. \tag{8}$$

3.2 Position Estimation

Once the device acceleration in the earth coordinate system is determined, then by doing double integration of the acceleration values, we can estimate the position displacement in the x-, y-, and z-axes respectively. Figure 4 shows a block diagram for determining the array coordinates from the IMU measurements.

In Figure 4, $\mathbf{w}^b$ is the rotational speed and $\mathbf{a}^b$ is linear acceleration measurement from the IMU, $\mathbf{g}^e$ is the acceleration due to gravity defined in the earth coordinate system, and $\mathbf{p}^e$ contains the x-, y-, and z-axis position estimates in the earth coordinate system. The figure shows that gravity acceleration is subtracted from the IMU measurements to compute net acceleration due to movement which further provides the position estimates.

4 DoA Estimation

Using the local array coordinates and the received wideband radio signal at these locations, high resolution parameter estimation of the multi-path components (MPCs) can be performed using, e.g., SAGE [5]. By using an iterative method, the SAGE algorithm provide maximum likelihood estimate of the MPC parameters. For each MPC, the estimated channel parameters are complex amplitude, delay, and DoA (ϕ, θ). The number of iterations in SAGE is set to 30 and 50 MPCs are estimated.

5 Measurement Setup

Channel measurements are performed using the RUSK Lund channel sounder. The channel sounder measures the complex transfer function of the radio channel between the Tx and Rx antennas at different frequency points. In the measurements, three panel antennas are used as three different access point antennas, transmitting a channel sounding signal with center frequency at 2.44 GHz and a bandwidth of 80 MHz. The channel sounder is based on a switched array architecture and it selects one of the Tx antenna at one time to transmit the sounding signal. The panel antennas have a gain of 10 dBi in the main direction and having a beam width of 60° in the horizontal plane and 45° in the vertical plane.

To synchronize the recordings of the IMU and channel sounder, a TTL trigger signal is used to trigger the measurements at the channel sounder and the IMU measurements. A LabVIEW application is used to generate the trigger signal using the NI-9401 Digital Input/output module.

At the receiver side, a monopole antenna that has uniform antenna gain in the azimuth plane, is used to receive the incoming radio signal. The receiver antenna is also attached with a low cost inertial measurement unit, Phidget--1044. The IMU sampling rate was set to 250 Hz for the data recording. The IMU has a 3-axis accelerometer, gyroscope, and magnetometer installed on it. For our measurements, only acceleration and gyro measurements are used to estimate the local coordinates of the array. The IMU can provide acceleration values upto $\pm 2g$ and rotation speed upto $\pm 300°/s$ for z-axis and $\pm 400°/s$ for x-, and y-axis measurements.

Since low cost IMUs are prone to static bias and offset errors static bias errors in the acceleration measurements are calibrated out using the Newton's method [6], along-with cross-axis misalignment errors before applying the dead

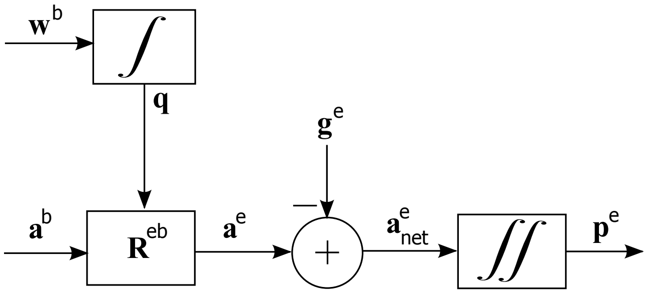

Figure 4: Position estimation from the IMU measurements.

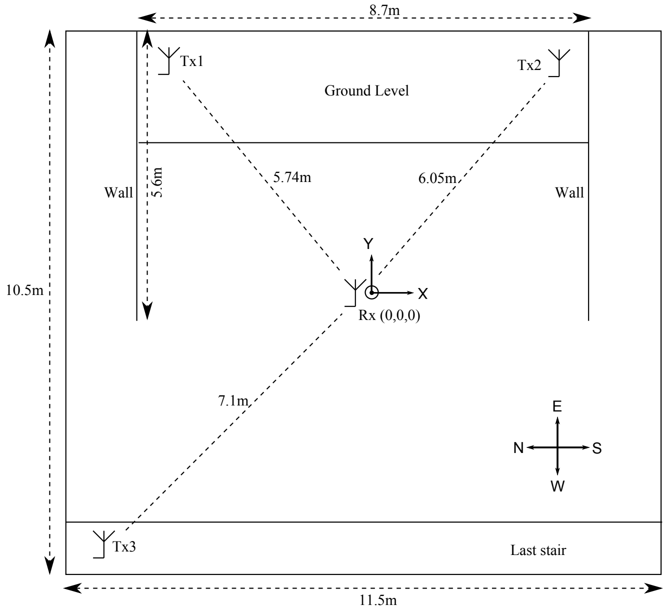

Figure 5: Room layout with antenna locations.

reckoning solution.

The measurements are performed in an indoor environment at one of the lecture theater halls in the E-building of LTH, Lund University, Sweden. The layout of the room in terms of antenna positions is shown in Figure 5. This is a rich scattering environment as many different objects can contribute to different reflection paths for the radio wave from the transmitter to the receiver. To show some details about the setup, a photo is given in Figure 6. Our main interest in this measurement campaign was to identify the line-of-sight (LOS) path from the incoming radio signal at the receiver.

Multiple free movements are carried out where the Rx antenna is moved freely in an arbitrary path. The true movement path is not tracked for these measurements, but the only validation for the suggested method is the DoA estimation results for the different LOS paths from different Tx antennas.

6 Results

The array coordinates are estimated from the IMU measurements of acceleration and angular speed. Figure 7 shows the estimated location of the Rx

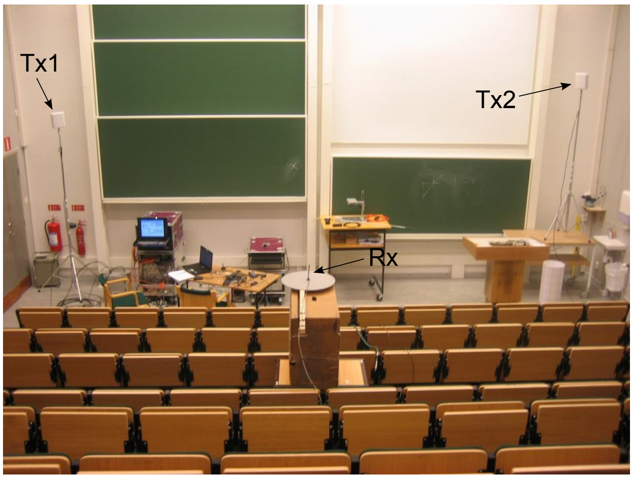

Figure 6: An indoor, rich scattering environment.

antenna at different time instants during the movement. Here we have selected one of the measurement (Mov #2) from our data set of 43 different measurements that we have recorded during the measurement activity.

As the integration error in position estimates grows unboundedly over integration time [7], initial four seconds of the movement data is used for position estimation. Furthermore, to reduce the computation time of the SAGE algorithm, every 4^{th} data sample is used from the estimated position values. The mean distance between two consecutive array positions is about $\lambda/10$ while maximum distance is observed to be around $\lambda/4$, where λ is the wavelength.

Using the estimated values of the array coordinates, DoA estimation is performed using 250 Rx antenna locations to form the virtual antenna array. As we have three independent radio links between the transmitter and receiver antennas, the SAGE estimates for these three links are determined independently.

Table 1 shows a comparison of the estimated values for DoA. The estimated DoA for the LOS path is determined by comparing the estimated delay values of the significant MPCs with each other. The significant MPCs are selected based on the criterion that it can have upto 6 dB lower power as compared to the strongest MPC. The significant MPC which has the smallest estimated delay is selected as the LOS path. Figure 8 shows the estimated DoA for different movements. Solid lines represent the true values for the DoA, while different markers on the dashed lines represent the estimated values for the DoA from different movements. Also, standard deviation values are computed for the

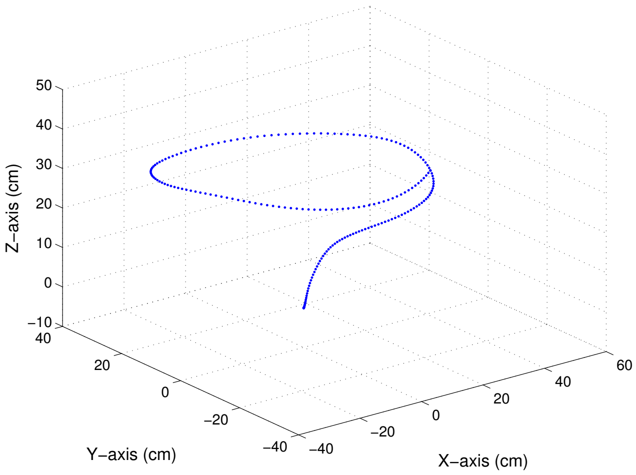

Figure 7: Array coordinates estimates using dead reckoning.

DoA estimates in different measurements. A standard deviation of about 20° is observed for the estimates. But, for Tx2, a high value of standard deviation in azimuth could be the result of 2-3 outliers in the data as shown in Figure 8.

Table 1: SAGE estimates for DoA(ϕ, θ)

Tx Ant #	True Angle (ϕ, θ)	Estimated Angle Mov #2 (ϕ, θ)	Estimated Angle St. Deviation (ϕ, θ)
1	(127°, 90°)	(120°, 89°)	(14°, 21°)
2	(47°, 80°)	(44°, 78°)	(33°, 21°)
3	(223°, 71°)	(220°, 71°)	(20°, 23°)

The estimated DoA results for Mov #2 are shown in Figs. 9 - 11, where a polar plot is used to represent the estimated angles in the azimuth plane together with their respective estimated powers. Different points in the plot represent different MPCs. The dynamic range for this plot is set to 15 dB which will discard all those MPCs whose power is 15 dB lower than the power of the strongest MPC. The distance from the center of the circle represents the associated power with each MPC. The power of the MPCs is scaled such that the strongest MPC has power of 15 dB, and is located on the outer circle in the plots.

Future work includes detailed investigation about the size and shape of the antenna array such that the DoA(ϕ, θ) estimation error could be minimized.

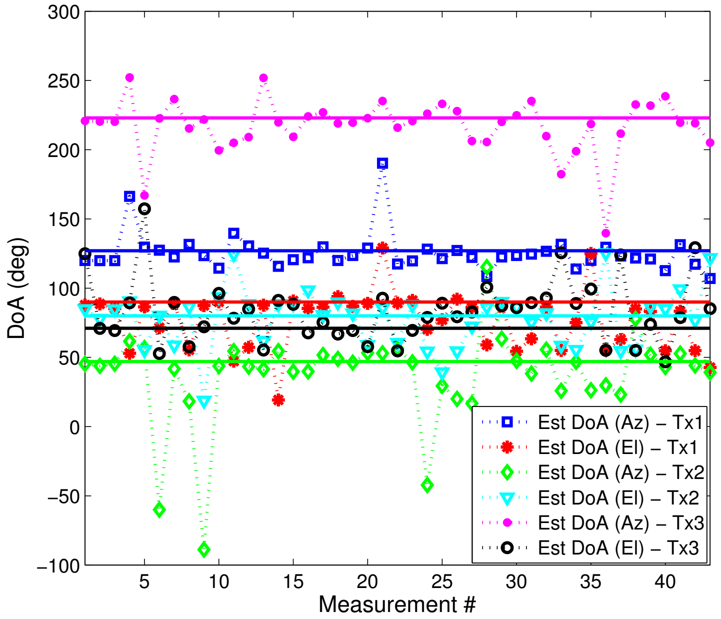

Figure 8: DoA estimates of the LOS component using SAGE algorithm for multiple movements.

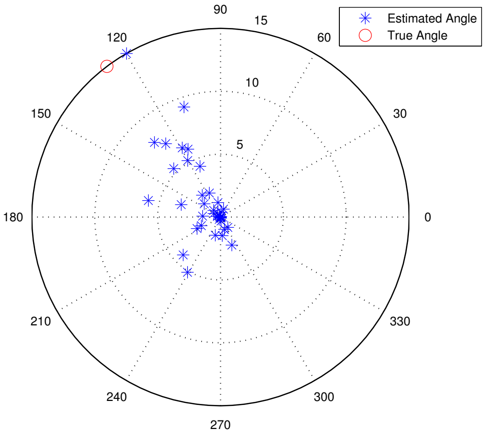

Figure 9: DoA estimates for Mov #2 using SAGE algorithm: Tx1-Rx.

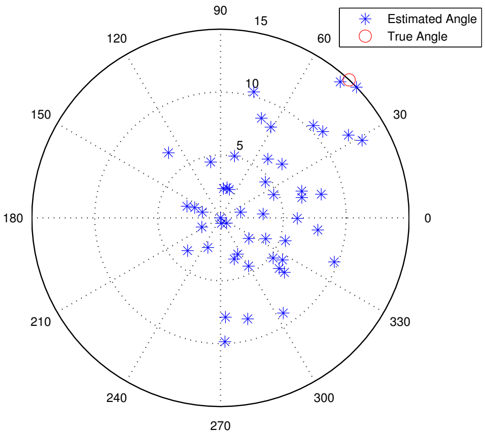

Figure 10: DoA estimates for Mov #2 using SAGE algorithm: Tx2-Rx.

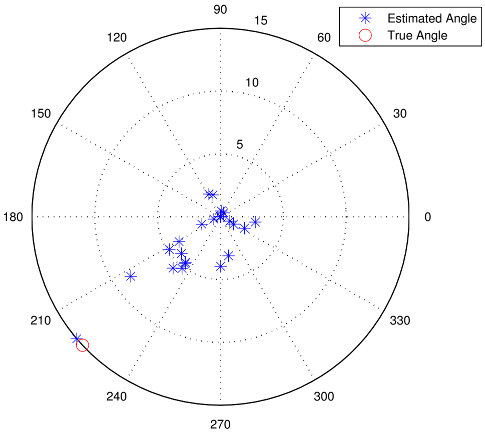

Figure 11: DoA estimates for Mov #2 using SAGE algorithm: Tx3-Rx.

Also, less complex estimation algorithms to identify the LOS path in an indoor scenario will be investigated. Furthermore, the application of this antenna array technique would be tested with commercial cellular networks, such as, the GSM network. For cellular networks, positioning/localization will be performed using DoA information of multiple base station antennas.

7 Conclusion

In this paper, we have demonstrated a method to perform DoA estimation with single antenna devices using virtual arrays and random movements. It is shown that simple dead reckoning solution can be used for position estimation with low cost MEMS based inertial measurement units for short duration of the movement (for around 3-4 seconds). The position estimates are utilized for making virtual antenna arrays with single antenna devices for directional channel estimation. It has further been shown that the direction of arrival estimation by using a high resolution SAGE algorithm provides reasonably good accuracy with random virtual antenna arrays.

Acknowledgment

This work is supported by the Excellence Center at Linköping-Lund in Information Technology (www.elliit.liu.se) and by the Lund Center for Control of Complex Engineering Systems (www.lccc.lth.se). The work was also supported by the Swedish Research Council through the project nr 621-2012-4969. The support is gratefully acknowledged.

References

[1] A. F. Molisch, *Wireless communications.* John Wiley & Sons, Inc., 2007.

[2] Y. L. C. de Jong and M. H. A. J. Herben, "High-resolution angle-of-arrival measurement of the mobile radio channel," *IEEE Trans. Antennas Propag.*, vol. 47, no. 11, pp. 1677–1687, Nov. 1999.

[3] A. Broumandan, T. Lin, A. Moghaddam, D. Lu, J. Nielsen, and G. Lachapelle, "Direction of arrival estimation of GNSS signals based on synthetic antenna array," in *ION GNSS*, Fort Worth, TX, 2007, pp. 25–28.

[4] W. F. Phillips, C. E. Hailey, and G. A. Gebert, "Review of attitude representations used for aircraft kinematics," *Journal of Aircraft*, vol. 38, no. 4, pp. 718–737, Jul.-Aug. 2001.

[5] B. H. Fleury, M. Tschudin, R. Heddergott, D. Dahlhaus, and K. Ingeman Pedersen, “Channel parameter estimation in mobile radio environments using the SAGE algorithm,” *IEEE J. Sel. Areas Commun.*, vol. 17, no. 3, pp. 434–450, Mar. 1999.

[6] I. Skog and P. Händel, “Calibration of a MEMS inertial measurement unit,” in *XVII IMEKO World Congress*, Rio de Janeiro, Brazil, 2006, pp. 1–6.

[7] J. H. Wall and D. M. Bevly, “Characterization of inertial sensor measurements for navigation performance analysis,” in *ION GNSS*, Fort Worth, TX, 2006, pp. 2678–2685.

Paper II

On the Performance of Random Antenna Arrays for Direction of Arrival Estimation

Abstract

A single antenna based virtual antenna array at the receiver can be used to find direction of different incoming radio signals impinging at the receiver. In this paper, we investigate the performance of random 3D virtual antenna arrays for DoA estimation. We have computed a Cramér-Rao Lower Bound (CRLB) for DoA estimation if the true antenna positions are not known, but these are estimated with an uncertainty. Position displacement is estimated with an extended Kalman filter (EKF) by using simulated data samples of acceleration and rotation rate which are corrupted by stochastic errors, such as, white Gaussian noise and bias drift. Furthermore, the effect of position estimation error on the DoA estimation performance is evaluated using the CRLB. The results show that the number of useful elements in the antenna array is limited, because the standard deviation of the position estimation error grows over time.

©2014 IEEE. Reprinted, with permission, from

M. A. Yaqoob, A. Mannesson, B. Bernhardsson, N. R. Butt, and F. Tufvesson, "On the performance of random antenna arrays for direction of arrival estimation," in *2014 IEEE Int. Conf. on Communications Workshops (ICC)*, Sydney, Australia, 2014, pp. 193-199.

1 Introduction

In this paper, we investigate the performance of random 3D antenna arrays for direction of arrival (DoA) estimation. The array is formed using a single antenna element that is moved to different locations to form a so-called virtual antenna array. An inertial measurement unit (IMU) can be used to track the antenna positions as shown in [1, 2], where it has also been demonstrated that DoA estimation can be performed using such virtual antenna arrays. Since the antenna position is estimated from IMU measurements which are corrupted by noise, the antenna positions are known with an uncertainty associated with each antenna location. This work will describe that using such random antenna arrays, the number of useful antenna elements in the virtual antenna array is limited; because, the standard deviation of the antenna position estimation error grows over time. For a fixed antenna array geometry and signal to noise ratio (SNR), the variance of any unbiased DoA estimator can be lower bounded by a well known bound known as Cramér-Rao Lower Bound (CRLB). Different types of antenna arrays (linear arrays, 2D, and 3D arrays) have been suggested in the literature for different applications and their performance is evaluated with the help of CRLB [3]. Similarly, Cramér-Rao Bound can be used to have a lower bound on the performance of any unbiased estimator in the presence of antenna location uncertainties [4].

The contribution of this paper is to determine the performance limits of DoA estimation using low cost IMUs to make random antenna arrays. In the first part, we have simulated a six degrees of freedom (6DoF) navigation system performance using an IMU for random movements in 3D space. Acceleration and rotation rate data samples are simulated for a random 3D movement and the simulated data is then corrupted by stochastic errors, such as, white Gaussian noise and bias drift. Position displacement is estimated in the presence of these stochastic errors using an extended Kalman filter (EKF). In the second part, the effect of position errors on the DoA estimation performance is evaluated and the results are shown in the form of CRLB.

The paper is organized as follows. Firstly, a brief overview of inertial measurement unit (IMU) is given in section 2. Section 3 describes the state space model to estimate the position displacement from the IMU measurements using the EKF. The Cramér-Rao lower bound on the DoA estimates is given in section 4. Results and discussion on the results is given in section 5. Finally, conclusion is drawn in section 6.

2 Inertial Measurement Units

Inertial measurement units (IMUs) are often used as an integral part of navigation systems. An IMU today usually has orthogonal 3-axis accelerometers and 3-axis rate gyroscopes and it can provide inertial measurements of acceleration and rotation rate which are corrupted by noise. From the IMU measurements, by performing so-called double integration of the acceleration, also known as deadreckoning, the position displacement can be estimated. However, the IMU measurements should not directly be used for longer integration times as the different noise sources present in the measurements give rise to accumulated error upon integration. This requires that the position errors should be corrected periodically after a certain amount of integration time. Alternatively, the estimated position can be used for small integration times for which the uncertainty of the estimated position remains within a specified limit.

The noise/error sources in IMU measurements can be categorized into two main categories. The first category covers fixed or deterministic error sources and the second covers random or stochastic error sources. The first type of errors, such as cross-axis misalignment, scale factor, and non-linearity errors, can be determined by calibration before using the IMU for measurements, as suggested in [5]. Stochastic error sources can be quantified by using a time domain analysis technique called Allan variance (AV) or a frequency domain analysis using power spectral decomposition (PSD) analysis [6, 7].

The Allan variance is a time domain technique originally developed by David W. Allan in 1966 to investigate the frequency stability of oscillators [8]. It has been successfully applied to model the different measurement errors in rate gyroscope and accelerometer measurements [6]. More details about Allan variance can be found in [9, 10]. In this work we will be using Allan variance analysis to quantify the stochastic errors present in the IMU measurements as shown in section 3.3.

3 Extended Kalman Filter

The Kalman filter has remained a popular choice for navigation solutions since its inception in 1960 [11]. Over time, various extensions have been proposed to the standard Kalman filter for specific applications. In this work we are using an extended Kalman filter, as the process dynamics and the measurement relationship to the process that is to be estimated is nonlinear. A brief overview of Kalman filters is given in [12].

The state vector that is to be estimated using the extended Kalman filter is given as:

$$\mathbf{x} = [\mathbf{p}, \mathbf{v}, \mathbf{a}, \mathbf{a_b}, \mathbf{q}, \mathbf{w_b}]^T, \tag{1}$$

where $\mathbf{p}$=$[p_x, p_y, p_z]^T$ is the position displacement estimated in the world coordinate system. Similarly, $\mathbf{v} \in \mathbb{R}^3$ and $\mathbf{a} \in \mathbb{R}^3$ represent the three axis estimated velocity and acceleration in the world coordinate system. $\mathbf{q}$=$[q_0, q_1, q_2, q_3]^T$ is the unit quaternion that represents the orientation of the device w.r.t. the world coordinate system. Also, $\mathbf{a_b} \in \mathbb{R}^3$ and $\mathbf{w_b} \in \mathbb{R}^3$ are used to estimate the acceleration and rotation rate bias in the acceleration and rotation rate measurements, respectively.

3.1 State Update

The acceleration state in the world coordinate system is here modeled as a first order Gauss-Markov process. Let $\tilde{\mathbf{x}}$=$[\mathbf{p}, \mathbf{v}, \mathbf{a}]^T$, then the process dynamics for the position, velocity, and acceleration states defined in the world coordinate system are given by [13]:

$$\tilde{\mathbf{x}}_{k+1} = \tilde{\mathbf{F}}\tilde{\mathbf{x}}_k + \tilde{\mathbf{G}}\nu_{a,k}, \tag{2}$$

where $\tilde{\mathbf{F}}$ and $\tilde{\mathbf{G}}$ are defined as

$$\tilde{\mathbf{F}} = \begin{bmatrix} \mathbf{I}_3 & T_s\mathbf{I}_3 & (\alpha T_s - 1 + e^{-\alpha T_s})/\alpha^2\mathbf{I}_3 \\ \mathbf{0}_3 & \mathbf{I}_3 & (1 - e^{-\alpha T_s})/\alpha\mathbf{I}_3 \\ \mathbf{0}_3 & \mathbf{0}_3 & e^{-\alpha T_s}\mathbf{I}_3 \end{bmatrix}, \tag{3}$$

$$\tilde{\mathbf{G}} = \begin{bmatrix} (1 - \alpha T_s + \alpha^2\frac{T_s^2}{2} - e^{-\alpha T_s})/\alpha^3\mathbf{I}_3 \\ (\alpha T_s - 1 + e^{-\alpha T_s})/\alpha^2\mathbf{I}_3 \\ (1 - e^{-\alpha T_s})/\alpha\mathbf{I}_3 \end{bmatrix}, \tag{4}$$

where T_s is the sample time, $\mathbf{I}_3$ is a 3×3 identity matrix, $\mathbf{0}_3$ is a 3×3 matrix of all zeros, α=$1/\tau_a$ is the inverse of the time correlation of the acceleration, and ν_a is a zero mean white Gaussian noise sequence, which drives the acceleration process, with variance $\sigma^2_{\nu_a}$.

The state dynamics for the quaternion can be expressed as [14, 15]

$$\mathbf{q}_{k+1} = e^{\frac{T_s}{2}\mathbf{S}_\mathbf{w}(\mathbf{w}_k^{true})}\mathbf{q}_k, \tag{5}$$

where $\mathbf{w}^{true}$ is the actual rotation rate.The measured rotation rate from the IMU is modeled as

$$\mathbf{w}^{meas} = \mathbf{w}^{true} + \mathbf{w_b} + \mathbf{e_w}, \tag{6}$$

where $\mathbf{w}^{meas} \in \mathbb{R}^3$ is the measured rotation rate that is the sum of actual rotation rate $\mathbf{w}^{true}$, bias in the sensor measurement $\mathbf{w}_b$, and measurement noise $\mathbf{e}_w$. The latter is modeled as zero mean white Gaussian noise with variance σ_w^2. Thus, the state dynamics for the quaternion is [14, 15]

$$\mathbf{q}_{k+1} = e^{\frac{T_s}{2}\mathbf{S}_\mathbf{w}(\mathbf{w}_k^{meas})}\mathbf{q}_k - \frac{T_s}{2}\mathbf{S}_\mathbf{q}(\mathbf{q}_k)\mathbf{w}_{b,k} - \frac{T_s}{2}\mathbf{S}_\mathbf{q}(\mathbf{q}_k)\mathbf{e}_{\mathbf{w},\mathbf{k}}, \tag{7}$$

The bias states for acceleration and rotation rates are modeled as first order Gauss-Markov processes. In discrete-time they can be modeled as

$$\begin{aligned} \mathbf{a}_{b,k+1} &= a_{d,a}\mathbf{a}_{b,k} + b_{d,a}\nu_{\mathbf{a}_b,k}, & (8) \\ \mathbf{w}_{b,k+1} &= a_{d,w}\mathbf{w}_{b,k} + b_{d,w}\nu_{\mathbf{w}_b,k}, & (9) \end{aligned}$$

where $a_{d,a} = e^{-\frac{T_s}{\tau_{a_b}}}$ and $b_{d,a} = \int_0^{T_s} e^{-\frac{t}{\tau_{a_b}}}dt$. τ_{a_b} is the time constant for the acceleration bias drift process. Furthermore, $\nu_{\mathbf{a}_b}$ and $\nu_{\mathbf{w}_b}$ represent white noise processes with variances $\sigma^2_{\nu_{\mathbf{a}_b}}$ and $\sigma^2_{\nu_{\mathbf{w}_b}}$, respectively. These white noise processes drive the bias processes and their variances are given by

$$\begin{aligned} \sigma^2_{\nu_{\mathbf{a}_b}} &= \frac{1-a^2_{d,a}}{b^2_{d,a}}\sigma^2_{a_b}, & (10) \\ \sigma^2_{\nu_{\mathbf{w}_b}} &= \frac{1-a^2_{d,w}}{b^2_{d,w}}\sigma^2_{w_b}, & (11) \end{aligned}$$

where $\sigma^2_{a_b}$ and $\sigma^2_{w_b}$ represents the variances of the accelerometer and rate gyroscope bias drift processes respectively.

3.2 Measurement Update

The acceleration state is related to the measurement through a nonlinear function as

$$\mathbf{a}_k^{meas} = \mathbf{R}_q(\mathbf{q}_k)(\mathbf{a}_k + \mathbf{g}) + \mathbf{a}_{b,k} + \mathbf{e}_{a,k}, \tag{12}$$

where $\mathbf{a}^{meas} \in \mathbb{R}^3$ is the measured acceleration in the body coordinate system, $\mathbf{R}_q(\mathbf{q})$ is the rotation matrix to transform the estimated acceleration that is in the world coordinate system to the body coordinate system, and $\mathbf{g}$ is acceleration in the world coordinate system due to gravity and is defined as $\mathbf{g}=[0, 0, 9.82]^T$. Also, the measured acceleration contains bias $\mathbf{a}_b$ as modeled in (8) and white Gaussian noise $\mathbf{e}_a$ with variance σ_a^2.

3.3 Simulation Parameters and Position Estimation

Using the Allan variance analysis, the stochastic error sources present in the IMU measurements are determined by recording static IMU data over a period of 8 hours. Figure 1 shows the measured Allan deviation (AD) curve for x-axis accelerometer and for x-axis rate gyroscope, where Allan deviation is computed as the square root of the Allan variance.

For modeling the white noise and bias drift processes used in the EKF, it is assumed that errors on the y-axis and z-axis accelerometer are similar to the x-axis accelerometer. The same is assumed for the rate gyroscope measurements. Furthermore, it is also assumed that the deterministic errors are completely removed by calibration while the effect of stochastic errors is present on the position estimates.

From the Allan deviation plot of the accelerometer and rate gyroscope data, we can identify that white Gaussian noise and bias instability are the dominant error sources for short averaging times. The standard deviation for the accelerometer white noise is determined as σ_a=VRW/$\sqrt{T_s}$, where VRW is defined as the velocity random walk parameter and its numerical value can be obtained from the Allan deviation plot when the averaging time equals to 1. The slope

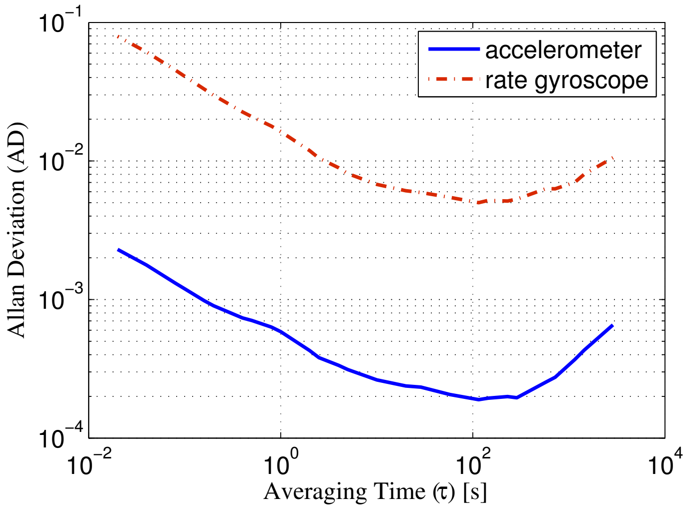

Figure 1: Measured Allan deviation (AD) plot for x-axis accelerometer and x-axis rate gyroscope data. AD is measured in m/s^2 for accelerometer data and $^\circ/s$ for rate gyroscope.

of the Allan deviation plot equals to zero when the averaging time is 115 s. This sets the time constant for the bias drift as τ_{a_b}=115 s and the standard deviation for the process noise for bias drift is found as $\sigma_{a_b}=\mathrm{AD}(\tau_{a_b})/0.664$, where $\mathrm{AD}(\tau_{a_b})$ represents the numerical value of the Allan deviation plot when the averaging time equals to τ_{a_b}. Similarly, from the Allan deviation plot of the gyroscope data, we can obtain the standard deviation of the white noise process as well as the time constant for the bias drift process and the standard deviation for the white noise that drives the bias drift process. The sampling time (T_s) is set as 20 ms and the numerical values for the noise processes are obtained as: $\sigma_a=4.15\times10^{-3}\,\mathrm{m/s}^2$, $\sigma_w=0.115\,^\circ/\mathrm{s}$, $\sigma_{a_b}=2.85\times10^{-4}\,\mathrm{m/s}^2$, and $\sigma_{w_b}=7.5\times10^{-3}\,^\circ/\mathrm{s}$. Also, τ_{w_b} is estimated as 115 s.

To simulate a random antenna array in 3D, acceleration as well as rotation rate data samples are generated using the Singer model [13]. This model is a maneuver model often used to model target maneuvering. As the antenna is moved by holding it in a hand to follow any random trajectory, the Singer model can be used to model such a movement. The Singer model states that the acceleration or rotation rate follows a first order Gauss-Markov process. In discrete time, it can be described as $\mathbf{a}_{k+1}=a_d\mathbf{a}_k + b_d\nu_{\mathbf{a}_k}$, where $a_d=e^{-\frac{T_s}{\tau_a}}$

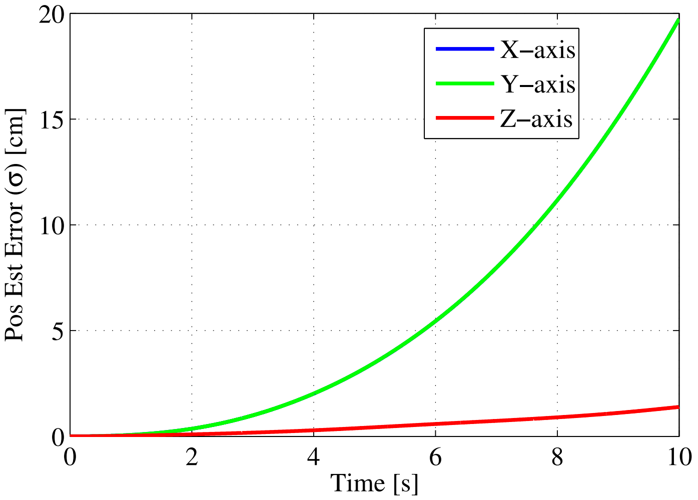

Figure 2: Position estimation error standard deviation from the EKF, x- and y-axes have similar position estimation error std. deviation vs time while z-axis has smaller std. deviation values as compared to the x- and y-axes.

and $b_d = \int_0^{T_s} e^{-\frac{t}{\tau_a}} dt$. τ_a is the maneuver time constant for the accelerometer data. Also, $\nu_{\mathbf{a_k}}$ is a white noise sequence with variance $\sigma^2_{\nu_{\mathbf{a}}} = \frac{1-a_d^2}{b_d^2}\sigma^2_{acc}$, where $\sigma^2_{acc} = \frac{a^2_{\max}}{3}(1 + 4P_{\max} - P_0)$. $a_{\max}$ is the maximum acceleration/deceleration during the maneuver, whereas, $P_{\max}$ and P_0 models the probability of having maximum acceleration/deceleration and zero acceleration during the maneuver [13]. We have used τ_a=2.5 s, $a_{\max}$=1 m/s^2, P_0=0.99, and $P_{\max}$=0.01 for the acceleration data samples. For rotation rate data, the parameter for maximum rotation rate is set to $w_{\max}$=600 °/s, while the other parameters are the same as for the acceleration. Acceleration and rotation rate data samples are then added with noise which is simulated using the values obtained from Allan deviation plots as described above. Position displacement is then estimated along-with the other states mentioned in (1) using an EKF. Figure 2 shows a typical plot for the position estimation error standard deviation that is estimated using the EKF. From Figure 2, it can be noted that the standard deviation in the estimated antenna position, as expected, grows over time. Also, the uncertainty in the x- and y-axes is similar while the z-axis has lower uncertainty as compared to the x- and y-axes. For any small tilt error (ζ) in the device orientation, the residual acceleration due to gravity on x- and y-axis would be approximated by $\sin(\zeta)$ and along z-axis it would be $\cos(\zeta)$. Using small angle approximation, $\sin(\zeta) = \zeta$ and $\cos(\zeta) = 1$. Therefore, as the gravity acceleration is along the z-axis, the residual acceleration after removing acceleration due to gravity would be larger along the x- and y-axes as compared to the z-axis.

4 Cramér Rao Lower Bound for DoA Estimation

In this section we will determine the CRLB for an antenna array where the antenna elements are defined in 3D space using Cartesian coordinates. Two different scenarios are considered to compute the CRLB. In section 4.1, the CRLB is computed when true antenna positions are known and section 4.1 provides the derivation of the CRLB when the antenna positions are estimated with an uncertainty associated with each antenna position.

4.1 CRLB with Known Antenna Positions

An incoming radio signal received from a narrowband far-field source at an antenna array comprising of N isotropic antenna elements can be defined as:

$$\mathbf{y_r} = \alpha_r \mathbf{s}(\phi,\theta) + \mathbf{e_r}, \tag{13}$$

where $\mathbf{y_r} \in \mathbb{C}^{N\times 1}$ is the received signal vector, $\alpha_r{=}ae^{jb}$ is the complex amplitude of the received radio signal (where a is the amplitude and b is the phase), $\mathbf{e}_r \in \mathbb{C}^{N\times 1}$ is the complex Gaussian white noise having covariance matrix $\mathbf{R_r}{=}\sigma_r^2\mathbf{I}$, and $\mathbf{s}(\phi,\theta)$ is the array response vector and is given by:

$$\mathbf{s}(\phi,\theta) = e^{jk(\mathbf{x}\cos(\phi)\sin(\theta)+\mathbf{y}\sin(\phi)\sin(\theta)+\mathbf{z}\cos(\theta))}, \tag{14}$$

where $\mathbf{x}$, $\mathbf{y}$, and $\mathbf{z}$ are position coordinate vectors defining the antenna elements in 3D space. Also, ϕ is the DoA of the incoming radio signal in the azimuth whereas θ is the DoA in the elevation, and $k{=}2\frac{\pi}{\lambda}$.

The probability density function of the received signal can be expressed as [3]

$$p(\mathbf{y_r};\Theta) = \frac{1}{\pi^N det(\mathbf{R_r})} e^{-(\mathbf{y_r}-\alpha_r\mathbf{s}(\phi,\theta))^H\mathbf{R_r^{-1}}(\mathbf{y_r}-\alpha_r\mathbf{s}(\phi,\theta))}, \tag{15}$$

where $\Theta{=}[a,b,\phi,\theta]$ are the unknown parameters. The Fisher information matrix $\mathbf{I}(\Theta)$ can then be found as:

$$\mathbf{I}(\Theta)_{ij} = -E_{\mathbf{y_r}}[\frac{\partial^2 \ln p(\mathbf{y_r};\Theta)}{\partial\Theta_i\partial\Theta_j}], \tag{16}$$

where $\mathbf{I}(\Theta)_{ij}$ represents the $(i,j)^{th}$ element of the 4×4 Fisher information matrix and $i,j \in [a,b,\phi,\theta]$. The expressions for the different entries in the Fisher information matrix $\mathbf{I}(\Theta)$ are determined as shown in (17)-(23):

$$-E_{\mathbf{y_r}}[\frac{\partial^2 \ln p(\mathbf{y_r};\Theta)}{\partial a^2}] = \frac{2N}{\sigma_r^2}, \tag{17}$$

$$-E_{\mathbf{y_r}}[\frac{\partial^2 \ln p(\mathbf{y_r};\Theta)}{\partial b^2}] = \frac{2Na^2}{\sigma_r^2}, \tag{18}$$

$$-E_{\mathbf{y_r}}[\frac{\partial^2 \ln p(\mathbf{y_r};\Theta)}{\partial \phi^2}] = \frac{2a^2}{\sigma_r^2}k^2\sum_{n=1}^{N} A_n^2, \tag{19}$$

$$-E_{\mathbf{y_r}}[\frac{\partial^2 \ln p(\mathbf{y_r};\Theta)}{\partial \theta^2}] = \frac{2a^2}{\sigma_r^2}k^2\sum_{n=1}^{N} B_n^2, \tag{20}$$

$$-E_{\mathbf{y_r}}[\frac{\partial^2 \ln p(\mathbf{y_r};\Theta)}{\partial b\partial\phi}] = -\frac{2a^2}{\sigma_r^2}k\sum_{n=1}^{N} A_n, \tag{21}$$

$$-E_{\mathbf{y_r}}[\frac{\partial^2 \ln p(\mathbf{y_r};\Theta)}{\partial b \partial \theta}] = \frac{2a^2}{\sigma_r^2} k \sum_{n=1}^{N} B_n, \tag{22}$$

$$-E_{\mathbf{y_r}}[\frac{\partial^2 \ln p(\mathbf{y_r};\Theta)}{\partial \phi \partial \theta}] = -\frac{2a^2}{\sigma_r^2} k^2 \sum_{n=1}^{N} A_n B_n, \tag{23}$$

where

$$A_n = (x_n \sin(\phi) - y_n \cos(\phi)) \sin(\theta), \tag{24}$$

$$B_n = (x_n \cos(\phi) + y_n \sin(\phi)) \cos(\theta) - z_n \sin(\theta). \tag{25}$$

The remaining elements of the Fisher information matrix are computed to be zero. The CRLB can then be obtained as the inverse of the Fisher information matrix.

4.2 CRLB with Estimated Antenna Positions

If the true antenna positions are not known but we have an estimate of the antenna position, e.g., for the n^{th} antenna element where n=$1, 2, \cdots, N$, let's assume (x_n, y_n, z_n) corresponds to the true antenna position represented in the 3D space and $\Delta x_n, \Delta y_n, \Delta z_n$ are the position errors along the x-, y-, and z-axis respectively. Then, the estimated position coordinates can be represented as $(x_n{+}\Delta x_n, y_n{+}\Delta y_n, z_n{+}\Delta z_n)$. Furthermore, the position errors for the n^{th} antenna element are modeled as independent zero mean white Gaussian noise processes with variances $\sigma_{x_n}^2$, $\sigma_{y_n}^2$, and $\sigma_{z_n}^2$, for the x-, y-, and z-axis, respectively. In this case, the unknown parameters would become $4 + 3N$, and are shown in (26)

$$\begin{gathered}\Theta = [a, b, \phi, \theta, \\ \Delta x_1, \Delta y_1, \Delta z_1, \Delta x_2, \Delta y_2, \Delta z_2, \cdots, \Delta x_N, \Delta y_N, \Delta z_N]\end{gathered} \tag{26}$$

Therefore, we will have deterministic unknown parameters as well as random unknown parameters. With random unknown parameters, the Fisher information matrix is defined as [4]

$$\mathbf{I}(\Theta)_{ij} = \mathbf{I}_1(\Theta)_{ij} + \mathbf{I}_2(\Theta)_{ij}, \tag{27}$$

where $i, j \in \Theta$, set of unknown parameters as shown in (26), and the two different elements of the Fisher information matrix are expressed as

$$\mathbf{I}_1(\Theta)_{ij} = -E_{\mathbf{y_r},\Theta}[\frac{\partial^2 \ln p(\mathbf{y_r};\Theta)}{\partial \Theta_i \partial \Theta_j}] \tag{28}$$

$$\mathbf{I}_2(\Theta)_{ij} = -E_{\Theta}[\frac{\partial^2 \ln p(\Theta)}{\partial \Theta_i \partial \Theta_j}]. \tag{29}$$

The elements of the Fisher information matrix in $\mathbf{I}_1(\Theta)$ can be found as shown in (30)-(51), where $l, m{=}1, 2, 3, \cdots, N$. Also, $A_1{=}\cos(\phi)\sin(\theta)$, $A_2{=}\sin(\phi)\sin(\theta)$, and $A_3{=}\cos(\theta)$.

$$-E_{\mathbf{y_r},\Theta}[\frac{\partial^2 \ln p(\mathbf{y_r};\Theta)}{\partial a^2}] = \frac{2N}{\sigma_r^2} \tag{30}$$

$$-E_{\mathbf{y_r},\Theta}[\frac{\partial^2 \ln p(\mathbf{y_r};\Theta)}{\partial b^2}] = \frac{2Na^2}{\sigma_r^2} \tag{31}$$

$$\begin{aligned}-E_{\mathbf{y_r},\Theta}[\frac{\partial^2 \ln p(\mathbf{y_r};\Theta)}{\partial \phi^2}] &= \frac{2a^2}{\sigma_r^2}k^2 \sum_{n=1}^{N} [(x_n^2 + \sigma_{x_n}^2)\sin^2(\phi) \\ &\quad +(y_n^2 + \sigma_{y_n}^2)\cos^2(\phi) - 2x_n y_n \sin(\phi)\cos(\phi)]\sin^2(\theta)\end{aligned} \tag{32}$$

$$\begin{aligned}-E_{\mathbf{y_r},\Theta}[\frac{\partial^2 \ln p(\mathbf{y_r};\Theta)}{\partial \theta^2}] &= \frac{2a^2}{\sigma_r^2}k^2 \sum_{n=1}^{N} [\{(x_n^2 + \sigma_{x_n}^2)\cos^2(\phi) \\ &\quad +(y_n^2 + \sigma_{y_n}^2)\sin^2(\phi)\}\cos^2(\theta) + (z_n^2 + \sigma_{z_n}^2)\sin^2(\theta) \\ &\quad +2(x_n y_n \cos(\phi)\sin(\phi)\cos(\theta) - y_n z_n \sin(\phi)\sin(\theta) \\ &\quad -x_n z_n \cos(\phi)\sin(\theta))\cos(\theta)]\end{aligned} \tag{33}$$

$$-E_{\mathbf{y_r},\Theta}[\frac{\partial^2 \ln p(\mathbf{y_r};\Theta)}{\partial b \partial \phi}] = -\frac{2a^2}{\sigma_r^2}k \sum_{n=1}^{N} A_n \tag{34}$$

$$-E_{\mathbf{y_r},\Theta}[\frac{\partial^2 \ln p(\mathbf{y_r};\Theta)}{\partial b \partial \theta}] = \frac{2a^2}{\sigma_r^2}k \sum_{n=1}^{N} B_n \tag{35}$$

$$\begin{aligned}-E_{\mathbf{y_r},\Theta}[\frac{\partial^2 \ln p(\mathbf{y_r};\Theta)}{\partial \phi \partial \theta}] &= -\frac{2a^2}{\sigma_r^2}k^2 \sum_{n=1}^{N} [\{(x_n^2 + \sigma_{x_n}^2) \\ &\quad -(y_n^2 + \sigma_{y_n}^2)\}\sin(\phi)\cos(\phi)\sin(\theta)\cos(\theta) \\ &\quad +x_n y_n(\sin^2(\phi) - \cos^2(\phi))\sin(\theta)\cos(\theta) \\ &\quad -z_n(x_n \sin(\phi) - y_n \cos(\phi))\sin^2(\theta)]\end{aligned} \tag{36}$$

$$-E_{\mathbf{y_r},\Theta}[\frac{\partial^2 \ln p(\mathbf{y_r};\Theta)}{\partial \Delta x_l \partial \Delta x_m}] = \begin{cases} \frac{2a^2}{\sigma_r^2}k^2 A_1^2 & \text{if } l = m, \\ 0 & \text{if } l \neq m. \end{cases} \tag{37}$$

$$-E_{\mathbf{y_r},\Theta}[\frac{\partial^2 \ln p(\mathbf{y_r};\Theta)}{\partial \Delta y_l \partial \Delta y_m}] = \begin{cases} \frac{2a^2}{\sigma_r^2} k^2 A_2^2 & \text{if } l = m, \\ 0 & \text{if } l \neq m. \end{cases} \tag{38}$$

$$-E_{\mathbf{y_r},\Theta}[\frac{\partial^2 \ln p(\mathbf{y_r};\Theta)}{\partial \Delta z_l \partial \Delta z_m}] = \begin{cases} \frac{2a^2}{\sigma_r^2} k^2 A_3^2 & \text{if } l = m, \\ 0 & \text{if } l \neq m. \end{cases} \tag{39}$$

$$-E_{\mathbf{y_r},\Theta}[\frac{\partial^2 \ln p(\mathbf{y_r};\Theta)}{\partial \Delta x_l \partial \Delta y_m}] = \begin{cases} \frac{2a^2}{\sigma_r^2} k^2 A_1 A_2 & \text{if } l = m, \\ 0 & \text{if } l \neq m. \end{cases} \tag{40}$$

$$-E_{\mathbf{y_r},\Theta}[\frac{\partial^2 \ln p(\mathbf{y_r};\Theta)}{\partial \Delta x_l \partial \Delta z_m}] = \begin{cases} \frac{2a^2}{\sigma_r^2} k^2 A_1 A_3 & \text{if } l = m, \\ 0 & \text{if } l \neq m. \end{cases} \tag{41}$$

$$-E_{\mathbf{y_r},\Theta}[\frac{\partial^2 \ln p(\mathbf{y_r};\Theta)}{\partial \Delta y_l \partial \Delta z_m}] = \begin{cases} \frac{2a^2}{\sigma_r^2} k^2 A_2 A_3 & \text{if } l = m, \\ 0 & \text{if } l \neq m. \end{cases} \tag{42}$$

$$-E_{\mathbf{y_r},\Theta}[\frac{\partial^2 \ln p(\mathbf{y_r};\Theta)}{\partial b \partial \Delta x_n}] = \frac{2a^2}{\sigma_r^2} k A_1 \tag{43}$$

$$-E_{\mathbf{y_r},\Theta}[\frac{\partial^2 \ln p(\mathbf{y_r};\Theta)}{\partial b \partial \Delta y_n}] = \frac{2a^2}{\sigma_r^2} k A_2 \tag{44}$$

$$-E_{\mathbf{y_r},\Theta}[\frac{\partial^2 \ln p(\mathbf{y_r};\Theta)}{\partial b \partial \Delta z_n}] = \frac{2a^2}{\sigma_r^2} k A_3 \tag{45}$$

$$-E_{\mathbf{y_r},\Theta}[\frac{\partial^2 \ln p(\mathbf{y_r};\Theta)}{\partial \phi \partial \Delta x_n}] = -\frac{2a^2}{\sigma_r^2} k^2 A_1 A_n \tag{46}$$

$$-E_{\mathbf{y_r},\Theta}[\frac{\partial^2 \ln p(\mathbf{y_r};\Theta)}{\partial \phi \partial \Delta y_n}] = -\frac{2a^2}{\sigma_r^2} k^2 A_2 A_n \tag{47}$$

$$-E_{\mathbf{y_r},\Theta}[\frac{\partial^2 \ln p(\mathbf{y_r};\Theta)}{\partial \phi \partial \Delta z_n}] = -\frac{2a^2}{\sigma_r^2} k^2 A_3 A_n \tag{48}$$

$$-E_{\mathbf{y_r},\Theta}[\frac{\partial^2 \ln p(\mathbf{y_r};\Theta)}{\partial \theta \partial \Delta x_n}] = \frac{2a^2}{\sigma_r^2} k^2 A_1 B_n \tag{49}$$

$$-E_{\mathbf{y_r},\Theta}[\frac{\partial^2 \ln p(\mathbf{y_r};\Theta)}{\partial \theta \partial \Delta y_n}] = \frac{2a^2}{\sigma_r^2} k^2 A_2 B_n \tag{50}$$

$$-E_{\mathbf{y_r},\Theta}[\frac{\partial^2 \ln p(\mathbf{y_r};\Theta)}{\partial \theta \partial \Delta z_n}] = \frac{2a^2}{\sigma_r^2} k^2 A_3 B_n \tag{51}$$

The remaining elements of $\mathbf{I}_1(\Theta)$ are found to be zero. The other part of the Fisher information matrix, i.e., $\mathbf{I}_2(\Theta)$ can be found as shown in (52), where the position errors are modeled as independent zero mean white Gaussian noise processes at each antenna location and also for the x-, y-, and z-axes as well.

$$\mathbf{I}_2(\Theta) = \begin{bmatrix} 0_{4\times 4} & 0_{4\times 3N} \\ 0_{3N\times 4} & \Sigma_{3N\times 3N}^{-1} \end{bmatrix} \tag{52}$$

where $0_{4\times 4}$ is a 4×4 matrix of all zeros for the deterministic unknown parameters and $\Sigma_{3N\times 3N}$ is a diagonal matrix representing the variance of the position errors along its diagonal and is defined as $\Sigma_{3N\times 3N} = diag(\sigma_{x_1}^2, \sigma_{y_1}^2, \sigma_{z_1}^2, \cdots, \sigma_{x_N}^2, \sigma_{y_N}^2, \sigma_{z_N}^2)$, where the first three diagonal elements represent the position error variance of the first antenna element and the last three elements define the position error variance of the last antenna element, for x-, y-, and z-axis respectively.

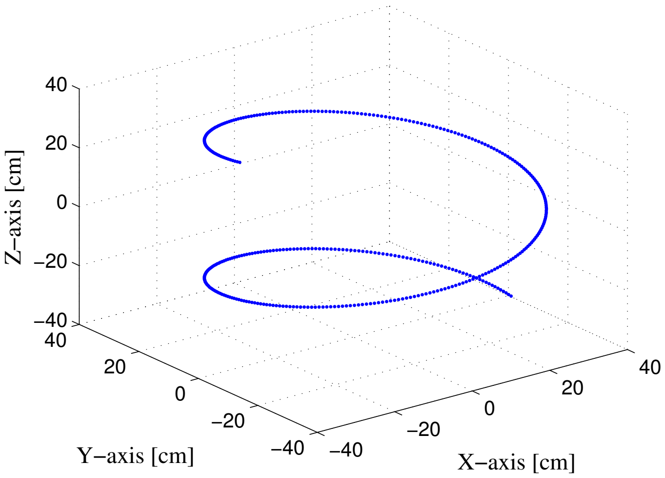

Figure 3: An antenna array in 3D where different points in the plot represent the antenna positions. The array is used to analyze the performance of DoA estimation with known and estimated antenna positions through CRLB plots.

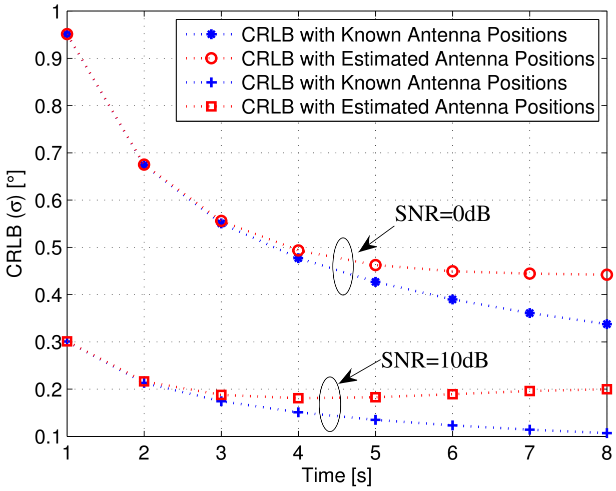

Figure 4: CRLB for estimating (ϕ) for a given DoA($30°$, $30°$) using the antenna array shown in Figure 3. 1 s corresponds to 50 antenna elements array obtained from IMU data samples where the IMU is sampled at a rate of 20 ms.

5 Results and Discussion

In this section, using the position estimation error standard deviation values as shown in Figure 2, we have computed two CRLB plots for the two cases mentioned in section 4, i.e., when the antenna positions are known and when the antenna positions are estimated with an uncertainty. Radio signal centre frequency is set as f_c=2.4 GHz, and signal to noise ratio at the receiving antenna elements is assumed to be 0 dB. An antenna array geometry as shown in Figure 3 is defined in 3D where the origin is at the center of gravity of the array. The CRLB plots are then obtained and are shown in Figure 4 for a given DoA$(30°, 30°)$. In the CRLB plots, x-axis represents the number of antenna elements that span the antenna array for different movement times. The sampling time is used as 20 ms to simulate the IMU as well as radio samples. The given sampling rate provides 50 antenna positions after 1 second of the movement time and so on. In order to analyze the effect of growing standard deviation of the position estimation error onto the DoA estimation accuracy, different movement times are used such that each movement covers the same trajectory but with different time by changing the speed of the movement. Thus, the number of antenna elements that span the whole trajectory are varied but the array shape is kept the same. The CRLB values are then calculated corresponding to different movement times. From the plot when antenna positions are known it can be seen that as time increases, i.e., more antenna elements are used to represent the antenna array, then the CRLB decreases because with the increase of antenna elements the SNR is improved and the array resolution is enhanced as well. Thus, the DoA estimation could be performed with better accuracy. However, if the antenna positions are not known and are estimated with an uncertainty whose standard deviation is also growing, then, in this case the CRLB first decreases with increasing antennas. But, as time goes more than 3 second, we can observe that the CRLB plot starts to deviate from the plot where the antenna positions are known and the difference between the two CRLB plots grows over time. The growing standard deviation of the antenna position estimation error plays a significant role in limiting the performance of the DoA estimation as we observe for the case when antenna positions are known. The standard deviation of the position estimation error is relatively small in the beginning or for short integration times, but the standard deviation grows over time and we can observe that the gap between the two CRLB plots also grows over time as well. Therefore, it is found that an optimal time limit should be determined in order to make the virtual antenna array where the antenna positions are obtained with relatively small position estimation errors. For the given standard deviation of the antenna position estimation errors, as shown in Figure 2, the optimal time in terms of DoA estimation performance is found to be approximately 3-4 seconds, and after this time limit we can see significant difference of the DoA estimation accuracy between the two CRLB plots. Similar results can be seen when the SNR is set as 10 dB.

As described above, similar analysis can be performed to estimate the performance of any random 3D antenna array if the antenna positions are known with an uncertainty. Figure 5 shows an example of a random 3D antenna array and in Figure 6 CRLB plots are shown. The two examples of 3D antenna arrays illustrate the usefulness of the given framework to compute the CRLB with known and estimated antenna positions. More detailed analysis of the results in terms of DoA estimation accuracy w.r.t. the different array shapes will be treated in our future work.

6 Conclusion

In this paper, we have shown that the performance of virtual antenna arrays using inertial measurement units is limited by the growing standard deviation of the antenna position estimation errors. The effect of stochastic error sources, such as, white Gaussian noise and bias drift in the IMU measurements is investigated using EKF, which shows that the standard deviation of the position estimation error grows over time. Furthermore, we have computed Cramér-Rao

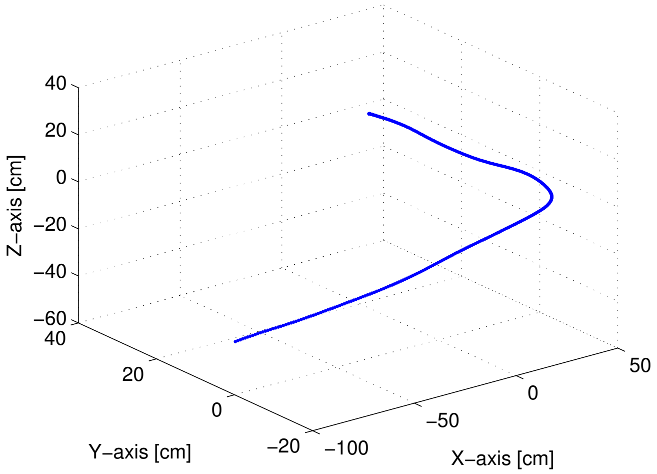

Figure 5: Example of a random 3D antenna array.

lower bound (CRLB) if the antenna positions are known and if the antenna positions are estimated with an uncertainty. Using these two CRLB values, it has been shown that after a specific integration time, the increase in the standard deviation of the position estimation error plays a significant role and the increase in the number of antenna elements does not provide significant improvement in the performance of DoA estimation. For a low cost MEMS based IMU making a typical 3D movement, the optimal integration/movement time in terms of DoA estimation performance has been found to be approximately 3-4 seconds.

Acknowledgment

This work is supported by the Excellence Center at Linköping-Lund in Information Technology (www.elliit.liu.se) and by the Lund Center for Control of Complex Engineering Systems (www.lccc.lth.se) as well as the Swedish Research Council. The support is gratefully acknowledged.

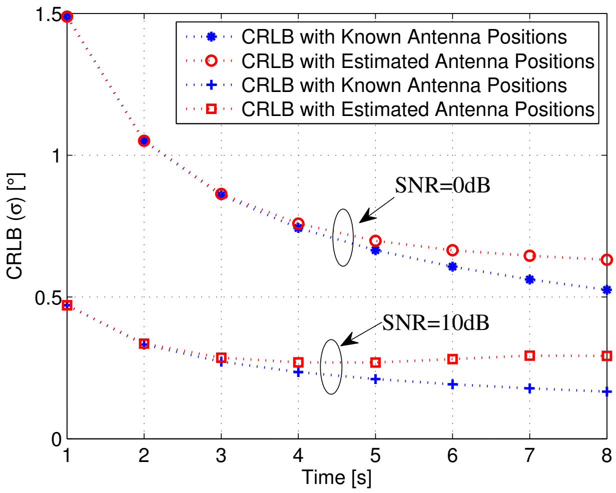

Figure 6: CRLB for estimating (ϕ) for a given DoA(30°, 30°) using the antenna array shown in Figure 5.

References

[1] M. A. Yaqoob, F. Tufvesson, A. Mannesson, and B. Bernhardsson, "Direction of arrival estimation with arbitrary virtual antenna arrays using low cost inertial measurement units," in *2013 IEEE Int. Conf. on Communications Workshops (ICC)*, Budapest, Hungary, 2013, pp. 79–83.

[2] A. Broumandan, T. Lin, A. Moghaddam, D. Lu, J. Nielsen, and G. Lachapelle, "Direction of arrival estimation of GNSS signals based on synthetic antenna array," in *ION GNSS*, Fort Worth, TX, 2007, pp. 25–28.

[3] X. Yang, T. Long, and T. K. Sarkar, "Effect of geometry of planar antenna arrays on Cramer-Rao Bounds for DOA estimation," in *2010 IEEE 10th Int. Conf. on Signal Processing (ICSP)*, Beijing, China, 2010, pp. 389–392.

[4] J. Zhu and H. Wang, "Effects of sensor position and pattern perturbations on CRLB for direction finding of multiple narrow-band sources," in *4th Annu. ASSP Workshop on Spectrum Estimation and Modeling*, Minneapolis, MN, 1988, pp. 98–102.

[5] I. Skog and P. Händel, "Calibration of a MEMS inertial measurement unit," in *XVII IMEKO World Congress*, Rio de Janeiro, Brazil, 2006, pp. 1–6.

[6] N. El-Sheimy, H. Hou, and X. Niu, "Analysis and modeling of inertial sensors using Allan variance," *IEEE Trans. Instrum. Meas.*, vol. 57, no. 1, pp. 140–149, Jan. 2008.

[7] P. Petkov and T. Slavov, "Stochastic modeling of MEMS inertial sensors," *Cybernetics and information technologies*, vol. 10, no. 2, pp. 31–40, 2010.

[8] D. W. Allan, "Statistics of atomic frequency standards," *Proc. IEEE*, vol. 54, no. 2, pp. 221–230, Feb. 1966.

[9] "IEEE standard specification format guide and test procedure for single-axis interferometric fiber optic gyros," *IEEE Std 952-1997*, Dec. 2008.

[10] M. M. Tehrani, "Ring laser gyro data analysis with cluster sampling technique," *Proc. SPIE*, vol. 412, pp. 207–220, Sept. 1983.

[11] R. E. Kalman, "A new approach to linear filtering and prediction problems," *Transactions of the ASME - Journal of Basic Engineering*, no. 82, pp. 35–45, Mar. 1960.

[12] W. Greg and G. Bishop, "An introduction to the Kalman filter," Department of Computer Science, University of North Carolina at Chapel Hill, Chapel Hill, NC, Tech. Rep. TR 95-041, 2006.

[13] X. R. Li and V. P. Jilkov, "Survey of maneuvering target tracking. Part I: Dynamic models," *IEEE Trans. Aerosp. Electron. Syst.*, vol. 39, no. 4, pp. 1333–1364, Oct. 2003.

[14] E. J. Lefferts, F. L. Markley, and M. D. Shuster, "Kalman filtering for spacecraft attitude estimation," *Journal of Guidance, Control, and Dynamics*, vol. 5, no. 5, pp. 417–429, Sept.-Oct. 1982.

[15] W.-T. Ang, P. K. Khosla, and C. N. Riviere, "Kalman filtering for real-time orientation tracking of handheld microsurgical instrument," in *Proc. of the IEEE Int. Conf. on Intelligent Robots and Systems*, vol. 3, Sendai, Japan, 2004, pp. 2574–2580.

Paper III

Source Localization Using Virtual Antenna Arrays

Abstract

Using antenna arrays for direction of arrival (DoA) estimation and source localization is a well-researched topic. In this paper, we analyze virtual antenna arrays for DoA estimation where the antenna array geometry is acquired using data from a low-cost inertial measurement unit (IMU). Performance evaluation of an unaided inertial navigation system with respect to individual IMU sensor noise parameters is provided using a state space based extended Kalman filter. Secondly, using Monte Carlo simulations, DoA estimation performance of random 3-D antenna arrays is evaluated by computing Cramér-Rao lower bound values for a single plane wave source located in the far field of the array. Results in the paper suggest that larger antenna arrays can provide significant gain in DoA estimation accuracy, but, noise in the rate gyroscope measurements proves to be a limiting factor when making virtual antenna arrays for DoA estimation and source localization using single antenna devices.

©2015 IEEE. Reprinted, with permission, from
M. A. Yaqoob, A. Mannesson, N. R. Butt, and F. Tufvesson,,
“Source localization using virtual antenna arrays,”
in *2015 Int. Conf. on Localization and GNSS (ICL-GNSS)*, Göteborg, Sweden, 2015, pp. 1-6.

1 Introduction

Direction of arrival (DoA) information at an antenna array of a mobile station is very useful for positioning purposes. DoA information can be directly used for triangulation to find the position of the mobile station in a given frame of reference. In [1], a random 3-D antenna array is used for DoA estimation, where, a virtual antenna array is formed by moving a single receive antenna in 3-D and estimating the antenna position coordinates from inertial measurement unit (IMU) measurements. Furthermore, in [2, 3], the effect of IMU sensor noise on the allowable time-duration of the virtual antenna trajectory, and consequently, on DoA estimation is provided. It has been shown that the length of the virtual antenna arrays is limited by the growing standard deviation of the antenna position errors. For an unaided inertial navigation system the standard deviation of the position estimation error grows over time if there is not any periodic correction made to the estimated position. However, the estimated position with small to moderately large position errors can be obtained for small integration times for which the uncertainty of the estimated position remains within a specified limit [2, 4].

Several authors have made contributions in the literature for DoA estimation with antenna arrays having antenna position perturbations. In [5], the authors have provided a discussion on the optimality of a delay-and-sum beamformer for antenna arrays with random antenna position perturbations. If the antenna position errors are assumed to be random at different antenna positions, their influence can be considered as if the signal to noise ratio (SNR) of the received radio signal is decreased. It has been shown that, for small to moderately large errors, conventional delay-and-sum beamforming would be optimal to estimate DoA of a single source located in the far field of the array. In [6, 7, 8], the authors have considered a scenario where more than one source is present transmitting the radio signal and the array is perturbed with small to moderately large antenna position errors. In those references, the authors have suggested that antenna array calibration and DoA estimation can be performed simultaneously with some underlying assumptions to fulfill the identifiability criterion for the joint estimation of antenna position errors and DoA of the incoming radio signal.

Our first main contribution in this paper is to investigate the effect of each individual IMU noise source on the performance of an unaided inertial navigation system. For this purpose, using the extended Kalman filter (EKF) that has been formulated in [2], we provide a detailed study of the effect of individual IMU noise sources on the unaided navigation system performance. Acceleration and rate gyroscope measurements from the IMU are used allowing six degrees of freedom inertial navigation system. In [9], the authors have analyzed mean drift in the static IMU position using Monte Carlo simulations where the IMU was considered static and stochastic errors in the IMU data are used as measurements from the IMU. Another approach in the literature is to derive complex analytical expressions to determine the effect of IMU noise sources on the navigation system performance [4]. We provide a direct and simple approach to analyze the results of position estimation error standard deviation vs. time of an unaided inertial navigation system w.r.t the different IMU sensor noise parameters using an EKF.

It is also of interest to study how the DoA estimation or source localization problem is affected by the shape of a virtual antenna array. In this regard, our second contribution is to provide a detailed Cramér-Rao lower bound (CRLB)-based study of DoA estimation from random 3-D antenna arrays assuming perfect knowledge of the antenna elements. We provide mean standard deviation of the DoA estimation error for random 3-D antenna arrays using Monte Carlo simulations. Different SNR values and different array lengths in terms of allowed time-duration for making virtual antenna arrays are considered for the simulations.

Our idea is to to make virtual antenna array where the antenna location is tracked using IMU measurements of acceleration and angular speed for short integration times; and then doing DoA estimation for positioning and source localization purposes. The paper discusses fundamental limitations of this technique and brief results about the achievable accuracy of DoA estimation using such antenna arrays are provided. The results from the first part of the study helps us to identify the allowed time-duration for making the virtual antenna array using the IMU measurements. While, the second part discusses about the mean DoA estimation performance that can be achieved using random 3-D antenna arrays if a single source is present in the far field.

The paper is organized as follows. Section 2 demonstrates how the IMU data is simulated for random trajectories in 3-D. The effect of IMU measurement noise on the unaided inertial navigation system performance is determined in Section 3. A brief description on the use of CRLB followed by Monte Carlo simulation results for DoA estimation are given in Section 4. Finally, a summary of results, and conclusion are given in Section 5.

2 IMU Data Generation

Using the Singer motion model, which can be used to model maneuvering of a moving object having time correlated acceleration, a random trajectory can be made in 3-D as described in [2, 10, 11]. With the Singer model, acceleration and rotation rate data samples are generated with a first-order Gauss-Markov process. The discrete-time equivalent for the acceleration data samples is given as [10, 11]

$$\mathbf{a}_{k+1}{=}a_d\mathbf{a}_k + b_d\nu_{\mathbf{a}_k}, \tag{1}$$

where $\mathbf{a}_k \in \mathbb{R}^3$ is the acceleration at time index k, $a_d{=}e^{-\frac{T_s}{\tau_a}}, b_d{=}\int_0^{T_s} e^{-\frac{t}{\tau_a}}dt$, $\nu_{\mathbf{a}_k}$ is white Gaussian noise at time index k, T_s is the sample time, and τ_a is the maneuver time constant. The variance of the moving object's acceleration σ^2_{acc} can be defined as [10]

$$\sigma^2_{acc} = \frac{a^2_{\max}}{3}(1 + 4P_{\max} - P_0), \tag{2}$$

where $a_{\max}$ is the maximum acceleration during object's maneuver; $P_{\max}$ and P_0 model the probability of having maximum acceleration and zero acceleration during the maneuver. $\sigma^2_{\nu_\mathbf{a}}$, the variance of the white Gaussian noise process that drives the Gauss-Markov process in (1) is computed as

$$\sigma^2_{\nu_\mathbf{a}} = \frac{1 - a^2_d}{b^2_d}\sigma^2_{acc}. \tag{3}$$

Similarly, rotation rate data samples are generated as well using the Singer model.

2.1 Random 3-D Antenna Array Coordinates

Using the Singer model, acceleration and rotation rate data is generated for each of the three coordinate axis. For a typical movement by holding an IMU in hand (e.g. a smart phone equipped with an IMU and a single antenna receiver), values of the different parameters in the Singer model are set as τ_a=2.5 s, $a_{\max}$=1 m/s^2, P_0=0.99, and $P_{\max}$=0.01. For rotation rate data, the maximum angular speed is set as w_{max}=600 deg/s while the remaining parameters are the same as are used for the acceleration data. Similar parameter settings for each of the three coordinate axis are used for the acceleration as well as for the angular speed. A sample realization of the simulated acceleration during 10 seconds is shown in Figure 1 for each of the three coordinate axes. Simple double integration of the acceleration along each of these three coordinate axes provides the position displacement in each axis as shown in Figure 2. A 3-D plot of the same position displacement data is shown in Figure 3, where the origin is defined at the center of gravity of the array.

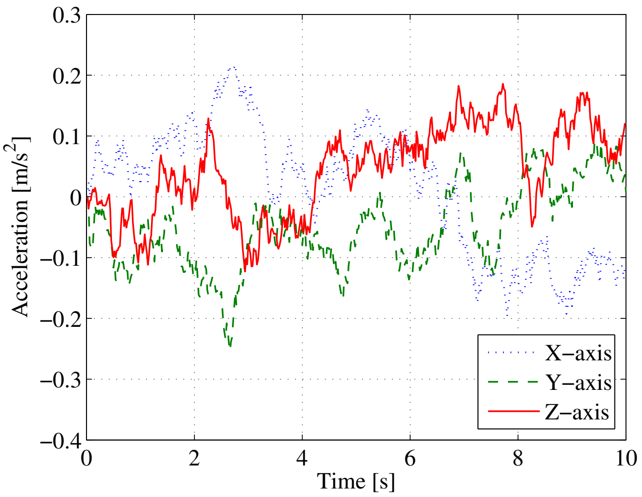

Figure 1: Example plot of acceleration data in Cartesian coordinates using the Singer model.

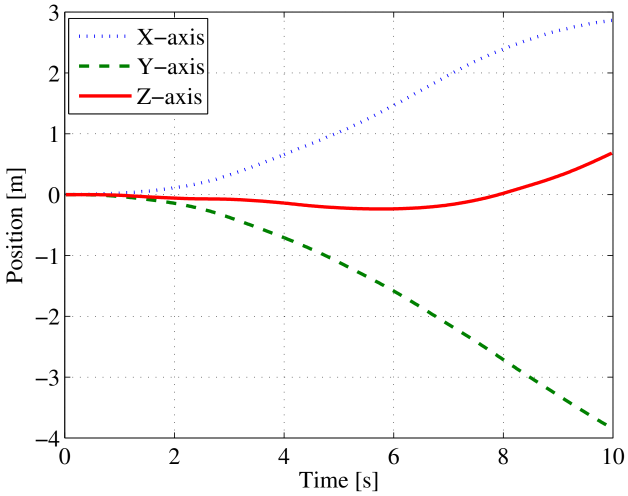

Figure 2: Position displacement calculated by double integration of the acceleration data shown in Figure 1.

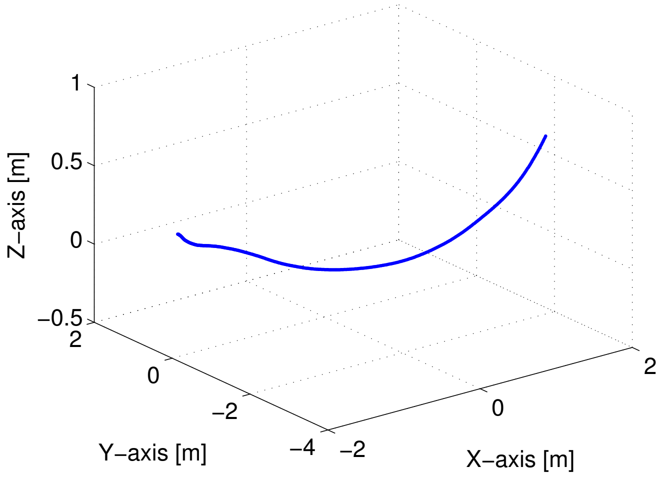

Figure 3: Trajectory from position estimates shown in Figure 2 plotted in 3-D. Origin is defined at the center of gravity of the array.

3 IMU Sensor Noise and Inertial Navigation System Simulation

For a low cost MEMS based IMU, white Gaussian noise and bias instability in the IMU measurements are the main sources of errors in the position estimates in an unaided inertial navigation system for short integration times [2]. These stochastic errors are typically quantified using Allan variance analysis [12, 13]. Using static IMU data as shown in [2], their numerical values are calculated and are given in Table 1. The IMU used in the measurements is a Phidget-1044 which is a low cost MEMS based IMU and it provides 3-axis acceleration and rotation rate measurements [14].

Table 1: Noise Parameters for Accelerometer and Gyroscope [2]

	VRW / ARW	Bias Instability
Accelerometer	5.86×10^{-4} m/s/$\sqrt{\text{s}}$	2.85×10^{-4} m/s^2(at 115 s)
Gyroscope	1.63×10^{-2} deg /$\sqrt{\text{s}}$	7.5×10^{-3} deg /s(at 115 s)

The sensor noise parameters in Table 1 are used as nominal noise parameters to simulate noise in the acceleration and rotation rate data samples in the following subsections. Using the state space model in the EKF, antenna position coordinates are estimated along-with other parameters in the state vector. After each iteration of the EKF, the estimation error covariance matrix is also obtained for the parameters in the state vector. Position estimation error standard deviation results from the EKF are then used to investigate the effects of stochastic errors in the accelerometer and rate gyroscope measurements, as given in the following sections 3.1, 3.2 and 3.3.

3.1 Accelerometer Noise

In order to investigate the effect of accelerometer noise on the position estimation error, it is assumed that the device's initial orientation is known and that there is no noise in the gyroscope measurements.

Velocity Random Walk (VRW)

By using the nominal value of the VRW noise parameter given in Table 1 and setting the bias instability noise in the accelerometer measurements to zero, the state vector is estimated from the EKF along-with the estimation error covariance matrix. Figure 4 shows the standard deviation of the position estimation error vs. time for each of the three coordinate axes. It can be noted from the plots that all of the three coordinate axes overlap each other. This suggests that if the accelerometer white Gaussian noise is the only noise source in the IMU measurements, then similar position estimation error will be observed for each of the three coordinate axes. Furthermore, by changing the VRW noise parameter to twice and half of the nominal value, the position estimation error standard deviation results from the EKF are obtained as shown in Figure 4. These results indicate that the standard deviation of the position estimation error is directly proportional to the VRW noise parameter.

Acceleration Bias Drift

By using the nominal value of the bias instability noise parameter for the accelerometer measurements given in Table 1 and setting the VRW noise parameter to zero, the state vector is estimated from the EKF along-with the estimation error covariance matrix. Figure 5 shows the standard deviation of the position estimation error vs. time for each of the three coordinate axes. The plots show that the position estimation error for the three coordinate axes is different in each axis. Due to the fact that the bias drift is a time correlated process and it is independent in each axis, different position estimation error standard deviation results are observed for each axis. Further, by varying the

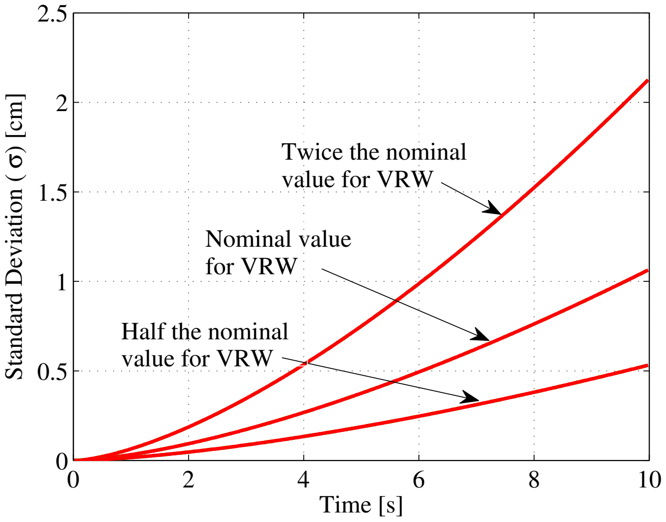

Figure 4: Plot of the standard deviation of the position estimation error for the three coordinate axes vs. time with VRW noise only. All the three coordinate axes curves overlap each other with VRW noise only in the IMU measurements. The VRW noise parameter is also changed from the nominal value given in Table 1 to study its effect on the navigation system performance.

standard deviation of the white Gaussian noise that drives the accelerometer bias drift process, results for the standard deviation of the position estimation error are also obtained from the EKF as shown in Figure 5. These results illustrate that the standard deviation of the position estimation error is directly proportional to the bias instability noise parameters.

VRW and Acceleration Bias Drift

By using the nominal values of the VRW and bias instability noise parameters for the accelerometer measurements given in Table 1, the state vector is estimated from the EKF along-with the estimation error covariance matrix. Figure 6 shows the standard deviation of the position estimation error vs. time for each of the three coordinate axes. From the plot it can be noted that the VRW is the dominant error source as compared to the acceleration bias drift in unaided inertial navigation system for short integration times of about 4-6 s.

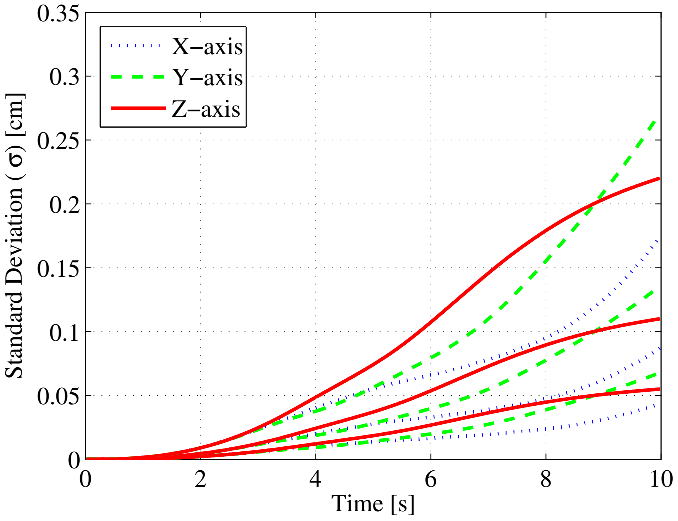

Figure 5: Plot of the standard deviation of the position estimation error for the three coordinate axes vs. time with bias instability noise only. Bias instability noise parameter is also changed from the nominal value given in Table 1 to study its effect onto the navigation system performance.

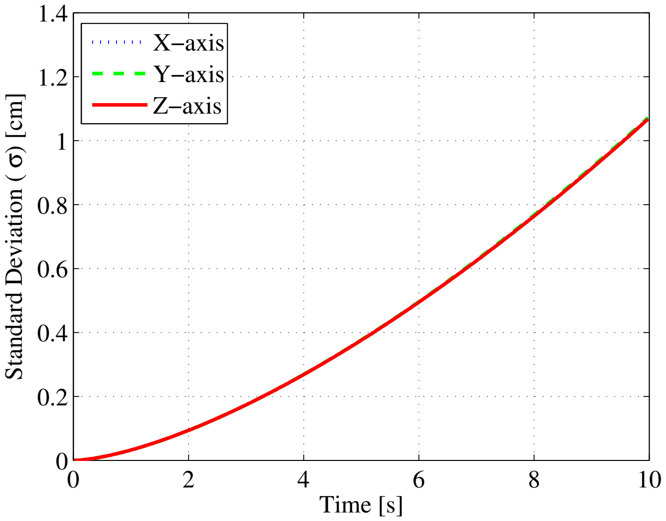

Figure 6: VRW and bias instability noise in the accelerometer measurements is considered using nominal values as given in Table 1. Plot of the standard deviation of the position estimation error for the three coordinate axes vs. time with accelerometer noise only.

3.2 Gyroscope Noise

In order to investigate the effect of gyroscope noise on the position estimation error, it is assumed that the device's initial orientation is known and that there is no noise in the accelerometer measurements.

Angle Random Walk

By using the nominal value of the ARW noise parameter given in Table 1 and setting the bias instability noise in the gyroscope measurements to zero, the state vector is estimated from the EKF along-with the estimation error covariance matrix. Figure 7 shows the standard deviation of the position estimation error vs. time for each of the three coordinate axes. From the plot, it can be observed that the estimation error standard deviations in the horizontal axes are larger as compared to the vertical axis. Any tilt error ζ in the orientation estimate of the IMU projects the gravity acceleration incorrectly onto the horizontal axes and vertical axis. The component of gravity acceleration onto the horizontal axes is projected as $g \sin(\zeta)$, while the component that is projected onto the vertical axis is $g(1 - \cos(\zeta))$. Using small angle approximation, $\sin(\zeta) \approx \zeta$ and $\cos(\zeta) \approx 1$, which means that the residual acceleration due to gravity along the horizontal axes is larger as compared to the vertical axis. This leads to larger position estimation errors along the horizontal axes as compared to the vertical axis. Similar results can be found in [9]. Furthermore, by changing the ARW noise parameter to twice and half of the nominal value, the position estimation error standard deviation results from the EKF are obtained as shown in Figure 7. These results indicate that the standard deviation of the position estimation error is directly proportional to the ARW noise parameter.

Rotation Rate Bias Drift

By using the nominal value of the bias instability noise parameter for the gyroscope measurements given in Table 1 and setting the ARW noise parameter to zero, the state vector is estimated from the EKF along-with the estimation error covariance matrix. Figure 8 shows the standard deviation of the position estimation error vs. time for each of the three coordinate axes. Due to the bias drift, tilt errors result in the orientation estimate and consequently residual accelerations due to gravity in each of the coordinate axes. Figure 8 shows that the position estimation error standard deviations in the horizontal axes are also larger as compared to the vertical axis due to the bias drift in the gyroscope measurements. The explanation is similar as given in Section 3.2. Further, by varying the standard deviation of the white Gaussian noise that

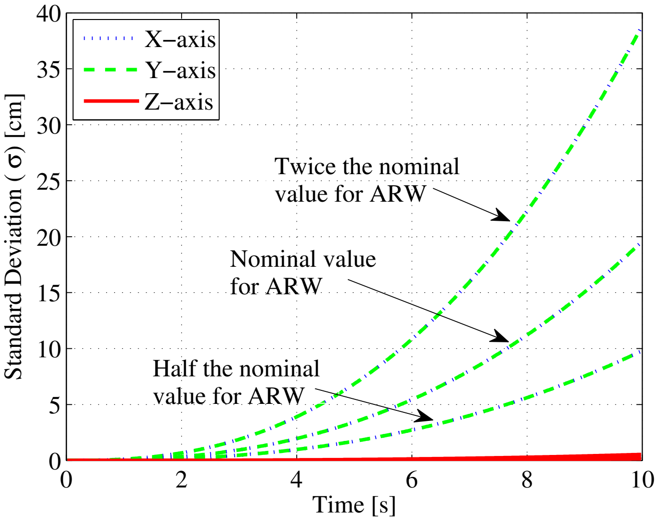

Figure 7: Plot of the standard deviation of the position estimation error for the three coordinate axes vs. time with ARW noise only. The x- and y-axis plots overlap each other while the z-axis has smaller standard deviation as compared to the horizontal axes. The ARW noise parameter is also changed from the nominal value given in Table 1 to study its effect on the navigation system performance.

drives the gyroscope bias drift process, results for the standard deviation of the position estimation error are also obtained from the EKF as shown in Figure 8. These results indicate that the standard deviation of the position estimation error is directly proportional to the bias instability noise parameters.

ARW and Rotation Rate Bias Drift

By using the nominal values of the ARW and bias instability noise parameters for the gyroscope measurements given in Table 1, the state vector is estimated from the EKF along-with the estimation error covariance matrix. Figure 9 shows the standard deviation of the position estimation error vs. time for each of the three coordinate axes. From the plot it can be noted that the ARW is the dominant error source as compared to the gyroscope bias drift in unaided inertial navigation system for short integration times of about 4-6 s.

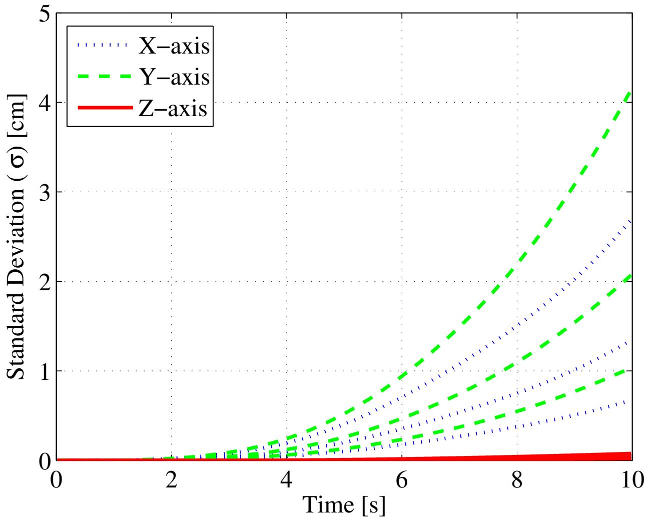

Figure 8: Plot of the standard deviation of the position estimation error for the three coordinate axes vs. time with bias instability noise. The bias instability noise parameter is also changed from the nominal value given in Table 1 to study its effect onto the navigation system performance.

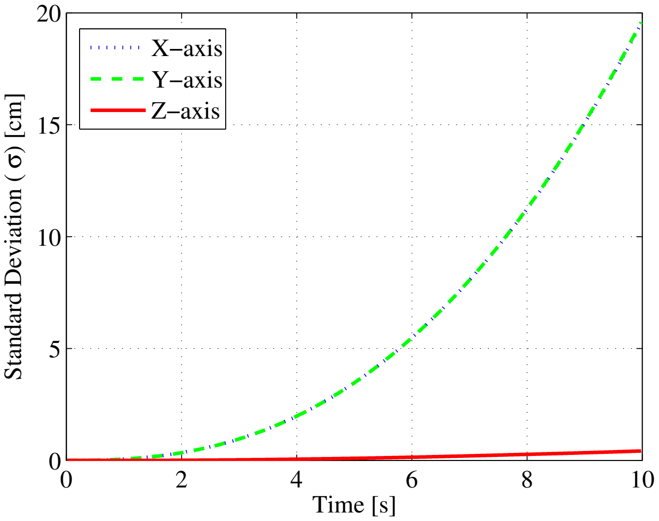

Figure 9: Plot of the standard deviation of the position estimation error for the three coordinate axes vs. time with gyroscope noise only when ARW and bias instability noise in the gyroscope measurements is considered.

3.3 Both Accelerometer and Gyroscope Noises

By using the nominal values of the accelerometer and the gyroscope noise parameters given in Table 1, the state vector is estimated from the EKF alongwith the estimation error covariance matrix. Figure 10 shows the standard deviation of the position estimation error vs. time for each of the three coordinate axes. The plot shows how the standard deviation of the position estimation error grows over time for an unaided inertial navigation system. It can be noted that the noise in the gyroscope measurements or more specifically the white Gaussian noise or ARW in the rate gyroscope measurements is the dominant error source in unaided inertial navigation systems for short integration times of about 4-6 s.

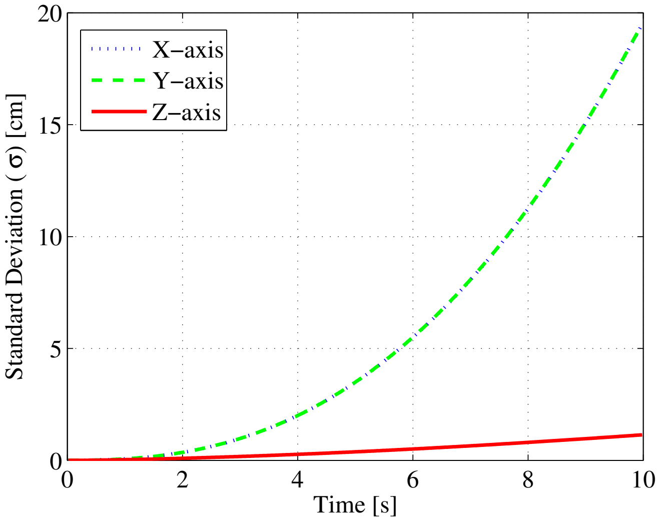

Figure 10: Plot of the standard deviation of the position estimation error for the three coordinate axes vs. time. Accelerometer and gyroscope noise in the IMU measurements is considered using nominal values given in able 1. The plot shows the effect of all the noise sources in the accelerometer and rate gyroscope measurements.

4 DoA Estimation using Monte Carlo Simulations

Using a minimum variance unbiased estimator, the direction of arrival estimate of an incoming radio signal received at an antenna array will be an optimal estimate in the maximum likelihood sense. The CRLB provides us such lower bound on the minimum variance that can be achieved with a maximum likelihood estimator. We will use the same formulation as in [2] to calculate the CRLB for a random antenna array of N isotropic antenna elements whose locations are known and are placed randomly in 3-D. In the calculations, the radio signal carrier frequency is set to 2.4 GHz.

Monte Carlo simulation results are used to analyze the performance of random antenna arrays in 3-D for DoA estimation. Firstly, this section provides a brief illustration of DoA estimation performance using random 3-D antenna arrays. Using 10 Monte Carlo simulations, random 3-D antenna array coordinates are obtained for 10 different antenna arrays. As described in Section 2.1, acceleration data is generated for 4 seconds using the Singer model and direct double integration of the acceleration data is performed to obtain the true antenna locations of the virtual array. Using the generated antenna arrays, CRLB results for DoA estimation are then computed for different source locations and the results are shown in Figure 11. In Figure 11, different colors are used for 10 different antenna arrays. Without any loss of generality, the source Elevation angle is fixed at $\theta = 30\,^{\circ}$ while the Azimuth angle ϕ is varied from $10\,^{\circ}$ - $360\,^{\circ}$ with a step of $10\,^{\circ}$. The plots in Figure 11 show lower bound on the achievable DoA estimation accuracy for a single plane wave source located in the far field of the array at different source locations, for 10 different antenna arrays. It can be noted that the effect of antenna array aperture w.r.t the source location plays a significant role in DoA estimation accuracy. It is also worth mentioning that the model used to make random array shapes puts no constraint on the volume spanned by the antenna array coordinates. Furthermore, using 500 Monte Carlo simulations, the mean standard deviation σ_{avg} of the DoA estimation error is calculated for random 3-D antenna arrays as

$$\sigma_{avg} = \frac{1}{500}\sum_{i=1}^{500}\sigma_i, \tag{4}$$

where σ_i describes the mean DoA estimation performance for the i^{th} antenna array in the Monte Carlo simulations. σ_i is found by computing the CRLB values for different source locations, where the Elevation angle is fixed at $30\,^{\circ}$ and the Azimuth angle is varied from $10\,^{\circ}$ - $360\,^{\circ}$ with a step of $10\,^{\circ}$. By averaging the CRLB values corresponding to different source locations, the mean CRLB

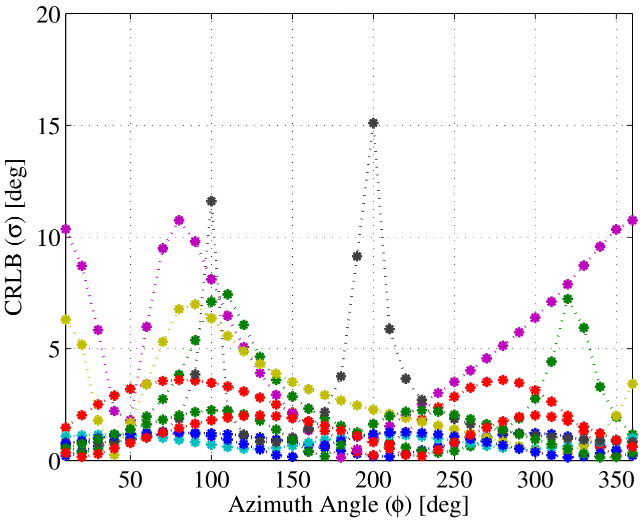

Figure 11: Plot of CRLB values w.r.t the source location angles for 10 different 3-D antenna arrays. Different colors correspond to different antenna arrays.

value σ_i is then determined. Table 2 shows the results of σ_{avg} for different array lengths in terms of time-duration for making virtual antenna arrays and for different SNR values.

Table 2: Mean standard deviation σ_{avg} of the DoA estimation error using random 3-D antenna arrays.

SNR [dB]	0		10	
Array Length [s]	4	6	4	6
σ_{avg} [deg]	8.8	3.1	2.8	1.0

The results in Table 2 illustrate the mean or the average performance of random 3-D antenna arrays for DoA estimation. One antenna array could have better DoA estimation accuracy in certain source location directions and worse DoA estimation accuracy in some other source directions. An array shape in 3-D might be devised for optimum DoA estimation for all azimuth-elevation source directions. The results in Table 2 further show that the array performance for DoA estimation improves significantly with increased array size as compared to the increase in SNR. Similarly, for other values of the Elevation angle, the mean standard deviation of the DoA estimation error results can be obtained using the Monte Carlo simulations.

5 Summary and Conclusion

In this paper, we have shown the application of a state space based extended Kalman filter to study the effect of individual IMU sensor noise parameters on the performance of an unaided inertial navigation system. We have observed that, for a typical low cost MEMS based IMU, noise in the rate gyroscope measurements is the dominant error source for the position estimation error for short integration times of about 4-6 s. Whereas, the accelerometer noise is observed to be less significant as compared to the rate gyroscope noise. We have also used Monte Carlo simulations to analyze the mean standard deviation of the DoA estimation error for random 3-D antenna arrays. Simulation results show that the array performance for DoA estimation improves significantly with increased array size as compared to the increase in signal to noise ratio. The results in the paper suggest that larger antenna arrays can provide significant gain in DoA estimation accuracy, but, noise in the rate gyroscope measurements proves to be the limiting factor when making virtual antenna arrays for DoA estimation or source localization using single antenna devices.

Acknowledgment

This work is supported by the Excellence Center at Linköping-Lund in Information Technology (www.elliit.liu.se) and by the Lund Center for Control of Complex Engineering Systems (www.lccc.lth.se) as well as the Swedish Research Council. The support is gratefully acknowledged.

References

[1] M. A. Yaqoob, F. Tufvesson, A. Mannesson, and B. Bernhardsson, “Direction of arrival estimation with arbitrary virtual antenna arrays using low cost inertial measurement units,” in *2013 IEEE Int. Conf. on Communications Workshops (ICC)*, Budapest, Hungary, 2013, pp. 79–83.

[2] M. A. Yaqoob, A. Mannesson, B. Bernhardsson, N. R. Butt, and F. Tufvesson, “On the performance of random antenna arrays for direction of arrival estimation,” in *2014 IEEE Int. Conf. on Communications Workshops (ICC)*, Sydney, Australia, 2014, pp. 193–199.

[3] A. Mannesson, B. Bernhardsson, M. A. Yaqoob, and F. Tufvesson, “Optimal virtual array length under position imperfections,” in *2014 IEEE 8th Sensor Array and Multichannel Signal Processing Workshop (SAM)*, A Coruña, Spain, 2014, pp. 5–8.

[4] D. Titterton and J. L. Weston, *Strapdown inertial navigation technology*, 2nd ed. Stevenage, United Kingdom: IET, 2004.

[5] P. M. Schultheiss and J. P. Ianniello, “Optimum range and bearing estimation with randomly perturbed arrays,” *Acoustical Society of America Journal*, vol. 68, pp. 167–173, Jul. 1980.

[6] Y. Rockah and P. M. Schultheiss, “Array shape calibration using sources in unknown locations–part I: Far-field sources,” *IEEE Trans. Acoust., Speech, Signal Process.*, vol. 35, no. 3, pp. 286–299, Mar. 1987.

[7] B. P. Flanagan and K. L. Bell, “Array self-calibration with large sensor position errors,” *Signal Processing*, vol. 81, no. 10, pp. 2201–2214, Oct. 2001.

[8] P.-J. Chung and S. Wan, “Array self-calibration using SAGE algorithm,” in *2008 IEEE 5th Sensor Array and Multichannel Signal Processing Workshop (SAM)*, Darmstadt, Germany, 2008, pp. 165–169.

[9] O. J. Woodman, “An introduction to inertial navigation,” *University of Cambridge, Computer Laboratory, Tech. Rep. UCAMCL-TR-696*, Aug. 2007.

[10] X. R. Li and V. P. Jilkov, “Survey of maneuvering target tracking. Part I: Dynamic models,” *IEEE Trans. Aerosp. Electron. Syst.*, vol. 39, no. 4, pp. 1333–1364, Oct. 2003.

[11] R. A. Singer, “Estimating optimal tracking filter performance for manned maneuvering targets,” *IEEE Trans. Aerosp. Electron. Syst.*, vol. AES-6, no. 4, pp. 473–483, Jul. 1970.

[12] D. W. Allan, “Statistics of atomic frequency standards,” *Proc. IEEE*, vol. 54, no. 2, pp. 221–230, Feb. 1966.

[13] N. El-Sheimy, H. Hou, and X. Niu, “Analysis and modeling of inertial sensors using Allan variance,” *IEEE Trans. Instrum. Meas.*, vol. 57, no. 1, pp. 140–149, Jan. 2008.

[14] “Phidgets inc. - 1044_0 - phidgetspatial precision 3/3/3 high resolution,” Retrieved March 16, 2015. [Online]. Available: http://www.phidgets.com/products.php?product_id=1044